Università degli Studi di Napoli *Federico II*

DOTTORATO EUROPEO DI RICERCA IN

FISICA

Ciclo XXXV
Coordinatore: prof. Vincenzo Canale

Study and characterization of a high-rate detection apparatus for the NUMEN project

Settore Scientifico Disciplinare FIS/04

Dottoranda
Elisa Maria Gandolfo

Tutor
Dott. Luigi Campajola
Prof. Giovanni La Rana
Dott. Paolo Finocchiaro

Anni 2019/2022

Abstract

Understanding the neutrino's nature is one of the major open quests in the physics beyond the Standard Model. Among the various approaches to this topic, the Neutrinoless Double Beta Decay (NDBD) certainly represents a unique tool for the investigation of the neutrino properties. The NUMEN project proposes a new way to access the Nuclear Matrix Element (NME) of the NDBD through the measurement of the Double Charge Exchange (DCE) cross section. The extremely low cross section, and the high intensity background foreseen, demand strict requirements for the detection apparatus which is currently under study and development. This work illustrates the main challenges of the NUMEN detection apparatus and its foreseen upgrades. In particular, this thesis presents the project and the design for the G-NUMEN array and the feasibility study of its prototype.

Introduction

Understanding the neutrino nature is one of the major open quests in the physics beyond the Standard Model.

A powerful tool for the study of this elusive particles is the Neutrinoless Double Beta Decay (NDBD), $0\nu\beta\beta$, whose experimental observation could prove the Majorana nature of the neutrino and answer to the questions about its absolute mass. The importance of the $0\nu\beta\beta$ decay has driven the attention to the development of structure model theories for the description of this process. A crucial point for this task is the determination of the Nuclear Matrix Element (NME). However, nowadays the evaluation of the NME suffers from large uncertainties due to the discrepancy between the results of the diverse structure models. A new approach to this issue is proposed by the NUMEN (NUclear Matrix Element for Neutrinoless double beta decay) project, which aims at providing information on the NME through the study of the Double Charge Exchange (DCE) reactions. The project is developed at Laboratori Nazionali del Sud (LNS) and it is based on a joint effort between theoretical and experimental research: the first focuses to the development of a DCE reaction model, the second focuses on the challenges related to the measurement of the extremely low cross section of the DCE reactions (~ nb).

The DCE reactions under study will involve heavy-ion beams, produced with the K800 Superconductive Cyclotron of LNS, impinging on targets of isotopes which are expected to decay via NDBD. Considering the rare DCE reaction probability, in order to be able to detect distinguishable DCE events the foreseen beams must have energies up to 60 AMeV with intensities of the order of 10^{12} – 10^{14} pps, corresponding to a beam power of 1- 10 kW.

These requirements demand a substantial improvement of the LNS facility (currently being upgraded), as well as the development of an *ad hoc* detection apparatus with high performance, capable of identifying and discriminating the DCE events with respect to an overwhelming background coming from the several other competing reactions.

The core of the experimental apparatus is MAGNEX, the large acceptance spectrometer of the LNS, together with its Focal Plane Detector (FPD). The DCE events will be identified by combining the information from the algebraic methods for the trajectory reconstruction inside MAGNEX and the ion detection in the FPD. The latter is composed of a Gas Tracker and a Particle Identification wall for the reconstruction and identification of the ejectile trajectories at the MAGNEX focal plane with high spatial and energy resolution. Both FPD components are currently under upgrade.

For the reactions involving high energy beams and target nuclei in the moderately and heavily deformed mass region, the MAGNEX spectrometer will not have the energy resolution required to distinguish the events under study. In all these cases, it will be essential to use a gamma array to detect the energy transitions of the nuclei of interest in the area of the target: the G-NUMEN array.

The detection apparatus which will be used in the future NUMEN experiment is a complex system of different types of detectors, whose study and development are strictly correlated one to each other and whose upgrades are still on-going.

This thesis concerns the study of the NUMEN detection system, addressed in particular to the G-NUMEN array. This gamma array will be a completely new feature of the LNS facility and the state-of-the-art of its development currently involves simulations and preliminary tests. This work presents the first experimental results of a prototype of the G-NUMEN detectors. In particular, an experiment (High Intensity Test for $LaBr_3$:Ce detector – HIT) has been designed and performed for the feasibility study of the detector under experimental conditions similar to the ones expected in NUMEN. The HIT experiment was performed at the ALTO facility of the IJC Laboratory, in the framework of my period abroad which was supported by the StarPlus scholarship. The results of this experiment set the stage for the development and upgrade of the future G-NUMEN array.

The first Chapter presents a description of the NUMEN project, the detection apparatus and its experimental challenges. Chapter 2 deals with the design of the components for the upgrade of the Gas Tracker detector of the MAGNEX FPD. The following chapter (Chapter 3) describes in detail the future G-NUMEN array and it presents the characterization of the detector's prototype. In Chapter 4 and Chapter 5 I present the HIT experiment. Chapter 4 deals with the study of the in-beam response of the detector and its performances at high rates, Chapter 5 illustrate the radiation damage study of the prototype.

1. The NUMEN project

The motivations for the work presented in this thesis are related to the challenging experimental needs of the NUMEN (Nuclear Matrix Element (NME) for Neutrinoless double beta decay (NDBD)) project at the LNS – INFN Catania. An overview of this experiment is due for the proper introduction of this thesis framework (sec. 1.1). The NUMEN project is strictly related to the POTLNS PON project for the upgrade of the LNS facility which is essential for the foreseen outcome of the NUMEN experiment itself. The main upgrade involves the LNS K800 superconductive cyclotron presented in sec. 1.2. NUMEN foresees a high performance detection apparatus (sec. 1.3), a complex system of several detectors whose development and study are strictly related one to the others: the MAGNEX spectrometer and its Focal Plane Detector and the gamma array G-NUMEN whose study is the core of this thesis work.

1.1. An overview of the project

The NUMEN project aims at the investigation of the Double Charge Exchange (DCE) reactions induced by heavy ions at energies above the Coulomb barrier, with the final purpose to extract information on the Nuclear Matrix Element of the $0\nu\beta\beta$ decay [1], [2], [3].

The latter are of a great interest because their determination provides information on the half-life $T_{1/2}$ of the NDBD decay, which represents an investigation tool for the effective Majorana mass of the neutrino:

$$[T_{1/2}^{0\nu\beta\beta}(0^+ \rightarrow 0^+)]^{-1} = G_{0\nu}|M_{0\nu}|^2|f(m_i, U_{ei}, \xi_i)|^2 \tag{1.1}$$

$$M_{0\nu} = \langle\psi_f|\hat{O}_{0\nu\beta\beta}|\psi_i\rangle \tag{1.2}$$

where $G_{0\nu}$ is the phase space factor, $f(m_i, U_{ei}, \xi_i)$ contains information about the average neutrino mass m_i, the mixing coefficients U_{ei} and the Majorana phases ξ_i and $M_{0\nu}$ is the transition probability between the final ψ_f and initial state ψ_i of the NDBD.

An accurate evaluation of the NME can therefore contribute to the evaluation of the neutrino mass, as well as the definition of the neutrino's nature and hierarchy. Nowadays, the NME for the NDBD are predicted with insufficient reliability to extract relevant information on the decay: the evaluation of the NME using different nuclear structure models (such as pnQRPA, EDF, ISB, IBM and ab-initio schemes for nuclear many-body calculation) can differ by a factor greater than two because the results are highly sensitive to the model used for the many-body nuclear wave function [4], [5].

In this framework, NUMEN proposes to extract information on the NME of the NDBD by a different approach, which is independent of the specific nuclear structure model being based on the DCE reaction theory. Despite being mediated by different mechanisms, there are theoretical analogies between the DCE and the $0\nu\beta\beta$ which support the NUMEN approach, such as the same initial and final nuclear states and the similar structure of the transition operators [6], [7], [8]. Thanks to these analogies, the measurement of the absolute cross section of the heavy ion induced DCE will provide a tool for the investigation of the many-body wave functions in the NME of the NDBD. The description of the theoretical aspect of the NUMEN project and the nuclear structure models currently being developed is beyond the scope of this work, but detailed information can be found in [9], [10], [11], [12], [13].

The DCE reaction leaves the associated projectile and target nuclei with the same mass but different charge:

$$a(z,n) \; + \; A(Z,N) \; \rightarrow \; b(z \pm 2, n \; \mp 2) \; + \; B(z \mp 2, n \pm 2)$$

The reactions of interests for the NUMEN project explore the two direction of isospin lowering $\tau^-\tau^-$ and rising $\tau^+\tau^+$ in analogy with the $\beta^-\beta^-$ and $\beta^+\beta^+$ decays. They involve NDBD candidate isotopes as targets such as ^{76}Ge, ^{76}Se, ^{82}Se, ^{106}Cd, ^{110}Pd, ^{116}Cd, ^{110}Sn, ^{124}Sn, ^{128}Te, ^{130}Te, ^{136}Xe, ^{130}Xe, ^{154}Sm, ^{160}Gd, ^{198}Pt and a $^{20}Ne^{10+}$ beam for the $\beta^-\beta^-$ channel and an $^{18}O^{8+}$ for $\beta^+\beta^+$ with energies in the range 15-60 AMeV . The projectiles are chosen to be nuclei with the highest DCE cross section among the lightest even-even stable nuclei to preserve the energy resolution in the reaction with the very thin targets (400 – 800 nm).

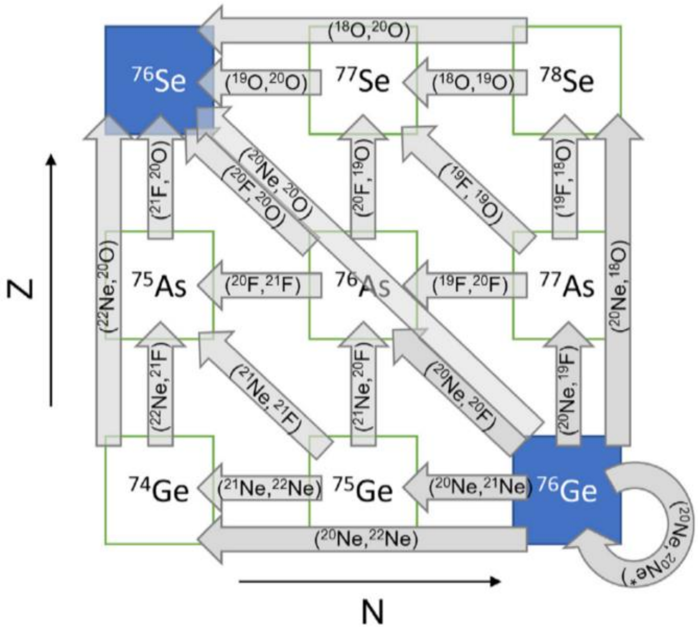

Figure 1.1 - Possible open channels for the reaction $^{76}Ge(^{20}Ne,^{20}O)^{76}Se$ [8].

Two examples of the reaction of interest respectively for $\beta^-\beta^-$ and $\beta^+\beta^+$ are:

$$^{116}Sn(^{18}O,{}^{18}Ne)^{116}Cd \tag{1.3}$$

$$^{76}Ge(^{20}Ne,{}^{20}O)^{76}Se \tag{1.4}$$

Several other reactions compete with the DCE channel such as multi-nucleon transfer, single charge exchange, elastic and inelastic channel, with cross section much higher than the DCE (Figure 1.1). Indeed, the main experimental challenge for NUMEN is related to the few nb cross section expected for the DCE reaction and the consequent need for a high-performance detection apparatus with high sensitivity and resolution and excellent discrimination capabilities.

The large-acceptance spectrometer MAGNEX (with its Focal Plane Detector FPD) [14] is the core of the NUMEN detection apparatus, allowing the identification of the ejectiles with high resolution in mass, energy and charge and therefore to distinguish the ground state–to-ground state transitions in the DCE reactions (sec. 1.3). The FPD is composed of a Gas Tracker for the reconstruction of the 3-dimensional trajectory of the heavy ions, and a E-ΔE telescope wall (PID-wall) for their identification.

The goal for the detection apparatus is to be able to select in an unambiguous way the products of the reaction of interest combining the discrimination in atomic number Z made from the PID wall, with the separation in mass number A performed with MAGNEX (Figure 1.2). The latter separates the ions according to their mass M and charge q, affecting their trajectory accordingly to the relation $B\rho = Mv/q$ (at the 1st order). When reaching the FPD, the track of the ions is reconstructed by the gas tracker while the telescope performs the separation in Z by measuring $E\,\Delta E\ \propto\ MZ^2$. The reaction products can then be identified combining the information on the horizontal position of the ions in the focal plane detector, x_{foc}, with the residual energy detected in the telescope E where the two quantities are related through $(x_{foc}/\sqrt{E}) \propto\ (\sqrt{M}/q)$.

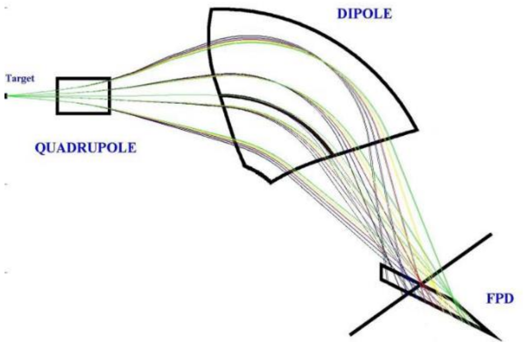

Figure 1.2 - The separation of the ion beams from the target with the MAGNEX spectrometer [6].

Figure 1.3 shows the Geant4 simulations of one telescope of the PID-wall, detecting the products of the reactions (1.4) for a beam of $^{20}Ne^{10+}$ at 35 AMeV. The events of $^{20}O^{8+}$ are detected together with contaminants of other isotopes of the oxygen, the fluorine and the neon. However, by combining the two representation in Figure 1.3 it is possible to isolate the DCE events with good efficiency.

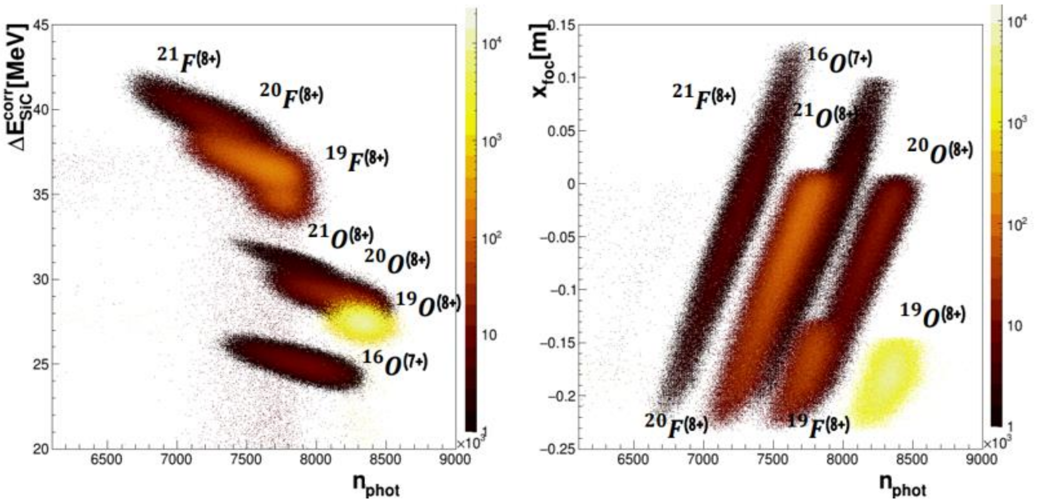

Figure 1.3 - Geant4 simulation of one telescope of the PID wall for the reaction $^{76}Ge(^{20}Ne,^{20}O)^{76}Se$ (evt not scaled for σ). On the left: separation in Z through the correlation of the energy loss in the SiC and the residual energy (expressed in number of photons). On the right: separation in A of the ions through the relation of the horizontal position in the focal plane and the residual energy [E. Gandolfo – NUMEN Collaboration Meeting 2020].

Despite the MAGNEX performance, the extremely low DCE cross section demands a substantial increase of the beam power to 1-10 kW (from the present limit of 100 W) to increase the DCE yield. This requirement involves the upgrade of the LNS facility and in particular a change in the beam extraction and transport of the K800 Superconducting Cyclotron (sec. 1.2).

In addition, in extreme experimental conditions involving nuclei in moderate and strongly deformed mass regions, the MAGNEX resolution is not sufficient to distinguish the ground state to ground state transition and it will be essential to use an ancillary gamma array (G-NUMEN) to measure the gamma decay of the first excited states. In these cases, the DCE reaction will be identified by gating the signal from G-NUMEN on the energy range of interest in the MAGNEX Focal Plane Detector. The NUMEN detection apparatus and its requirements is described in section 1.3.

1.2. The LNS cyclotron

The LNS K800 superconductive cyclotron (CS) is a three-sector accelerator whose mid-plane magnetic field (2.2 – 4.8 T) is generated by two pairs of superconducting coils. The CS is capable of producing beam of mass up to the uranium, at energies in the range 10-80 AMeV and with a beam power up to 150 W [15], [16], [17]. The maximum beam power is related to the electrostatic deflectors of the beam extraction system which limits the extraction efficiency to 50-60%. In addition, due to the absence of thermal shielding in the extraction channel, it would not be possible to dissipate the halos of beams with power greater than 150 W.

The NUMEN experiment requires beam of $^{20}Ne^{10+}$ and $^{18}O^{8+}$ with energies of 15-70 AMeV and intensity up to 10^{14} pps corresponding to a beam power of 1-10 kW. In order to match these beam requirements, it is foreseen a cyclotron upgrade for the development of a new extraction channel in which the beam will be extracted through stripping. With this technique, the ion beam will be accelerated with a charge $q = Z - 5 \div Z - 1$ and then fully stripped with an efficiency higher than

99% after crossing a stripper foil placed at the maximum radius of the CS. The beam loss expected using this technique are below 100 W even for the maximum beam power of 10 kW. Figure 1.4 shows a picture of the CS and its layout with the present and the new extraction line; the red and blue lines represents the trajectory for two of the ions of interest after being extracted. The upgrade of the cyclotron is designed alongside with the upgrade of the beamlines and the beam-dump [3].

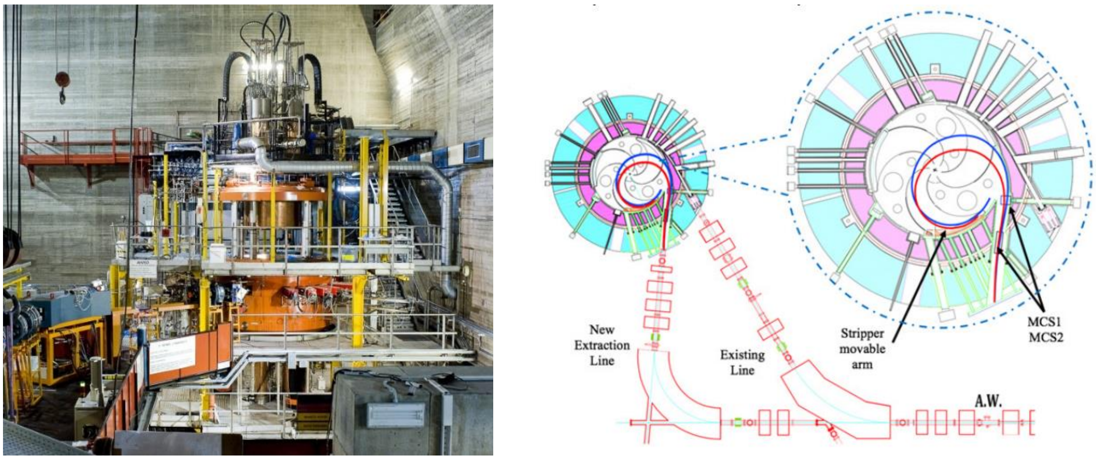

Figure 1.4 – On the left: Picture of the superconductive cyclotron at the LNS – Catania. On the right: Representation of the CS with the existing line and the new extraction line [15].

1.3. The detection apparatus

The detection apparatus, currently under development, must face several challenges related to the very low cross section of the DCE reaction and the high intensity beams [18]. These conditions demand high energy, angular and spatial resolutions, high efficiency, excellent identification and discrimination capabilities to be able to distinguish the few DCE events with respect to the overwhelming background coming from the other reaction channels. In addition, the high beam intensity also raises questions on the resistance of the apparatus under such intense radiation environments. The MAGNEX spectrometer (sec. 1.3.1) is crucial for the separation of the reaction ejectiles and their identification through the Focal Plane Detector. The latter is composed by a gas tracker and a Particle Identification wall, both being currently developed accordingly to the NUMEN needs (sec. 1.3.2). For extreme conditions of the target nuclei, the system MAGNEX+FPD will not be sufficient to discriminate between the energy transitions associated with the DCE. These cases will be resolved by using an ancillary gamma spectrometer, G-NUMEN, whose signal will be analyzed in coincidence with the FPD (sec. 1.3.3). Figure 1.5 shows a 3D model of the future detection apparatus and a picture of the present MAGNEX experimental hall. The following section presents an overview of the design and the challenges for the NUMEN experimental apparatus.

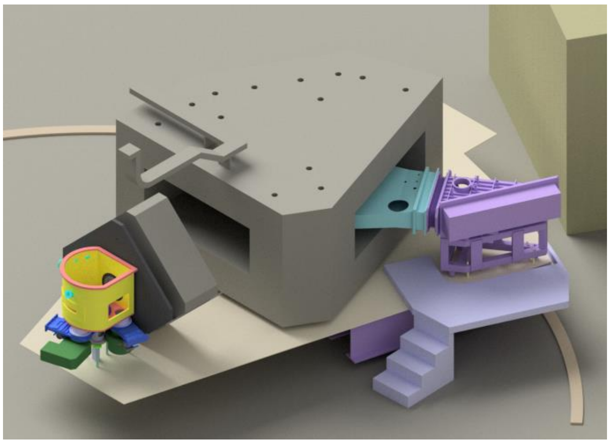
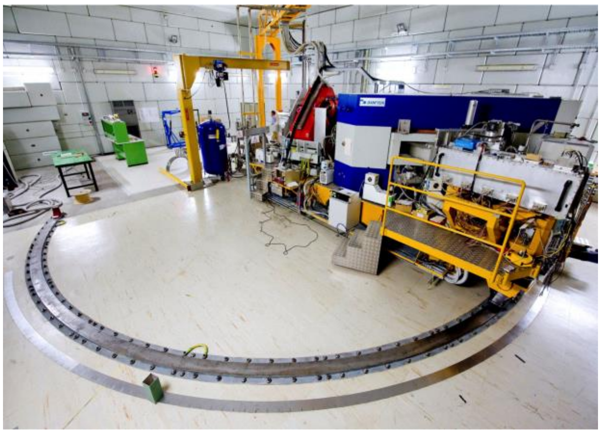

Figure 1.5 – On the left: The scattering chamber (yellow) around which G-NUMEN will be placed, the quadrupole and dipole of MAGNEX (in grey), the gas tracker (purple) and the PID-wall (green) of the Focal Plane Detector. On the right: picture of MAGNEX in the present experimental hall.

1.3.1. MAGNEX

MAGNEX is a large acceptance spectrometer ($0.2\,Tm < B\rho < 1.8\,Tm$) composed by a quadrupole (vertical focusing) and a dipole (horizontal bending), followed by a Focal Plane Detector FPD for the beam identification (Figure 1.6).

Its characteristics allow energy resolution of ${}^{\Delta E}/_{E} \sim 1/1000$ with an energy acceptance of 0.2 AMeV – 40 AMeV, a mass and angle resolution of ${}^{\Delta A}/_{A} \sim 1/160$ and $\Delta\theta \sim 0.2°$ in a momentum range $-14\% < {}^{\Delta p}/_{p} < +10\%$. The equation of motion in the MAGNEX spectrometer is calculated using the differential algebraic methods of COSY INFINITY which allows the reconstruction of the trajectory to the 10th order [14]. The main upgrade of the MAGNEX spectrometer involves the magnetic field which will be increased of ~20% to reach higher magnetic rigidity required by the

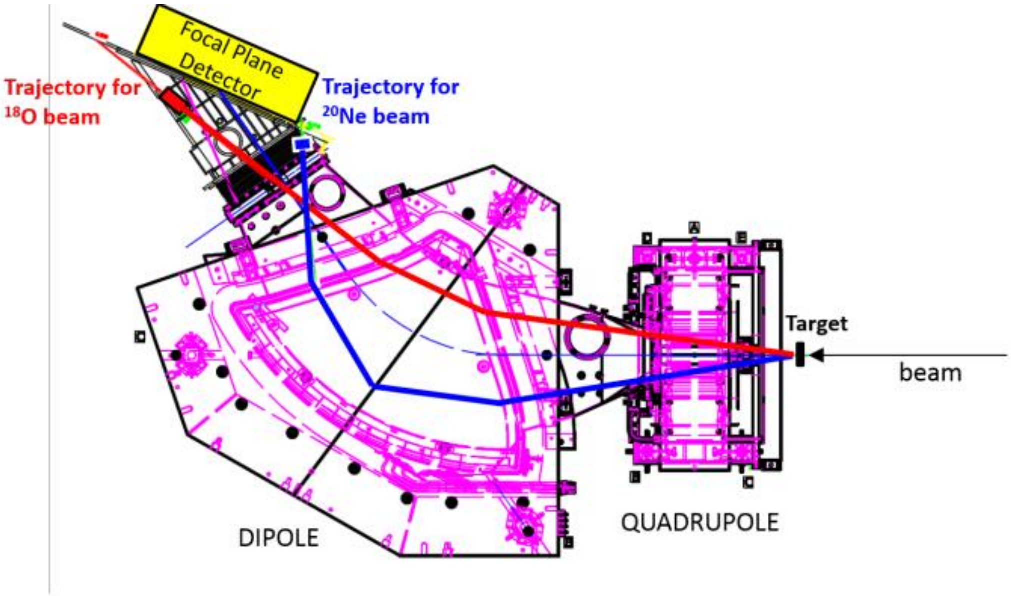

Figure 1.6 - On the left: Design of the MAGNEX components and representation of the trajectory of the primary beam of interest for NUMEN [6]

NUMEN experiment. The enhancement of the magnetic fields requires also an upgrade of the cooling system of the magnet coils at pressure up to 8 bar.

1.3.2. The Focal Plane Detector

The Focal Plane Detector (FPD) is placed with the entrance face rotated of 59.2° with respect to the MAGNEX central trajectory (Figure 1.6) and it consists of a gas tracker for the reconstruction of the ions trajectory and a Particle Identification wall (PID-wall). Both components of the FPD are currently being upgraded to match the

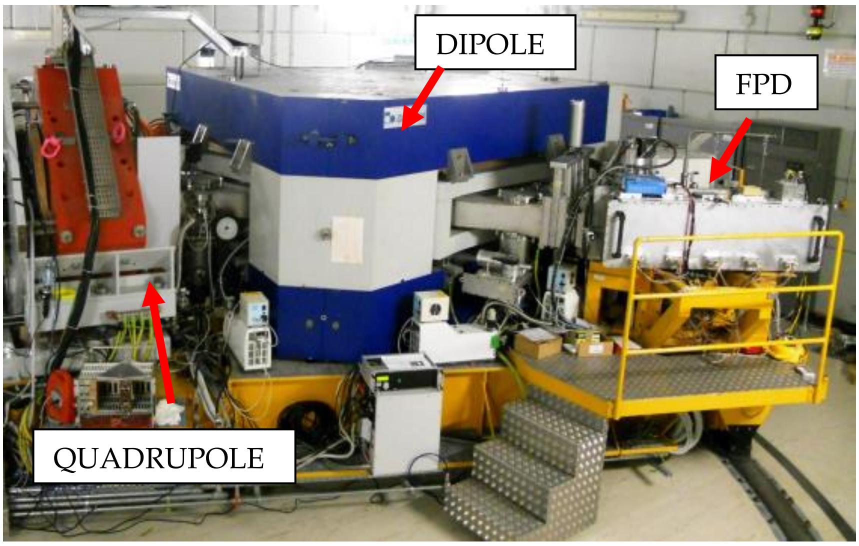

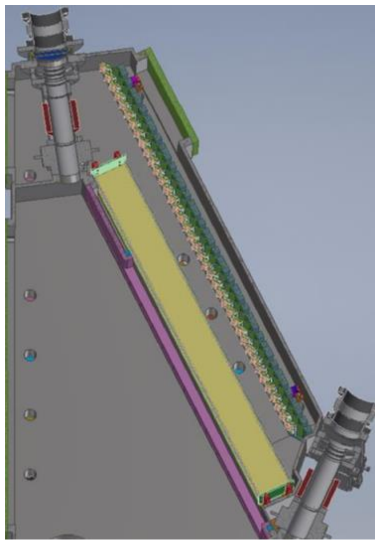

Figure 1.7 – On the left: the elements of MAGNEX. On the right: Design of the gas tracker (yellow) and the PID-wall (green) and their positioning in correspondence of the MAGNEX focal plane.

experimental needs. Figure 1.7 shows the drawings of the gas tracker and the PID wall and how they will be positioned at the focal plane of the spectrometer.

The gas tracker

The new gas tracker, under development, consists of a micro-patterned gas detector with an active volume of 1122x185x108 mm^3 filled with a pure isobutane gas (C_4H_{10}) at pressure in the range 10-100 mbar. It will be made of four modules covering a total length of 1.2 m.

The new tracker must satisfy several experimental needs:

- it must guarantee a high resolution of the phase space parameter (X_{foc}, Y_{foc}, θ_{foc}, φ_{foc}) for the identification of the trajectory of the particles in the focal plane of MAGNEX. The requirements are: horizontal position resolution 0.7mm (FWHM), horizontal angle resolution 0.5◦ (FWHM), vertical position resolution 0.7 mm(FWHM), vertical angle resolution 0.7◦ (FWHM);
- it must be very fast since the expected rate with the upgraded CS will be ~ 50 KHz/cm.

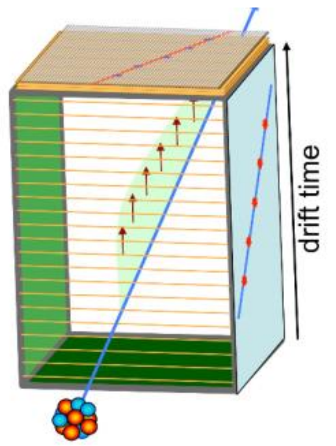

Figure 1.8 –Sketch of the gas tracker and the track left from an ion when crossing the active volume [18].

The identification of the ion trajectory will be achieved by measuring the position and the time of the charge released by the ions in the active volume of the tracker. In particular, each module of the gas tracker is divided in a vertical drift region (active volume), an electron multiplication stage based on thick-GEM (Gas-Electron-Multiplier) and a pixel read-out anode. When an ion enters the active region of the tracker (after passing through a ~µm mylar window), it ionizes the atoms along its track and the primary electrons produced are accelerated by the uniform electric field towards the upper region of the tracker where they cross the thick-GEM. In this stage the electrons are accelerated and multiplied through the holes of the thick-GEM and the produced avalanches finally reach the pixel anode where the horizontal position is measured (Figure 1.8). By adding the drift time information, it is also possible to reconstruct the vertical trajectory. An important part of the gas tracker is the design of the anode which, for each module, is divided in 5 horizontal strips. Each strip is divided in 60 pixels of 5 mm which allows an excellent spatial resolution. The design of the anode and the first tests of the detector prototype are presented in the Chapter 2.

<u>The PID-wall</u>

The PID-wall is dedicated to the identification of the reaction ejectiles, whose tracks is reconstructed by the gas tracker, through the measurement of the ion energy loss and its residual energy. The PID-wall must be capable of distinguish the ejectile isotopes for Z ~ 10 and A ~ 20 corresponding to O, F and Ne, with an energy resolution better than 2%. An important aspect is the Time Of Flight (TOF) of the ejectiles from the target to the focal plane, which must be measured with a resolution better than 2-3 ns in order to perform the coincidence between the FPD and the G-NUMEN with the lowest number of uncorrelated events. Other requirements are the granularity of the wall, to minimize the double-hit event probability, the scalability and the high geometrical efficiency given the low DCE cross section and the expected high background. Another important issue is the radiation hardness of the components as the expected heavy ions fluence is ~10^{11} ions/($cm^2 \cdot yr$).

The PID-wall for the future FPD is currently under development and it will consist of ~800 E-ΔE telescopes covering 1 m length and arranged in modules of 10 telescopes each as shown in Figures 1.9, 1.10. The modules are tilted of 35° with respect to the vertical axis of the MAGNEX focal plane. Each telescope is a SiC-CsI detector of 1.5x1.5 cm^2 area. The SiC substrate (100 μm thick) is the ΔE layer, preceding the CsI(Tl) (1 cm thick) E layer thick enough to stop all the ions in the range 15-60 AMeV. The scintillation light of the CsI is collected by an Hamamatsu S3590 photodiode with an active area of 1x1 cm^2. This telescope configuration allow good Z identification and energy resolution as proven by the simulation and experimental tests of the PID prototype [6], [18].

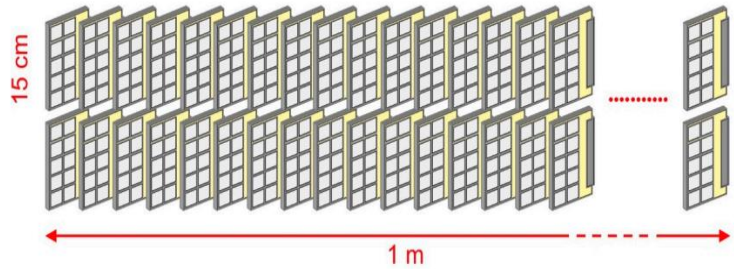

Figure 1.9 – Representation of the PID-wall modules covering the focal plane detector of MAGNEX

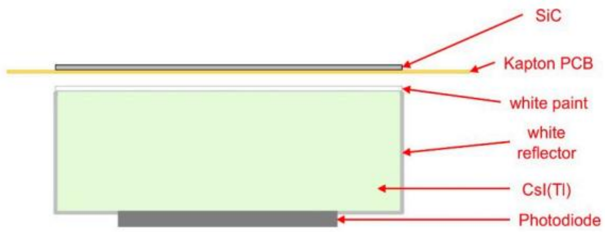

Figure 1.10 - Scheme of the PID telescope layers.

1.3.3. G-NUMEN

For all the reactions involving target nuclei in the moderately and strongly deformed mass regions, and high energies projectile, the MAGNEX resolution is not enough to separate between nearby energy states of the reaction products. Such cases involve heavy target as ^{110}Pd, ^{150}Nd, and ^{160}Gd and beam energies ≥30 AMeV. In these conditions, it is essential to use a gamma array to be coupled with the FPD to provide the required selectivity. The DCE events will be discriminated by imposing a strict time coincidence between the gamma ray and the specific ejectile in the energy region selected in the FPD.

The gamma spectrometer G-NUMEN, currently under development, will be placed around the scattering chamber before the MAGNEX quadrupole (Figure 1.5). In that zone, in the experimental conditions in which the spectrometer will be used, the gamma emission rate from a typical NUMEN experiment can reach 10^9 evt/s generating a huge background in the detectors. Other than gamma radiation, the detector will be exposed to neutron fluxes of the same intensity, which can trigger signals in the detectors and can also cause a degradation of their performance. The requirements for the G-NUMEN array are:

1. Energy resolution <10% around ~ 200 keV(in the range 3-30% depending on the energy). The reaction with the most populated energy spectra is the one involving ^{160}Gd whose first and second excited states above the g.s. have energies of 75.3 keV and 248.5 keV respectively;
2. Fast signals (<100 ns) and time resolution ~ ns;
3. High photopeak efficiency;
4. Large solid angle total coverage but high granularity to minimize the pile-up events possibility;
5. High radiation resistance to both gamma and neutrons.

The scintillators which best satisfy all these requirements are the $LaBr_3$:Ce, well known for their fast scintillation properties and good energy resolution, whose typical signals have a decay constant of < 20 ns. The future G-NUMEN array will be composed by 105 $LaBr_3$:Ce (38 mm diameter x 50 mm length) placed at 24 cm from the target and supported by mechanical shells covering seven octants of the total sphere (Figure 1.11). The solid angle coverage is 20%, which represents the best configuration given the mechanical constraint from the scattering chamber and the support systems. The expected photopeak efficiency is around

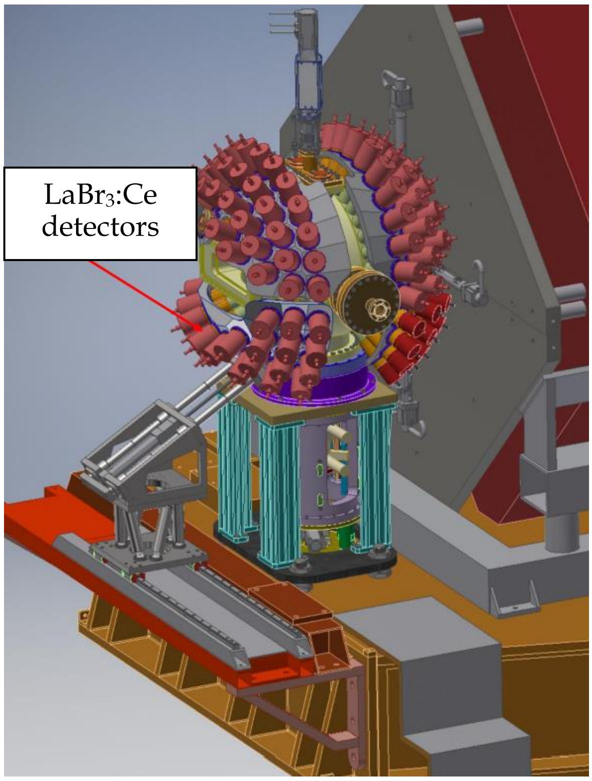

Figure 1.11 - Drawing of the G-NUMEN array and its mechanical support. The array will be placed just before the MAGNEX quadrupole, around the scattering chamber at 24 cm from the

20% at low energies and 4% at 1.3 MeV. The highest foreseen detection rate on each scintillator is ~300 kHz.

The background for the gamma array for the reactions of interest for NUMEN, as well as the detection rate, have been evaluated through a series of GEANT4 simulations to assess the expected performances of G-NUMEN [19], [20], [6], [3]. The simulations show that it is possible to achieve an observational limit of the cross section of ~ 1 nb and an uncertainty of 10-12% after 30 days of acquisition.

While the FPD projects presented in the previous sections represent an upgrade of the already existing facilities, the gamma array (G-NUMEN) represents a new detector whose study is so far being supported by mainly simulations and limited experimental tests. The work illustrated in this thesis presents one of the first experimental result of the detector prototype of the G-NUMEN array, and it is intended to test the requirements for the NUMEN project described previously.

2. The Gas Tracker of FPD

The Gas Tracker will be used for the 3-dimensional reconstruction of the tracks of the ions produced in the NUMEN reactions and separated by the MAGNEX spectrometer. As the tracker will have to reconstruct the trajectory of an elevate number of very intense ion beams, the design and the specifics for each component must satisfy strict requirements in terms of spatial, angular and time resolution (Chapter 1).

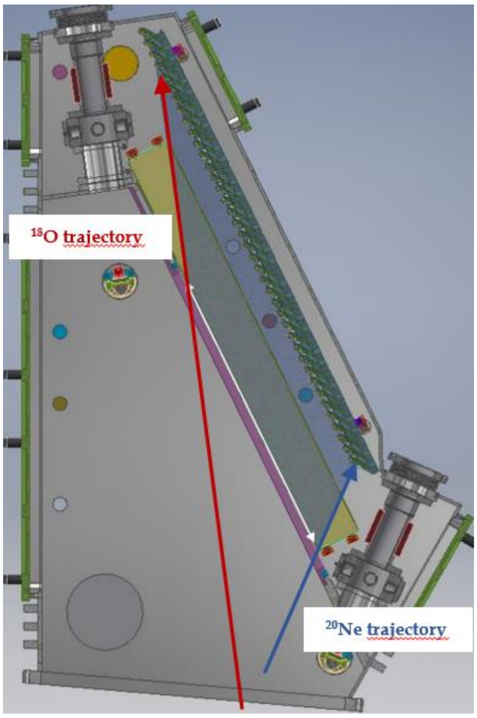

Figure 2.1 - CAD drawings of the detector of the MAGNEX focal plane. The red line represents the outer beam trajectory (^{18}O) while the blue line represents the inner trajectory correspondent to ^{20}Ne beam.

The dimensions of the future tracker will match the extension of the MAGNEX focal plane (~ 1.2 m) with an active volume of 1122x185x108 mm^3 and it will be composed by four identical modules of 300 mm each. This Chapter will provide a description of the gas tracker module (sec. 2.1) and it will illustrate the design of its components at INFN-Napoli (sec. 2.2).

2.1. The Gas Tracker module

The single module of the gas tracker is a 300x170x122.4 mm^3 proportional drift chamber filled with isobutane gas with the multiplication stage based on thick-GEM (Figure 2.2). When the ions cross the drift region, delimited by the cathode and the triple thick-GEM, the electrons produced by the ionization are driven towards the anode thanks to the application of an electric field between the cathode and the anode. The uniformity of this field is assured by a series of wires connected through a partition grid (sec. 2.2). Before reaching the anode, the electrons cross the multiplication stage composed by triple thick-GEM with high gain and capable to bear intrinsic rates higher than 10^6 Hz/mm^2. The avalanche produced in the thick-

GEM then reaches the anode through the induction region. Figure 2.3 shows the Garfield++ simulation of the electrons tracks before and after the avalanche in the region of the thick-GEM.

The electron charge is collected by the anode for the measurement of the angle and of the horizontal position. The anode is composed by 5 horizontal rows (parallel to

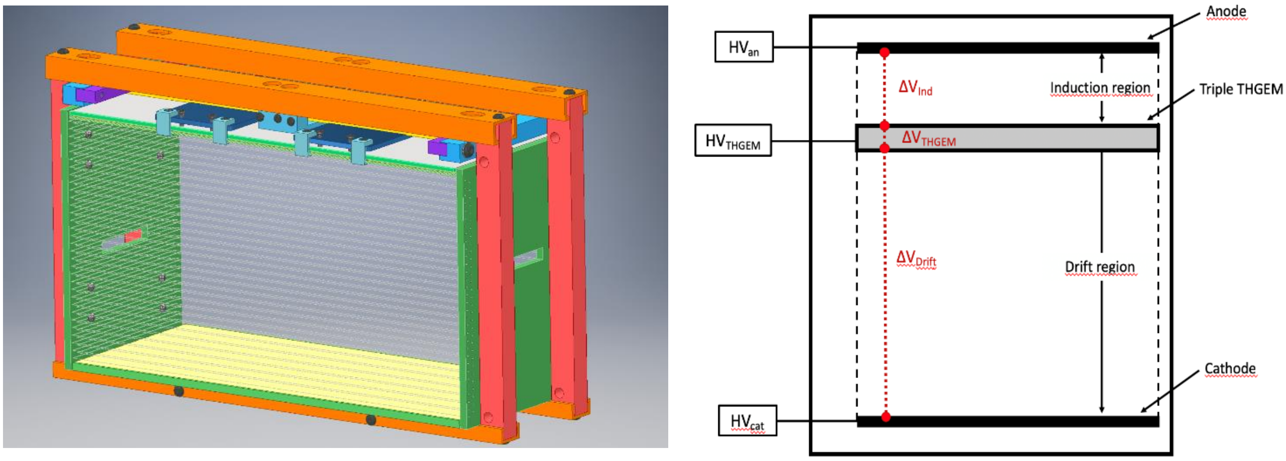

Figure 2.2 - On the left: design of the gas tracker module. On the right: Schematic representation of the components of the gas tracker.

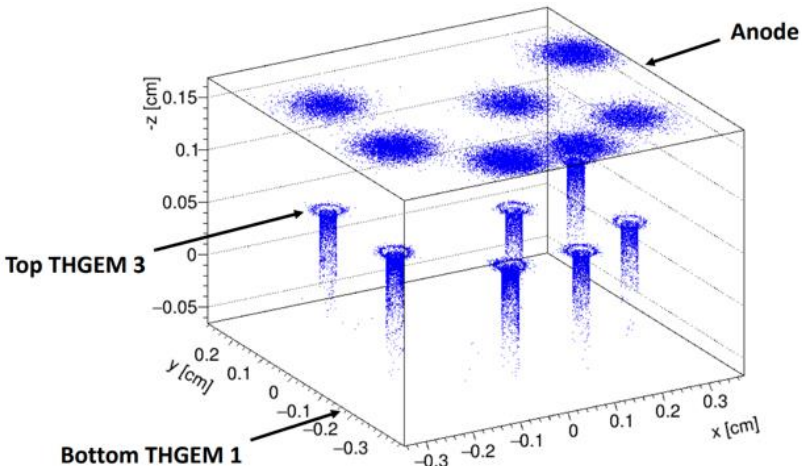

Figure 2.3 - Garfield ++ simulation of the behavior of the electrons in the region of the thick-GEM [I.Ciraldo - NUMEN Collaboration Meeting 2022]

the focal plane) each divided in several pixels (see sec. 2.2.2). The reconstruction of the horizontal track is done by taking the weighted centroid for each row and fitting the five positions obtained. The information on the vertical position of the ions is extracted from the measurement of drift times corresponding to the centroids of the five rows. This information allows the three-dimensional trajectories of the ions to be fully reconstructed. A new method for the track reconstruction based on artificial retina algorithms is currently being developed. Figure 2.4 shows a picture of the new gas tracker module.

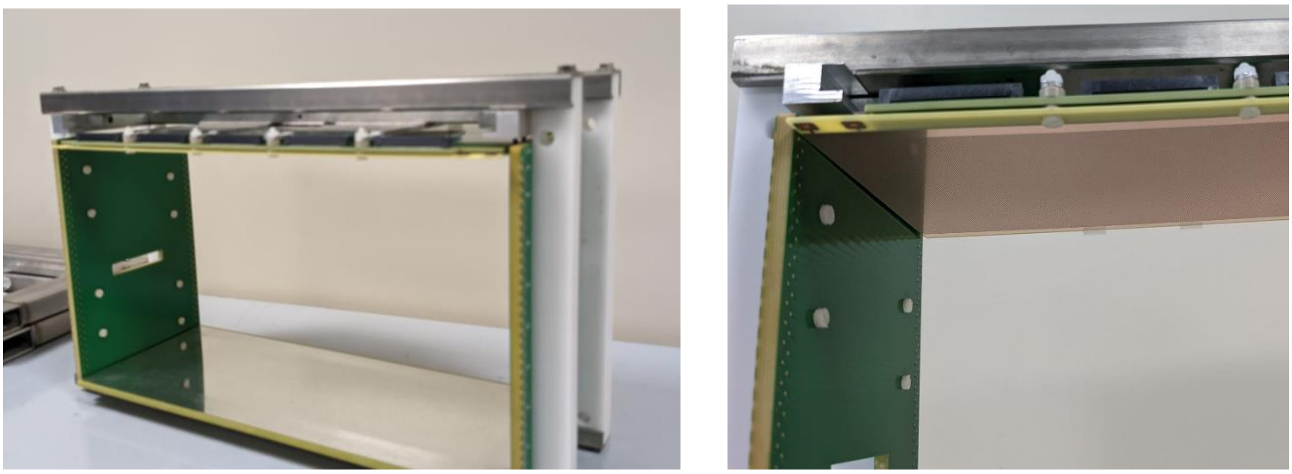

Figure 2.4 - Picture of the gas-tracker module (left) and a detail of the upper region (right) with the thick-GEM.

2.2. The components of the module

In the frame of the gas tracker project, I have developed some of the components for the module presented in the previous section: the cathode, the voltage divider and the anode (sec. 2.2.1). The cathode is a conductive layer with a sensitive area of 302x122 mm^2 biased at a voltage of -2000 V. The electric field between the cathode and the anode is kept uniform thanks to a field cage composed by two series of 64 conductive wires connected between the printed circuits on the lateral walls of the gas tracker module. The wires, spaced by 2.5 mm, are connected to each other through resistors of R = 10 MOhm in the lateral walls. The latter then act as voltage divider, and the entire configuration provides a gradient of ~47 V between each equipotential plane (Figure 2.5). The design of the field cage was based on the model obtained through electrostatic simulations using the Poisson Superfish code [6].

2.2.1. The anode

The anode is a printed circuit board with an active area of 300x118 mm^2 ,divided in horizontal strips parallel to the entrance window of the gas tracker (i.e. to the

MAGNEX focal plane). The design of the anode is shown in Figure 2.5. Each strip is divided in 60 pixels of 4.9x10 mm^2 distant to each other by 50 µm. The 5 strips allow for a reconstruction of the horizontal trajectory with a 5-point fit. However, when the electron avalanche reaches the anode, the charge collection for each strip can involve more than one pixel due to the spatial spread of the avalanche and to the halo effects. Therefore, the position of the charge for each strip is evaluated through a weighted fit of the hit pixels. This anode represents an upgrade of the old gas tracker prototype, made of only one horizontal strip, divided into vertical pads. Respect to the previous version, the design of this anode allows for a easier reconstruction of the track and it reduces the ambiguity between different track especially at high rate as the one expected in the focal plane [3], [18].

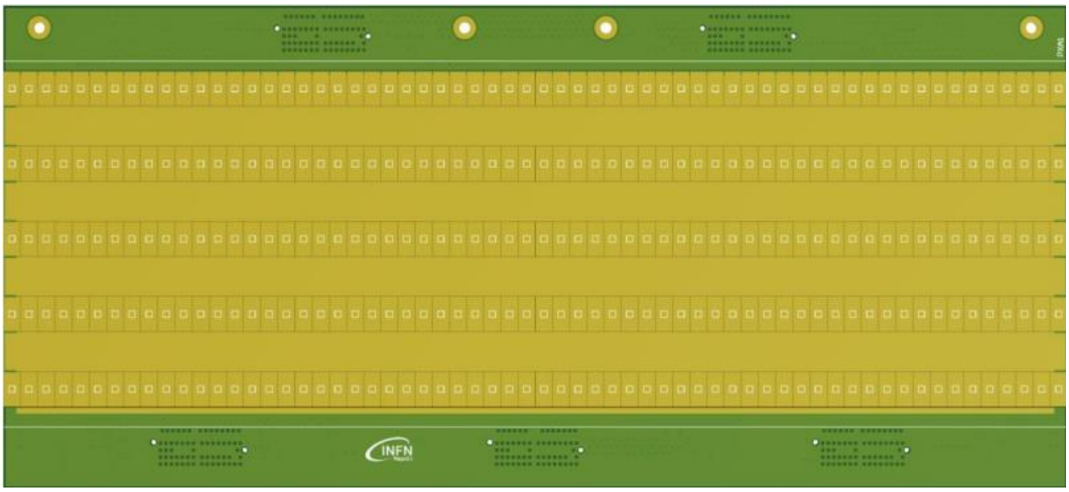

Figure 2.5 - Design of the anode for the gas tracker module. The sensitive area (yellow) is divided in 5 strips, each of them divided into 60 pixels.

Figure 2.6 shows the results of the first test with the gas tracker module using an alpha source ^{241}Am of 11 MBq. The graph on the top shows the charge collected by the anode in each strip (or row). The red line represents the reconstruction of the horizontal trajectory of the ion fitted using the 5 black dots which represents the weighted centroid of the position in the strip. The graph on the bottom shows the time distribution of the ions in each strip.

The results of these tests are preliminary, and the precise evaluation of the spatial and time resolution is currently being performed. However, a rough evaluation of the results suggests that the obtained spatial resolution is < 1 mm, matching the NUMEN requirements and the time resolution is < 10 ns.

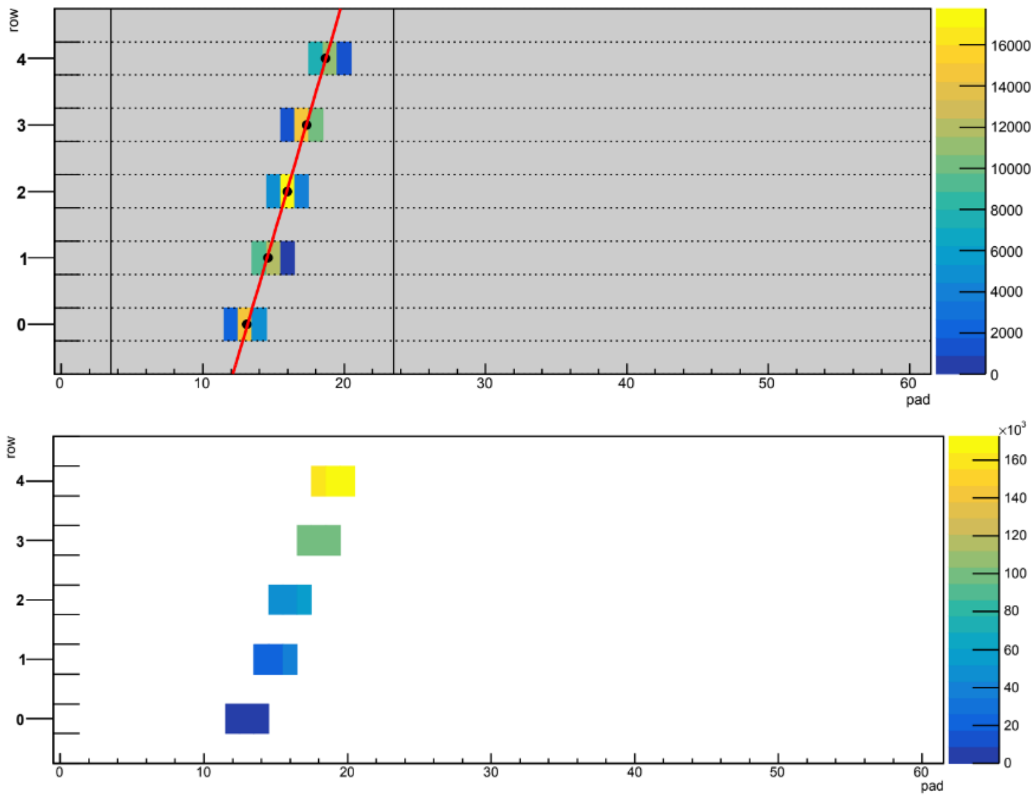

Figure 2.6 - Preliminary experimental results of the gas tracker module with the pixel anode. On the top: the horizontal position and angle of the track is obtained with a weighted fit of the signals in the 5 strips. On the bottom: the drift time of the ions for the extraction of the vertical position [D. Torresi – NUMEN Collaboration Meeting 2022].

3. The G-NUMEN array

The G-NUMEN array will be crucial for the identification of energy transition related to the DCE reaction channel when high rate of signals is expected in the overall detection apparatus.
This chapter concerns the project of the future G-NUMEN array and the design choices based on the theoretical calculation and simulations presented in chapter 1. Sections 3.2 – 3.5 present the firsts experimental results of the prototype developed for the G-NUMEN array. This study was important for the understanding of the detector properties, their advantages and their limits in the frame of the NUMEN project.
In particular, section 3.2 will illustrate the design of the prototype, its components and its acquisition system. The detector characteristics such as the intrinsic background, the calibration, the energy resolution and the efficiency are discussed in the section 3.3. The following section (3.4) deals with the study of the time resolution and the coincidence efficiency. In the same section the dependence of the detector characteristics on the acquisition rate and how this can affect its performance will be discussed. The last section deals with the study of the detector which will be used for the G-NUMEN array and the comparison of its performance with the detector prototype.
The work illustrated in this chapter was performed at the University of Napoli Federico II and at the Laboratori Nazionali del Sud LNS (Catania).

3.1. The design of the G-NUMEN project

G-NUMEN is a gamma array for the NUMEN project to be placed around the target area for the detection of the gamma transition decays from the excited states of the DCE reaction. These signals will be detected in coincidence with the projectile-like fragment (PLF) from the Focal Plane Detector of MAGNEX and related to the timing information from the cyclotron RF signal.

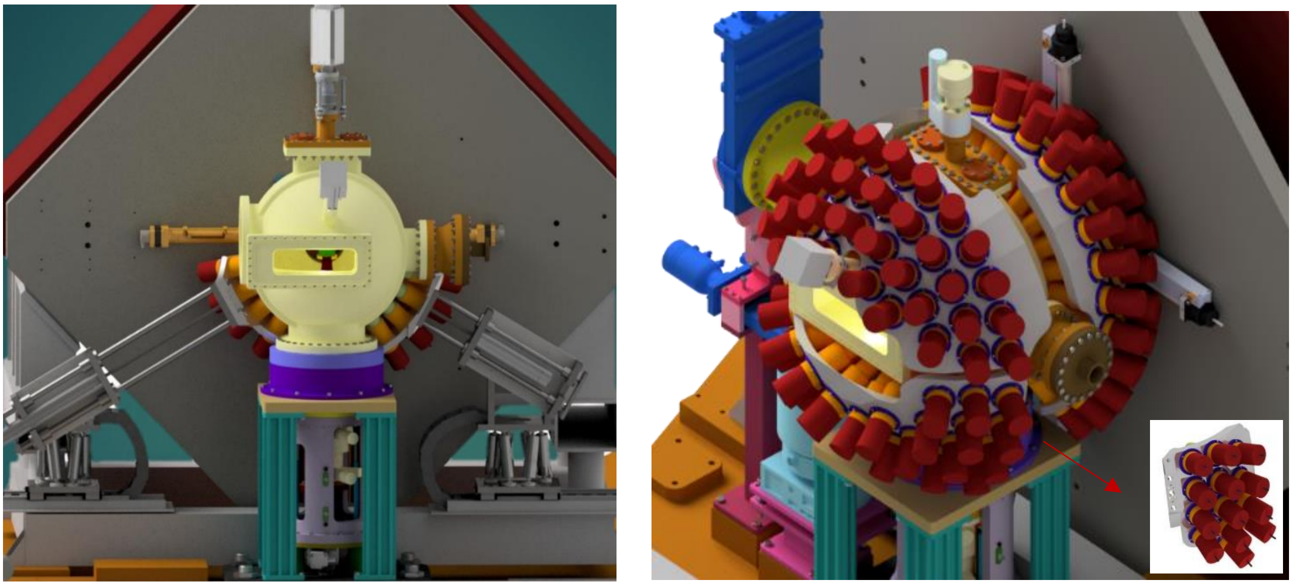

Figure 3.1 Design of the gamma array for G-NUMEN. On the left: the scattering chamber (in yellow) give a constraint for the minimum distance possible (24 cm) and the maximum solid angle coverage. On the right: the LaBr3:Ce detector are placed around the scattering chamber, supported by separated mechanical shells. The mechanical design is being developed by the NUMEN group of INFN-Torino [D. Sartirana – NUMEN Collaboration Meeting 2022].

The LaBr3:Ce scintillator crystal represents the optimal choice for the G-NUMEN array mainly due to its excellent timing properties and energy resolution (see 3.2.1). The crystals will be of 38 mm diameter and 50 mm length, which guarantees the best compromise between large dimensions for full energy absorption in the crystal volume and high granularity to reduce pile-up events and Doppler broadening of the gamma transitions from PLF [6]. Due to the very low theoretical cross section expected for DCE reaction (~nb), the geometry of the detectors must provide the largest efficiency possible. However, only a limited part of the total solid angle is available due to several mechanical constraints which limits the maximum possible coverage to 20% of the total solid angle.

The 105 LaBr3:Ce will be placed at 24 cm around the target, divided in six shells, with the axis directed towards the target at polar angles between 45 and 65 degrees respect to the beam axis (Figure 3.1). In this configuration the simulated photopeak efficiency at 1.3 MeV is ε = 4%. The detector, provided by EPIC company, will be composed of the crystal coupled with a PhotoMultiplier Tube (PMT). The signals from the detectors will be processed directly with the digitizer of the same model to the one to be used for the FPD of MAGNEX (Caen VX2745).

3.2. The prototype

The prototype of the G-NUMEN detector is a custom hand-made scintillation detector assembled with the purpose of testing the performances of the future detector components.

The prototype and the future G-NUMEN detector are composed of a $LaBr_3$:Ce with the same dimension and produced by the same company (diameter ϕ = 38 mm, length $l = 50\,mm$). The PMT of the prototype is an R6231 Hamamatsu, with the same characteristics of the G-NUMEN detector. For the voltage divider, the prototype is powered by a D-type Hamamatsu E1198-26 while the one to be used for the future detectors is to be confirmed as it is still object of on-going and future test.

3.2.1. The scintillator

The core of the prototype is the $LaBr_3$:Ce crystal, an efficient and fast scintillation crystal used for high resolution gamma spectroscopy in several applications [21], [22], [23]. The main $LaBr_3$:Ce characteristics of interest for NUMEN are its excellent energy resolution and fast time response for which it has been preferred over other crystals such as LYSO or GAGG(Ce) [24], [6](see also Chapter 1).

The Cerium-doped lanthanum bromide crystals are hygroscopic inorganic scintillators of a new generation. Being hygroscopic, the crystals are provided in an Al casing closed with a glass window for the coupling with the PMT. The main properties of the $LaBr_3$:Ce produced by EPIC company are listed in Table 3.1.

Density [g/cm3]	5.20
Decay time [ns]	16
Light Output [Photons/MeV]	$68 \cdot 10^3$

Energy resolution @662 keV	< 3.5%
Melting Point [K]	1116
Wavelength of emission peak [nm]	380
Refractive index	1.9

Table 3.1 - Properties of LaBr3:Ce crystal produced by EPIC company [61]

The crystals show a very fast decay time and a high light output which provides their very appealing energy resolution. However, the high light output can lead to saturation of the electronics causing non-linear effects at gamma energies higher than 1-2 MeV [23], [25], [26], [27].

The $LaBr_3$:Ce have relatively high self-activity naturally caused by ^{138}La isotope, which decays by electron capture (EC) or β^-, and also by α-radioactive ^{227}Ac isotope whose percentage depends on the production process [28], [29](see 3.5). Even though the internal activity of the $LaBr_3$:Ce can affect the precision of the measurement, especially when low background are needed, the energy peak characteristics of the internal contamination can be used as reference in the study of the detector characteristics as it has been done in this work.

3.2.2. Prototype assembling

Two prototypes were assembled and characterized, both composed of a LaBr3:Ce crystal from EPIC and a R6231 PMT from Hamamatsu. The optical coupling of the PMT with the crystal was done using high viscosity optical grease. Since the PMT diameter ($\emptyset_{PMT} = 51\,mm$) is greater than the crystal external diameter ($\emptyset_{PMT} = 41\,mm$) a 3D printed ring was used to center the crystal with respect to the PMT. Both the crystal and the PMT have been wrapped with Teflon, aluminized Mylar and, finally, with a black tape for light shielding. This type of assembly provided the best energy resolution with the lowest environmental noise.

The alignment of the detector with respect to other detectors and/or radioactive sources was assured with a system of custom 3D printed holders.

The picture of the steps of the detector assembling and the holders used for the alignment are shown in Figure 3.2.

Figure 3.2 - From left to right: The crystal and the PMT have been covered with a white Teflon layer, an aluminized mylar layer and finally with a black tape.

3.2.3. The data acquisition system

The data acquisition system foreseen for NUMEN will be composed of new generation high performances digitizers VX2745 from Caen (64 ch., 125 MS/s) , which will be used for the data acquisition of the entire experimental apparatus (Focal Plane Detector and G-NUMEN array). These digitizers accept signals directly from the detectors, processing them in a digital way through the FPGA therefore simplifying the typical analog module chain. Moreover, each digitizer can process the signals from multiple detectors, up to 64 channels for VX2745, and it can synchronize the signals between channels and also with signals from other digitizers. In addition, a further advantage relies on the possibility to reduce the large quantity of data by selecting a priori only the events of interest. All these features are of particular interest for NUMEN since it will need to process data from more than 10^3 detectors: ~800 E-dE telescopes from the PID wall, ~ 300 signal from the Gas-Tracker anode pixels, ~ 100 LaBr3:Ce detectors from the G-NUMEN array (see Chapter 1).

The VX2745 can support both DPP-PHA (Pulse Height Analysis) and DPP-PSD (Pulse Shape Discrimination) acquisition mode, where the latter is more suited for fast timing scintillation detectors such as $LaBr_3$:Ce.

During this work the VX2745 digitizers were not available yet, and when they became available only the DPP-PHA firmware was released. For this reason, unless otherwise specified, the work presented in this thesis refers to data acquired with a desktop digitizer DT5720C (2 ch., 250 MS/s) from Caen, supporting a DPP-PSD firmware similar to the one which will be used for NUMEN.

The software used for the signal acquisition from the digitizer was CoMPASS (Caen) and the data were processed using the ROOT-CERN toolkit.

DPP - PSD firmware

It is worth introducing briefly the digital acquisition firmware used in this work since the choice of the signal process method was important for the optimization of the detector characteristics.

A digitizer working with a DPP-PSD firmware (Figure 3.3) integrates the charge of the input signals from the detectors. Once defining the baseline for the charge integration, the signals are identified if they reach a predefined threshold. This is called the "leading edge" identification method, and it is used by the DT5720C digitizer. Other digitizers, such as the VX2745, present the possibility to use the "constant fraction discrimination (CFD)" method to obtain more precise timing information.

In the case of the *Leading Edge* method, when the signal (subtracted by the baseline) reaches the trigger threshold it is selected and identified by a "Time stamp" with a

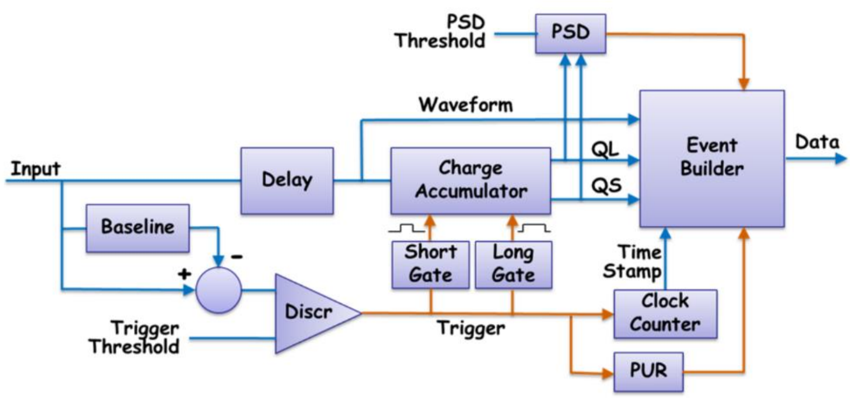

Figure 3.3 – Block diagram of the DPP-PSD firmware [59]

precision depending on the ADC sampling which corresponds, for example, to 8 ns for the VX2745 and to 4 ns for the DT5720C.

Using the *CFD* method increases the timing precision and it also avoid the "walk effects" which may occur using the leading edge method. With the CFD method the "Time stamp" is defined as the time at which the signal reaches a defined fraction of the full amplitude. The CFD of the digitizer works as the analogic CFD so the signal trigger corresponds to zero-cross of the CFD bipolar signal (the sum of the delayed and the inverted and attenuated signal). The timing precision is improved respect to the leading edge mode thanks to the introduction of the Fine Time stamp which is calculated as the linear interpolation of the signal samples before and after the zero crossing. The precision of the latter depends on the sampling period of the digitizer and it correspond to 8 ps for the VX2745 (there is no CFD mode for DT5720C).

The sum of the Time stamp (as evaluated with the leading edge method) and the Fine Time stamp is defined as the "interpolated zero crossing".

Regardless from the method used for the signal identification, for a PSD firmware the selected signal is then integrated through a pre-defined charge integration window (Gate). Figure 3.4 represents the typical waveform of the prototype acquired with the PSD firmware of the DT5720C digitizer. The total duration of the signal is ≤

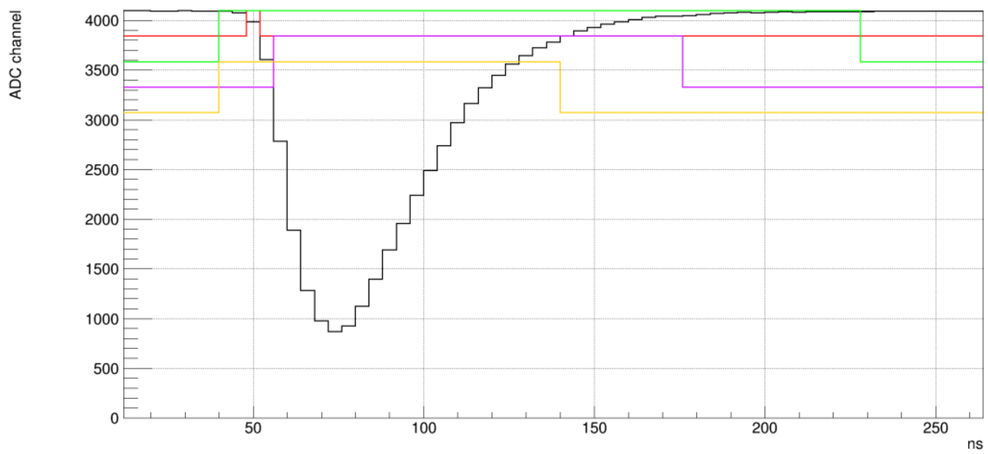

Figure 3.4 – Example of the waveform of the prototype acquired with the DT5720C digitizer (PSD firmware). The green line represents the charge integration Gate, the red line represents the trigger, the purple line is the trigger hold-off while the yellow line is the short gate used for the n-gamma discrimination.

150 ns and the charge integration window chosen for the acquisition, represented in green, is 180 ns.

From Figure 3.4 it can be noticed that the signal covers almost the entire dynamic range of the digitizer (~ 75% of the ADC channels). The latter is 2 Vpp while the average detector signal can be higher: the signal in figure refers to the ^{137}Cs peak (662 keV) meaning that the maximum signal amplitude which can be processed correctly from the digitizer corresponds to ~ 900 keV (see sec. 3.3.2). By decreasing the energy gain factor (gain = 160 fC/LSB), it is possible to acquire wider spectra at the cost of the linearity of the region above 900 keV. The VX2745 digitizer does not present this problem since the dynamic range is 4 Vpp which includes the average signal amplitude.

3.3. Characterization

The intrinsic background, the energy calibration and resolution, the photopeak efficiency were studied. The evaluation of these characteristics was done using the following radioactive sources: ^{152}Eu, ^{207}Bi, ^{22}Na, ^{137}Cs and ^{60}Co.

From now on, the two prototypes will be identified with CH0 and CH1. They were supplied with a $HV_{CH0} = -1050\,V$ and $HV_{CH1} = -1100\,V$, the value of the high voltage supply was chosen to optimize the energy resolution and the signal-to-noise ratio.

3.3.1 Intrinsic background

The intrinsic activity of the LaBr$_3$:Ce crystals is caused by the radioactive isotope ^{138}La (abundance = 0.0902%, $t_{1/2}$ = 1.05 · 10^{11} y) and to the contamination of ^{227}Ac and daughters [29], [30], [27]. The main and unavoidable contribution to the internal activity is linked to ^{138}La decay

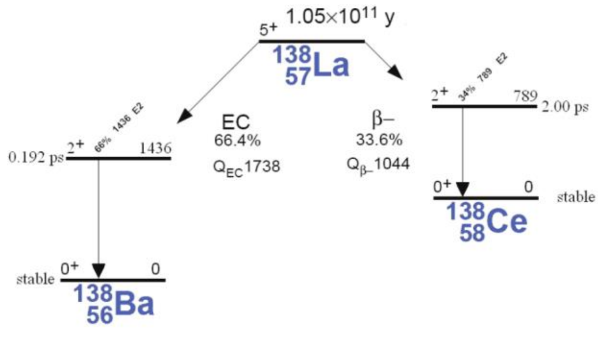

Figure 3.5 - Decay scheme of ^{138}La [60].

(Figure 3.5). The EC and β^- decay of ^{138}La contributes to the background spectrum with:

1. Low energy peaks from ε-decay of ^{138}Ba, related to the cascade products originated by the electron capture in the K and L atomic shells. The binding energies of these shells are 37.4 keV ad 5.6 keV, however these peaks are detected at the equivalent energy of 35.5 keV and 4.5 keV due to the non-proportional response of the $LaBr_3$:Ce crystal to x-ray radiations [31], [28]. The peaks can be detected when the gamma ray from the transition $2^+ \rightarrow 0^+$ at 1436 keV escapes the crystal;
2. A β continuum spectrum related to the ^{138}La decays into ^{138}Ce in which the 789 keV gamma has escaped the detector. The end point is 255 keV;
3. A Compton continuum spectrum in the region around 255 – 750 keV due to the contribution of both 789 keV and 1436 keV gammas;
4. A photopeak at E = 789 keV from the ^{138}Ce decay, widened due to the β spectrum emitted in coincidence, which results in a continuum region ending around 1 MeV;
5. A photopeak at E = 1436 keV from the ^{138}Be decay, which is detected in coincidence with the K and L cascades resulting in a wider peak around 1472 keV.

In addition to this background, the contamination of the ^{227}Ac produces alpha particles with an energy of gamma-ray equivalent in the range 1.6 – 3 MeV. The contribution of the ^{227}Ac is strongly influenced on fabrication processes and it may depend on the production company as well as on the crystal batch. The intrinsic activity can be evaluated by self-counting. Figure 3.6 shows the intrinsic activity of the prototype CH0 acquired for t = 52900 s.

The energy peaks at 1) and 2) can be easily identified and they correspond to the energy expected from literature: 4.5 keV, 35.5 keV and around 1472 keV. The contamination from ^{227}Ac is in the energy region 1.6 MeV – 3 MeV, as expected from literature. Its structure can be seen in the top right window of the Figure 3.6.

Table 3.2 lists some properties of the intrinsic background for both CH0 and CH1.

	CH0	**CH1**
Count rate [Hz]	~170	~230
Contamination [cps/cm³]	0.46 ± 0.02	1.28 ± 0.02
CPS at 35.5 keV	19.6 ± 0.2	20 ± 0.2
CPS at 1472 keV	4.3 ± 0.1	4 ± 0.1

Table 3.2 - Properties of the intrinsic background for the prototypes CH0 and CH1.

The self-counting spectra of the two prototypes have similar shape and properties except for the contamination CPS which is higher for CH1. However, this value is still below the maximum one assured by the production company (< 2 cps/cm³).

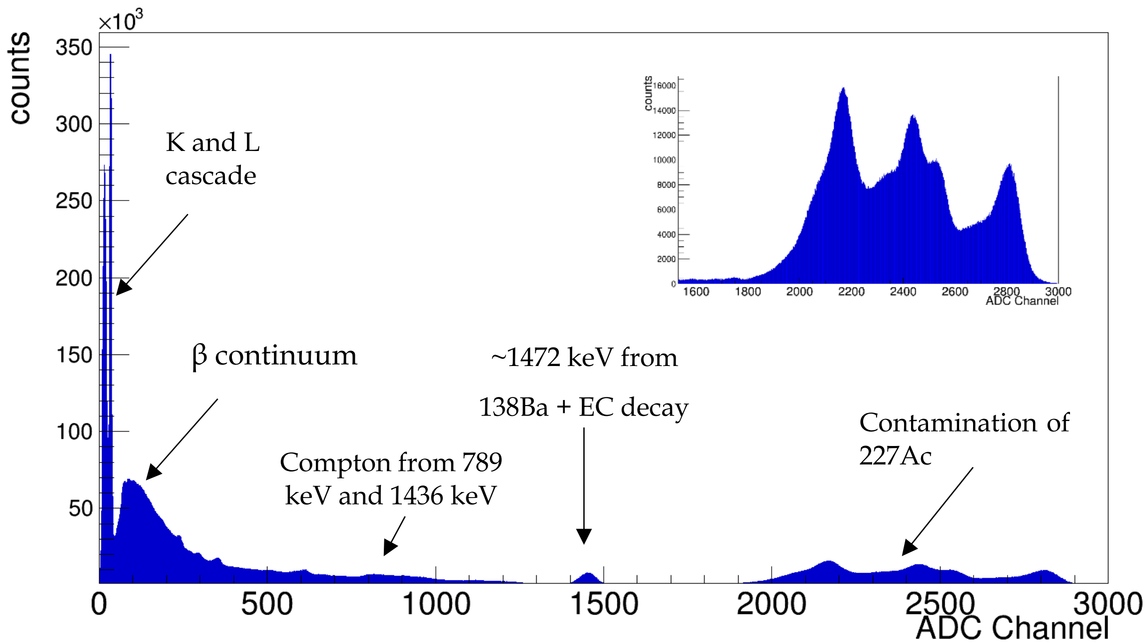

Figure 3.6 - Background spectra of the prototype CH0, acquired for ~15 hours. On the top right: zoom of the contamination contribution from ^{227}Ac.

3.3.2. Calibration and energy resolution

The calibration and the resolution curves of both prototypes have been evaluated using ^{152}Eu, ^{207}Bi, ^{22}Na, ^{137}Cs and ^{60}Co sources placed in a custom 3D printed holder (see Figure 3.7). The detection rate for each source spectrum acquisition has been kept below 4 kHz.

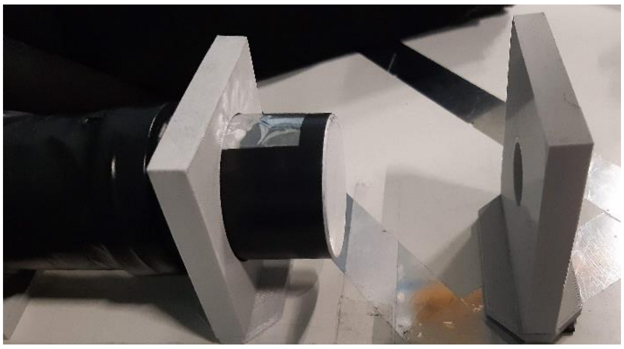

Figure 3.7 - Setup for the acquisition of the source's spectra. From left to right the detector and the source in their respective holders.

The calibration curves for both prototypes are shown in Figure 3.8. The elbow shown in the figure corresponds to the digitizer's saturation limit above mentioned and it is relative to the energy of E= 964 keV (^{152}Eu). The calibration curves were fitted with n-order polynomial functions considering n=1,2,3. For both detectors the R^2 factor is worst for n=3 while it is similar for n=1,2. As a title of example for CH0 $R^2 =$ 0.99981 for the 2-order polynomial fit while $R^2 = 0.9998$ for the 1-order polynomial

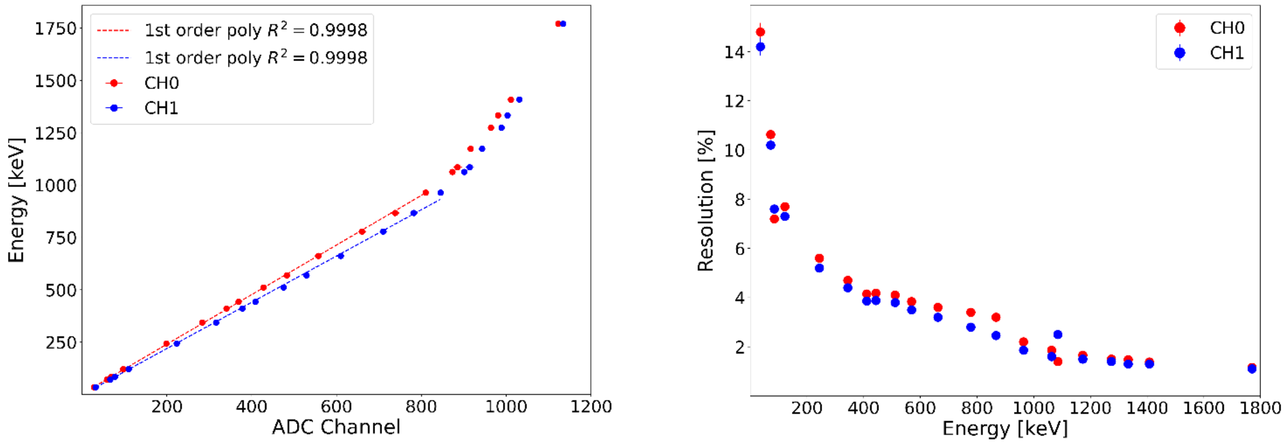

Figure 3.8 – On the left: Calibration curves for the two prototypes. The linear fits for the calibration curves of the two detectors are consistent and they corresponds to $E_{CH0}(keV) = 1.2ch + 4$ for CH0 and $E_{CH1}(keV) = 1.1ch + 1$ for CH1. On the right: Energy resolution of the two detector prototypes

fit. Figure 3.8 - left shows the 1-order poly fit and their factor of goodness $R^2$for both prototypes, while the resolution of the prototypes is shown in Figure 3.8 - right. As reference, the resolution at 662 keV for CH0 is 3.6 $\pm$ 0.05 % while for CH1 is 3.25 $\pm$ 0.05 %. This slight discrepancy can be ascribed to differences in the crystal's fabrication and/or in the optical coupling. These results are coherent with what expected from literature [32], [33].

3.3.3. Efficiency

The photopeak efficiency was evaluated using ^{22}Na, ^{137}Ca and ^{60}Co. The sources were placed at a distance *d* = 12.5 cm*. This is the distance at which the CPS of the energy peaks from the calibration source, as a function of the distance, starts to have a $\propto 1/d^2$ behavior (point-like approximation – see Fig. 3.9-left).

The photopeak efficiency has been evaluated as:

$$\varepsilon_{ph} = {CPS}/{(\varepsilon_{geom} \cdot A(t*) \cdot br)} \tag{3.1}$$

where ε_{geom} is the geometrical efficiency, $A(t*)$ is the activity of the source at the time t* of the measurement and br is the branching ratio associated to the energy peak. The results for the two prototypes, shown in the Figure 3.9- right, are consistent with each other within the error bars and they are in good agreement with the literature [33]. As a reference, the photopeak efficiency at 662 keV calculated in this work is (26.9 ± 0.8) % for CH0 and (25.5 ± 0.8) % for CH1 while the expected value is in the range 25-27 %.

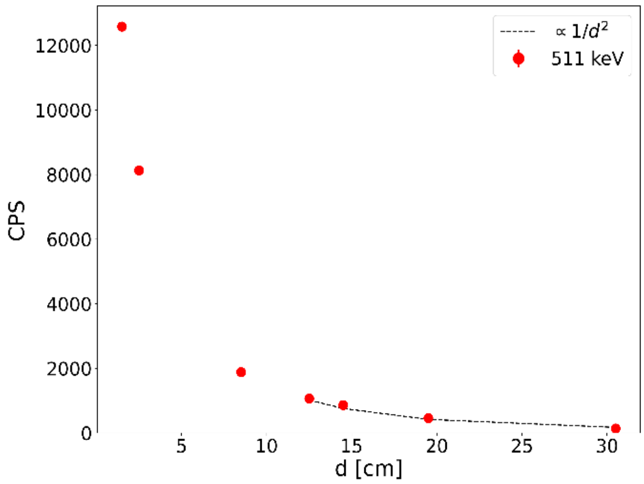

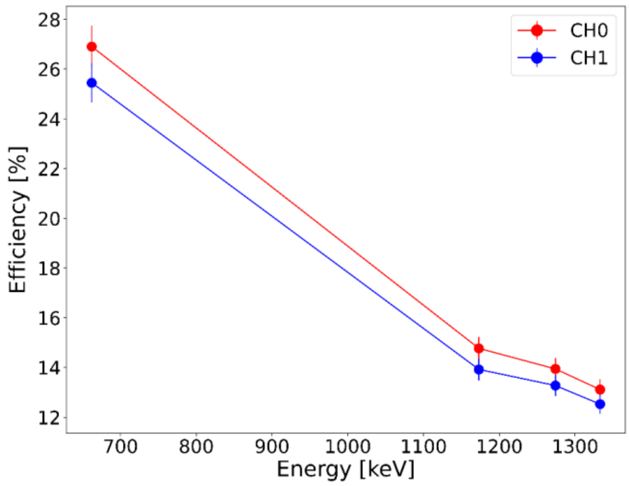

Figure 3.9 – On the left: Measurement of the CPS in the 511 keV peak as a function of the distance source-detector for the evaluation of the distance d* at which the point-like approximation is valid. The black dotted line represents the 1/d² fit. On the right: Photopeak efficiency of LaBr3:Ce for the two prototypes CH0 (red) and CH1 (blue).

3.4. Time coincidence and resolution

The aim of the future gamma array for NUMEN is to detect signal in coincidence with the projectile-like fragments detected in the Focal Plane Detector of the MAGNEX spectrometer, with a time resolution $\sim ns$ in order to be able to distinguish between the beam bunches (see Chapter 1). It is therefore important to study the feasibility of such coincidence in condition as similar as possible to the future NUMEN experiment. This section presents an experiment performed at LNS (INFN – Catania) for the study of a $LaBr_3$:Ce discrimination capabilities of a gamma signal triggered by a second signal from another detector in time coincidence.
In particular, measured were made of:

1) the gamma-gamma coincidence of the 511 keV annihilation peaks from a ^{22}Na source;
2) the gamma-particle coincidence from the reaction $^{10}B(n, \alpha)$.

In both cases the full energy spectra of the detectors were acquired and the coincidence was processed offline with a ROOT-CERN macro. The spectra obtained from the macro will be referred to as the 'coincidence' spectra.
It should be noted that this study was performed with a preliminary version of the detector prototype which was composed of the same $LaBr_3$:Ce crystal with a different light collection system. The digitizer used is the DT5751 Caen with a PSD firmware.

3.4.1. $\gamma - \gamma$ coincidence

The ^{22}Na source decays by emitting two annihilation gammas at 180 degrees respect to each other due to conservation of momentum (Figure 3.10- left). In these conditions, the gamma signal from the $LaBr_3$:Ce under study (CH1) is triggered by the coincident gamma signal detected by the second $LaBr_3$:Ce (CH0) placed at 180° (Figure 3.10 - right).

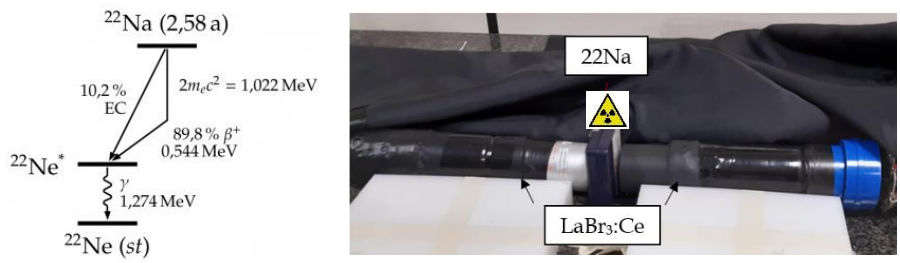

Figure 3.10 – On the left: ^{22}Na decay scheme. On the right: Experimental setup for the gamma-gamma coincidence test.

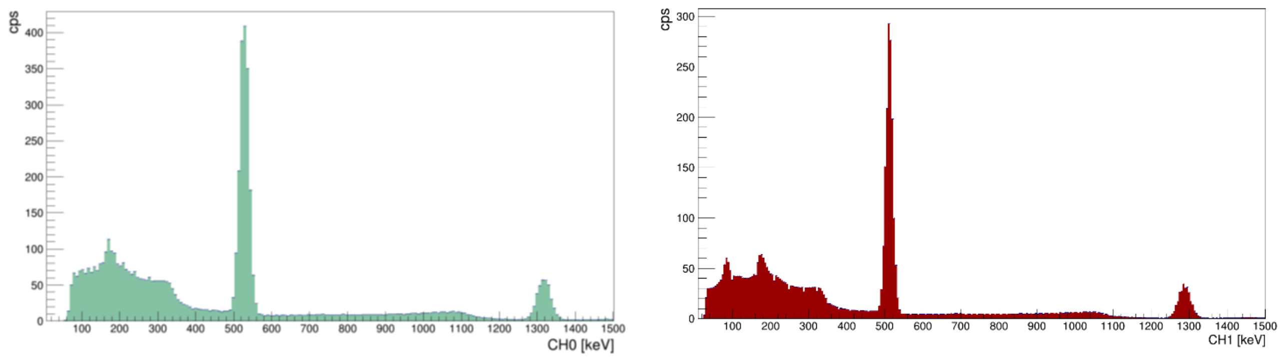

Figure 3.11 - Full energy spectra of the triggering detector CH0 (left) and the detector under study CH1 (right).

The full energy spectra measured of both detectors are shown in Figure 3.11 left (for CH0) and right (for CH1). The detection rate on both detectors is ~ 6 kHz, whose main component is the ^{22}Na characteristic decay (511 keV and 1274 keV).

The CPS in the energy peak of the signal of interest at 511 keV is ~300 evt/s for both detectors, therefore the signal-to-noise S/N ratio in the full energy spectrum is S/N = 0.05. Both the triggering detector and the one under study are in similar experimental conditions. Figure 3.12 shows the scatterplot of the coincidence events between the two detectors in a time window $\delta t_c = 30\ ns$. The true coincidence events are the ones for which both CH0 and CH1 detect the 511 keV photopeak (red ROI in Fig. 3.12) and are $CPS_{p-p} = 157\ evt/s$; all the events of CH1 in coincidence with the 511 keV peak in CH0 are $CPS_{511} = 417\ evt/s$ (black dotted ROI). Therefore, the S/N ratio of the coincidence spectra gated on the CH0 signal is $(S/N)_{\gamma\gamma} = 0.37$. The coincidence efficiency ε_{p-p}^{511} can be defined as the ratio between the number of the peak-peak coincidences measured and expected:

$$\varepsilon_{p-p}^{511} = \frac{(\#evt_{ROI(p-p)})/s}{A \cdot br \cdot \varepsilon_g \cdot \varepsilon_p^{CH0} \cdot \varepsilon_p^{CH1}} \tag{3.2}$$

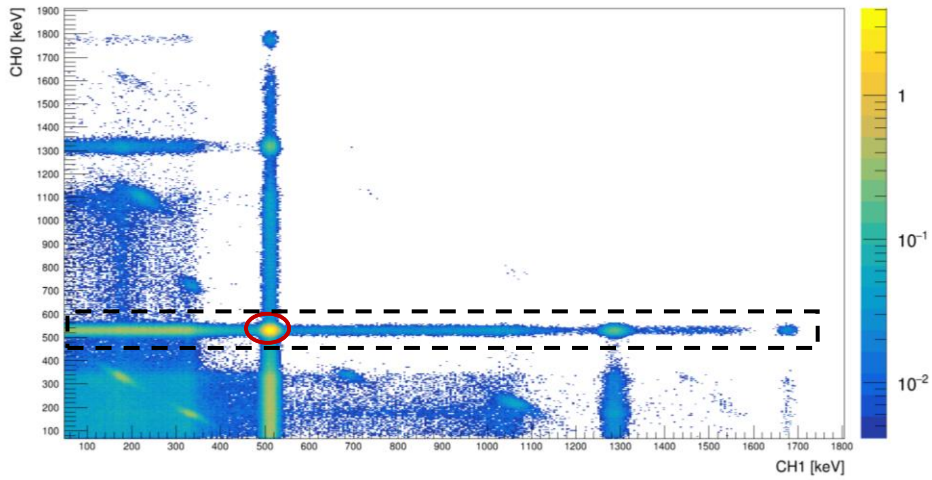

Figure 3.12 - Scatterplot of the coincidence events from the two detector CH0 (y-axis) and CH1 (x-axis).

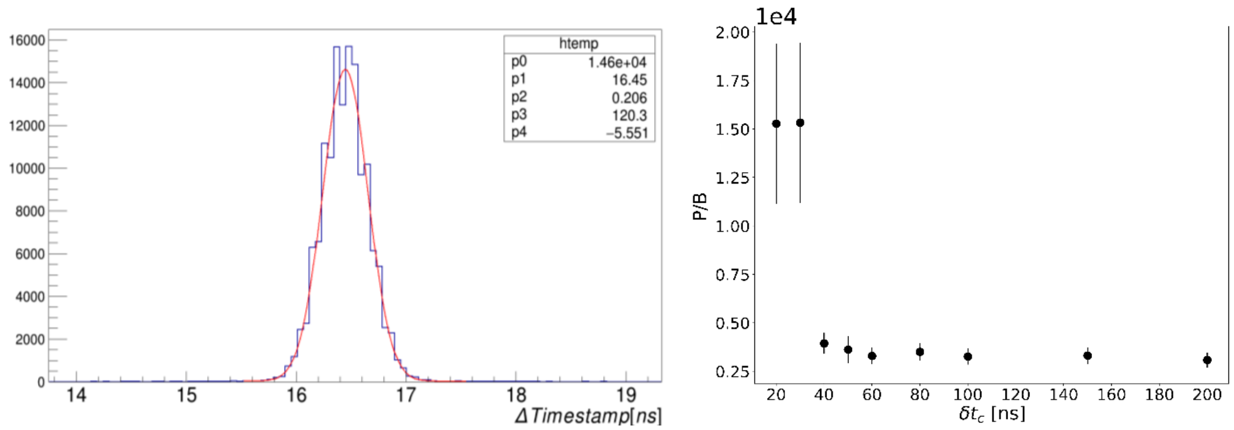

Figure 3.13 – On the left: Time spectra of the coincidence events in the 511 keV- 511 keV peak region. On the right: Peak-to-Background ratio of the coincidence time spectra evaluated at different time windows.

Where $\#evt_{ROI}$ is the number of events in the ROI (511-511), ε_g the geometric efficiency, ε_p^{CH0} is the photopeak efficiency at 511 keV, A is the activity of the ^{22}Na source, br the branching ratio of the 511 keV peak. For this experiment $\varepsilon_{p-p}^{511} = 25\%$. This can be used as reference value for the goodness of the coincidence discrimination (for the given geometrical configuration). In fact, in this situation the energy spectra of both detectors are composed mainly by the signal of interest, therefore the random coincidences are negligible, and the number of coincidence events is the maximum possible.

The time spectrum of the coincidence events in the ROI (511-511) is shown in Figure 3.13 (left). The sigma of the fit gaussian + (1-order)poly is σ = 206 ps. It can be noticed that the random coincidences (linear background) are negligible as expected.

The value of time window δt_c of the coincidence events was chosen to optimize the peak-to-background ratio P/B of the time spectrum (see Figure 3.13– right).

3.4.2. $\alpha - \gamma$ coincidence

The feasibility of the time coincidence was studied using a gamma signal in the $LaBr_3$:Ce triggered by a charged particle signal from a Si detector. A boron layer 2 µm thick (95% ^{10}B, 5%^{11}B) was mounted on the top of a 300 µm Si detector (30 x 30 mm^2). The $LaBr_3$:Ce and the Si detectors are placed inside the shielding case of a Am-Be source of A = 37 GBq (see Figure 3.14).

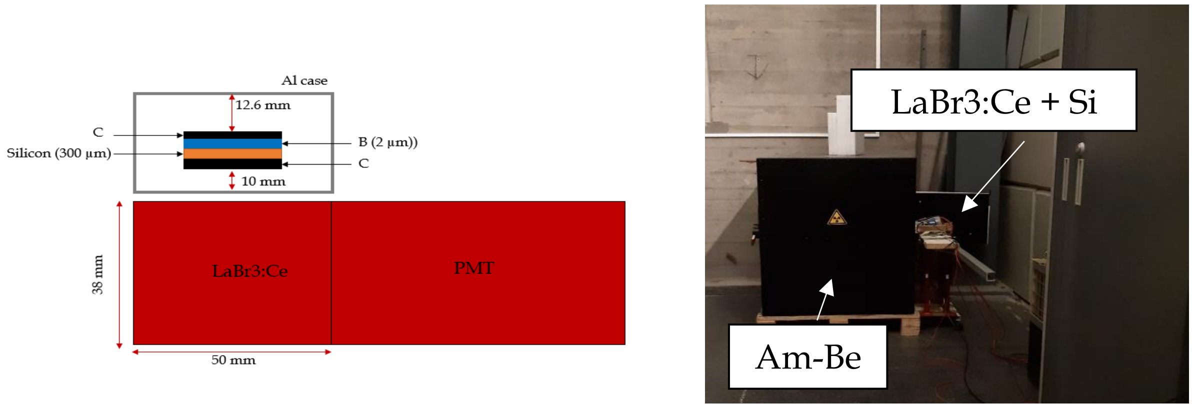

Figure 3.14- Experimental setup for the coincidence measurement of the 481 keV gamma signal in the LaBr3:Ce triggered by the α particle produced in the $^{10}B(n,\alpha)$ reaction. On the left: scheme of the geometric configuration of both detectors. On the right: picture of the experimental set up. The detector is placed inside the shielded Am-Be source.

The neutrons emitted by the source imping on the Boron layer, triggering the reaction $^{10}B(n,\alpha)$ where the alpha particles are emitted in coincidence with a gamma at E = 481 keV. The full energy spectra of both detectors are shown in Figure 3.15. The Si spectrum is in good agreement with what is expected from literature [34]. The total detection rate in the $LaBr_3$:Ce is extremely high(~280 kHz) and can be seen that the 481 keV peak is not resolved.

The coincidence spectrum of the $LaBr_3$:Ce is shown in Figure 3.16-left while Figure 3.16 - right shows the scatterplot of the coincidence events α-γ. The time window is $\delta t_c = 200\, ns$ and it was chosen with the same method discussed above. The total number of coincidence events gated on the α spectrum of the Si detectors is CPS = 2.5 evt/s while the coincidences in $LaBr_3$:Ce energy region corresponding to the E =

481 keV peak (red ROI in Fig. 3.16) are CPS_{481}=0.15 evt/s, therefore the signal-to-noise ratio of the $LaBr_3$:Ce coincidence spectra gated on the alpha spectrum is $(S/N)_{\alpha\gamma}$ = 0.06. The time spectrum of the coincidence events in the above-mentioned ROI is shown in Figure 3.17. The sigma of the gaussian fit of the peak is σ = 6.2 ns. The constant background in the time spectra is representative of the random coincidences and it has been fitted with a 1-order polynomial. The P/B at FWHM is ~ 2.5.

Even though the energy peak at 481 keV was not resolved in the full energy spectrum, it was still possible to discriminate the signal of interest by studying the coincidence events within a time window of 200 ns. The $(S/N)_{\alpha\gamma}$ of the coincidence spectra is much lower than in the previous case $(S/N)_{\gamma\gamma}$, however it was still possible to identify the events of interest. The difference in the σ of the time spectrum gaussian fit (σ = 206 ps for the γ-γ test and σ = 6.2 ns for the α-γ ones) can be ascribed to the longer signal duration of the particle detector with respect to the $LaBr_3$:Ce and to an non optimal acquisition system for the particle detector.

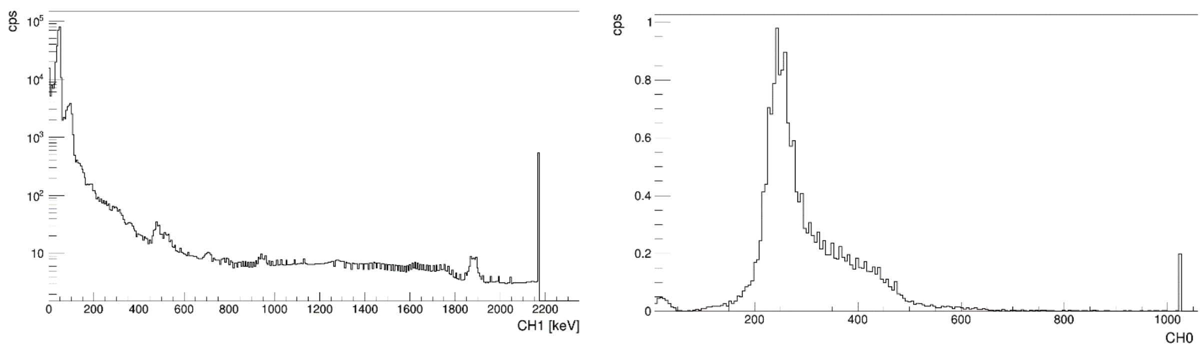

Figure 3.15 - Full energy spectra of the LaBr3:Ce detector (left) and of the Si detector (right).

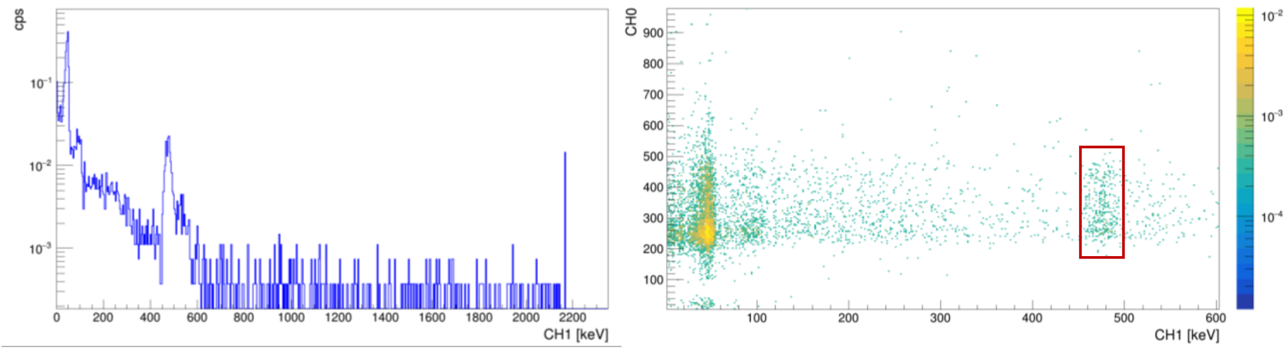

Figure 3.16 – On the left: Full energy spectra of LaBr3:Ce in a time window of 200 ns. On the right: Scatterplot of the full spectra of CH0 (Silicon detector) versus CH1 (LaBr3:Ce).

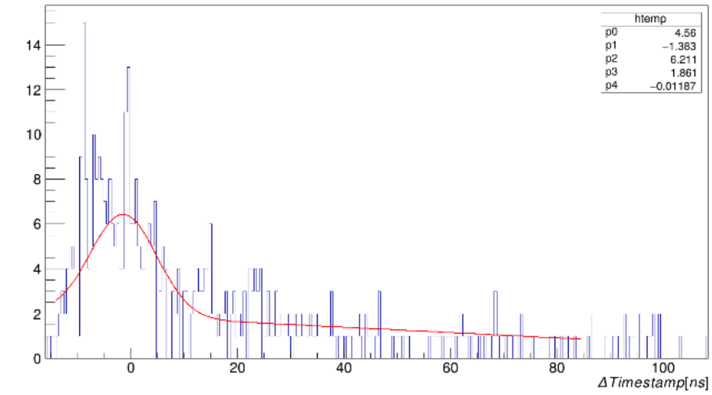

Figure 3.17 - Time spectra of the coincidence events between the alpha particles and the 481 keV peak.

3.5. Rate dependence

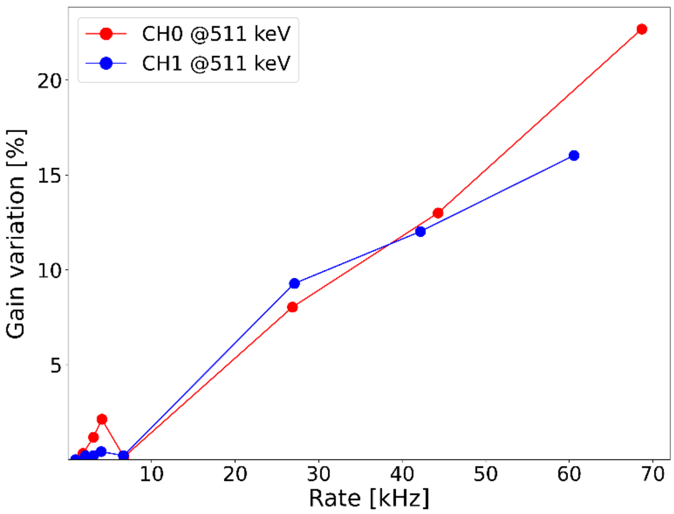

Figure 3.18 - Variation of the gain at 511 keV respect to the point at lower detection rate.

The evaluation of the worsening of the detector performances at increasing detection rate is crucial since the G-NUMEN array will be used in all the cases in which the detection rate is expected to reach ~300 kHz per detector.

The properties of the detectors may vary with the detection rate due to different factors:

- The detection rate can affect the detector gain. This effect might be ascribed to an abrupt decrease of the collection efficiency due to the saturation of the anode-to-dynode current ratio [35], [36].
- The time resolution, as well as the coincidence efficiency, might also depend on the detection rate due to the increase of the uncorrelated events detected in the time coincidence window.

3.5.1. Energy characterization

The gain at the energies of the calibration sources was measured at different detection rate by varying the distance source-detector and therefore increasing/decreasing the overall rate on the detectors. The rate dependence of the gain for the 511 keV peak of the ^{22}Na is shown in Figure 3.18. For detection rate of ~ 70 kHz, the gain can have a variation greater than 20% respect to the point at the lowest detection rate (~Hz). However, in the range 0 – 10 kHz the variations are less than 3% and the gain can be considered stable.

Figure 3.19 shows the calibration curves for one prototype for different detection rates of the calibration points. The black points refer to calibration sources acquired at high detection rate between 70-80 kHz while the red points are acquired at rate of few Hz. It can be noticed that this effect is non-linear with the energy: the percentage variation mitigates at increasing energy. At E = 867 keV (^{152}Eu) the variation is ~30 % while at E = 74 keV (^{207}Bi) the peak centroid increases almost of a factor of 3. The gain variations affect the energy resolution, as it can be noticed in Figure 3.20. The resolution at E = 74 keV varies from 7.3% to 15.3% while it increases from 3.7% to 3.2% at E = 867 keV (see Figure 3.20).

The non-linearity with the energy of the detector can be ascribed to the very high current peak induced by the LaBr3:Ce crystal in the PMT itself [37], [38] and it can

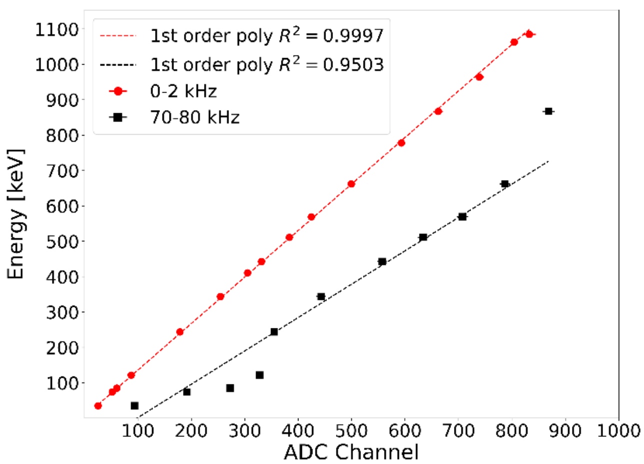

Figure 3.19 - Calibration of CH1 at low (red) and high (black) detection rate.

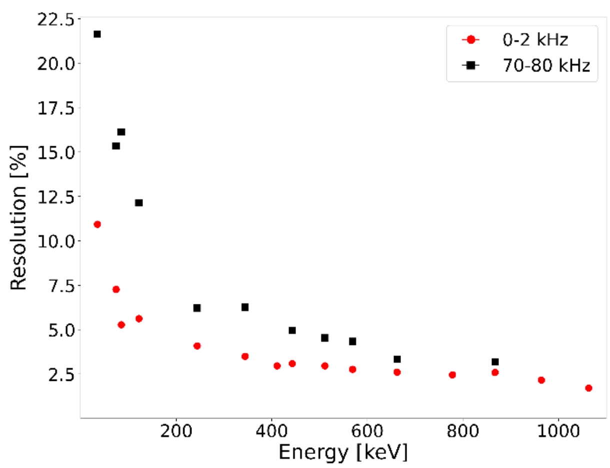

Figure 3.20 - Resolution of CH1 evaluated at low (red) and high (black) detection rate

depend on the type of voltage divider . The latter can also affect the detector response at high rate (see sec. 4.5).

3.5.2. Time coincidence

The discrimination capabilities of the detector can be affected by the detection rate since the random coincidences in the selected time window can increase. The γ-γ coincidence were evaluated following the same procedure illustrated in section 1, at increased detection rate on CH1. The signal to be discriminated by the detector CH1 is the 511 keV peak from the ^{22}Na source, triggered by the coincident 511 keV on CH0. An additional source ^{137}Cs was added near CH1 to increase the random background and therefore the total detection rate which was ~ 80 kHz (Figure 3.21).

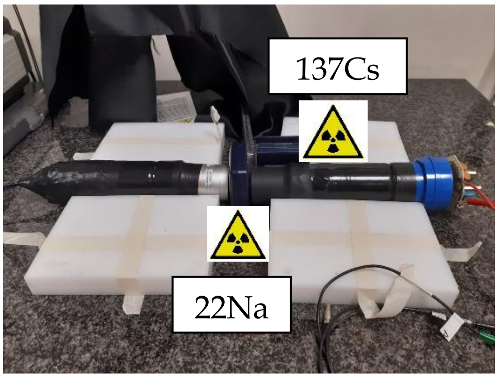

Figure 3.21 - Experimental setup for the coincidence study at high detection rate.

While the full energy spectrum of CH1 is dominated by the decay peak of 137Cs at 662 keV (S/N < 0.04), the 511 keV signal can be easily identified in the coincidence spectrum (Figure 3.22).

The scatterplot of the coincidence events CH0 vs CH1 is shown in Figure 3.23. The S/N ratio for the coincidence spectra as defined above is S/N = 0.36, similar to what obtained for low detection rate. The coincidence efficiency is ε_{p-p}^{511} = 38% while ε_{p-p}^{511} = 25% for low detection rate. Since the geometry is the same for both tests, this increase is representative of the increase of the random coincidence in the ROI(511 – 511). However, the contribution of the random coincidence in the 511-511 ROI is still negligible as seen in the time spectrum in Figure 3.24: the continuous background is negligible with respect to the events in the peak The sigma of the Gaussian peak of the time spectrum distribution is σ = 215 ps, similar to the value at lower detection rate (σ = 206 ps).

In conclusion, the discrimination capabilities of the detector under a total detection rate of ~ 80 kHz do not differ significantly from the ones at low detection rate (~ 5 kHz) in the same experimental condition. However, in this test the detection rate reached was much lower than the one expected in NUMEN (~300 kHz); in addition the events used to increase the detection rate mainly involve a narrow region of the energy spectrum (peak at 662 keV) therefore, they do not reproduce properly what will happen in the NUMEN experiment where the high rate will be due to a background composed by low energy neutrons and several gamma peaks at different energies [6]. The α-γ test was performed in more similar conditions to the foreseen NUMEN experiment, however it was not possible to study the rate dependence of the α-γ discrimination capabilities since the background rate is fixed by the AmBe source geometrical configuration. A detailed study of the detector discrimination capabilities and its rate dependence can be found in Chapter 4.

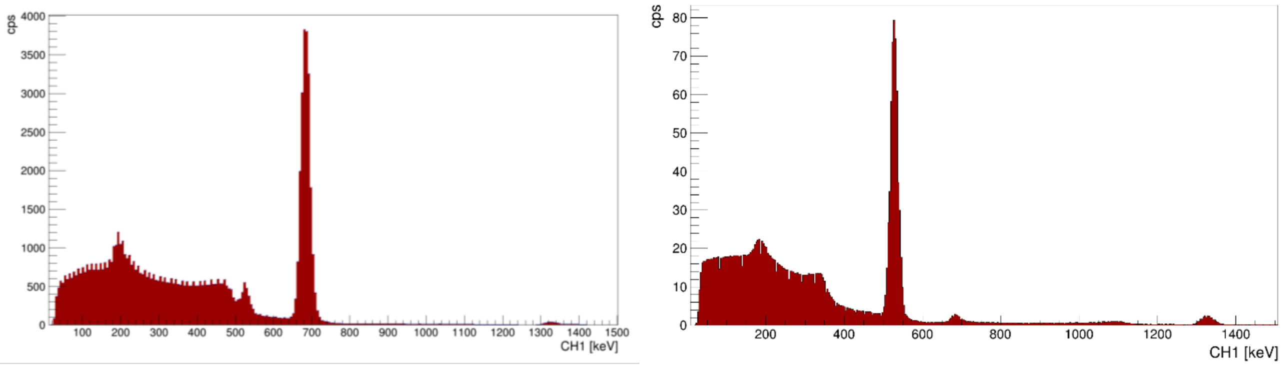

Figure 3.22 - Full energy spectrum (left) and coincidence spectrum (right) of CH1. The coincidence events of the spectrum on the right were evaluated within a time window of 30 ns.

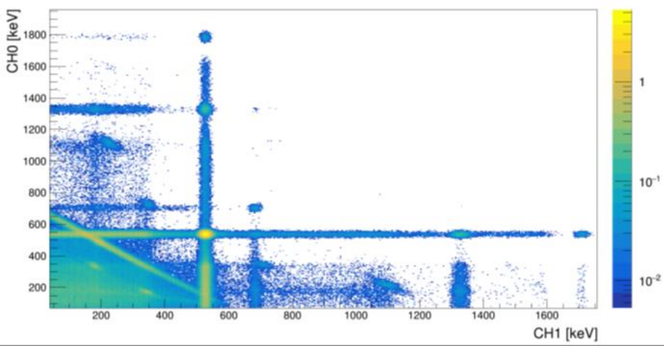

Figure 3.23 - Scatterplot of coincidence events between CH0 and CH1.

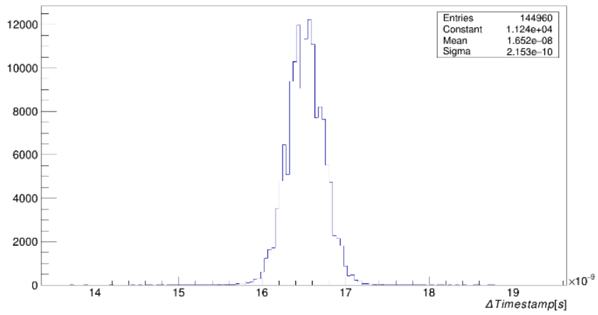

Figure 3.24 - Time spectrum of the coincidence events in the ROI (511-511). The random coincidences are negligible.

4. High Intensity Test of $LaBr_3$:Ce detectors: In-beam study

The in-beam High Intensity Test (HIT) of the $LaBr_3$:Ce detector aims at evaluating the performance of the G-NUMEN detector prototype in experimental conditions similar those foreseen in NUMEN. It is a feasibility study of the prototype performances involving the two main key aspects of the G-NUMEN array: 1) the time and energy resolution and 2) the resistance to harsh environments.

The study of the radiation damage is presented in Chapter 5. This chapter deals with the study of the time and energy resolution of the detector under increasing detection rate. In particular, the section 4.1 discusses the motivations for this study, the section 4.2 presents the design of the experiment while section 4.3 shows the results. The HIT experiment was carried out at the ALTO facility of the IJC Laboratory (Université Paris-Saclay).

4.1. Motivations

The low cross section of the DCE reactions requires very high beam intensity ($10^{12} - 10^{14}\ pps$) and long period runs (see also chapter 1). On the one hand, the high intensity is needed to get high statistics in order to identify DCE events, on the other hand this will increase the overall radiation production especially in the target area, where G-NUMEN will be placed.

G-NUMEN will be used to discriminate DCE events for all the reactions at high energies, involving moderately and heavily deformed mass nuclei, for which the MAGNEX detection apparatus does not have the adequate energy resolution to distinguish between the ground states ($I^{\pi} = 0^{+}$) and the first excited states ($I^{\pi} = 2^{+}$) of both projectile and target. In all these cases, the simulations show that the expected detection rate on each of the 105 $LaBr_3$:Ce detectors is ~300 kHz, depending on the specific reaction.

An example of one of the reactions for the $\beta^{-}\beta^{-}$ investigation, which will require the use of G-NUMEN, is:

$$^{116}Cd(^{20}Ne, ^{20}O)^{116}Sn \tag{4.1}$$

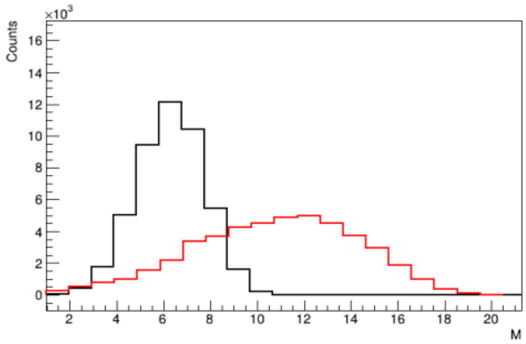

Figure 4.1 – Simulated emission multiplicity of neutrons (black) and gamma (red) for the reaction 4.1 [6].

Of course, there are several other possible channels other than DCE events which can be opened in this reaction, with cross sections much higher than DCE, which represent the background of the measurement. Considering a ^{116}Cd target of 1.4 mg/cm^2, a^{20}Ne beam of energy 230 MeV and intensity 10^{12} pps, the emission rates for gammas and neutrons for all the possible reactions channels are respectively 240 MHz and 140 MHz. The average γ and n multiplicity multiplicities are $M_{\gamma} = 12$ and $M_{n} = 6$, which might slightly change depending on the beam energy and/or the target backing (Figure 4.1). For example, in the case of 600 MeV, the distribution of the gamma multiplicity is wider and the average is reduced to $M_{\gamma} = 10$ [6].

The simulated detection rate in each $LaBr_3$:Ce is ~300 kHz with a very populated energy spectrum, especially in the low energy region (Figure 4.2). The simulation shows that from the coincidence of the G-NUMEN and FPD signals, it could be possible to distinguish the transitions of interest for the DCE. Figure 4.3 shows the coincidence spectrum of the gamma array in which it is possible to separate the peak at 463 keV and 1674 keV representative of the target like fragment transition $0^{+}(2)$ and 2^{+} respectively.

The results of the several simulation studies of the detector performances are promising [6], [3], [20], [19], however there is no experimental test of the actual in-beam response of the detectors of the G-NUMEN array. As demonstrated in Chapter 3, the performances of these detectors can be strongly affected by the detection rate, therefore it is of fundamental importance to assess the suitability of the detectors response at high detection rate, under experimental conditions as similar as possible to those expected in NUMEN. In particular, this task mainly involves the study of the energy and time resolution of the detectors at increasing detection rate to verify their suitability for the NUMEN experiment.

For a correct identification of the energy peak of the transitions of both PLF and TLF, the resolution of the detectors must be below 10% in the energy region of 200 keV while the time resolution must be of the order of ns to be able to perform the time coincidence with the signals of the FPD detected within the same beam bunch.

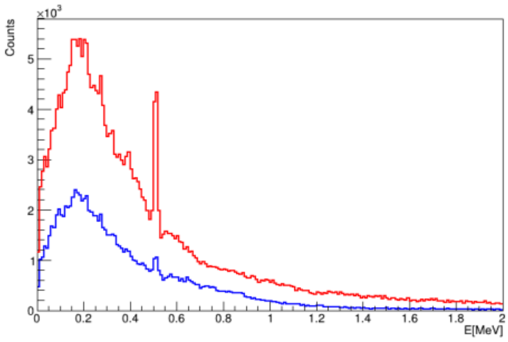

Figure 4.2 - Simulated LaBr3:Ce spectra of the reaction $^{116}Cd(^{20}Ne,^{20}O)^{116}Sn$ at 300 MeV. The difference between the lines is in the presence (red) or not(blue) of a carbon target backing [6].

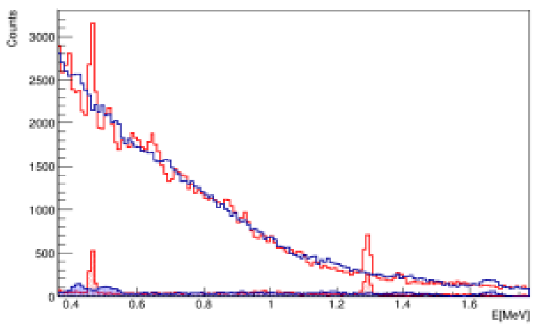

Figure 4.3 - Simulated spectrum of the gamma array for the reaction $^{116}Cd(^{20}Ne,^{20}O)^{116}Sn$ at 300 MeV, in coincidence with the PLF signal in the FPD. Red and blue lines differ from the Doppler correction [6].

4.2. The experiment

The aim of the HIT experiment is to study the response of the detector prototype in conditions similar to the one expected in NUMEN. Other than studying the energy resolution at increasing detection rate, the main purpose is the measurement of the time resolution of the detector, which is one of the key aspects of the future gamma array. In particular, the aim is to study the time resolution of the coincidence between two signals, while the prototype is exposed to a high background detection rate composed by both gammas and neutrons, as in the case of NUMEN (see 4.1).

In this chapter it is presented the study of the detector characteristics at increasing detection rate by exploiting the fusion evaporation reactions (^{16}O + ^{58}Ni) and (^{16}O +

^{107}Ag) as a source of background, over which the coincidence of the signals coming from a ^{22}Na source were measured.

In fact, a fusion-evaporation reaction provides a background very similar to what expected in NUMEN, being composed by both neutrons and gammas with variable multiplicity and with energy spectra wide but mainly peaked in the low energy part (as in the case shown in sec. 4.1). In addition, an advantage of using a background produced by a beam is the possibility to change the detection rate by modulating the intensity of the beam. In this way it was possible to perform a punctual study of the detector characteristics as a function of the detection rate. The signal, to be detected in coincidence over the background produced by the fusion evaporation reaction, as previously mentioned, was produced by a ^{22}Na source which emits in coincidence two annihilation gammas at 511 keV back-to-back.

The energy resolution, the time resolution and the coincidence efficiency of the prototype described in Chapter 3 were studied under an increasing detection rate up to 310 kHz.

4.2.1. The ALTO facility

The HIT experiment was performed at the ALTO facility of the Iréne Joliot-Curie Laboratory. The facility is used for several multidisciplinary applications thanks to the diversity of beams and the numerous beam line available. It consists of two accelerators: an electron linear accelerator for the production of radioactive beams [39] and a Tandem accelerator [40]. The latter was used for the experiment presented in this Chapter. The Tandem of ALTO (Figure 4.4) is a 15 MV Van de Graaf accelerator whose acceleration element is based on the “ladderton” charging belt. It can produce a large variety of stable beams, from protons to heavy ions and neutrons, using a “sputtering” or a “duoplasmatron” ion source. The beams are continuous, but they can be pulsed using a chopper on the injector obtaining beam bunches of few nanosecond width and periods of 100, 200 and 400 ns. The beam used for the experiment here presented was a $^{16}O^{7+}$ beam with a maximum intensity of ~ 400 enA.

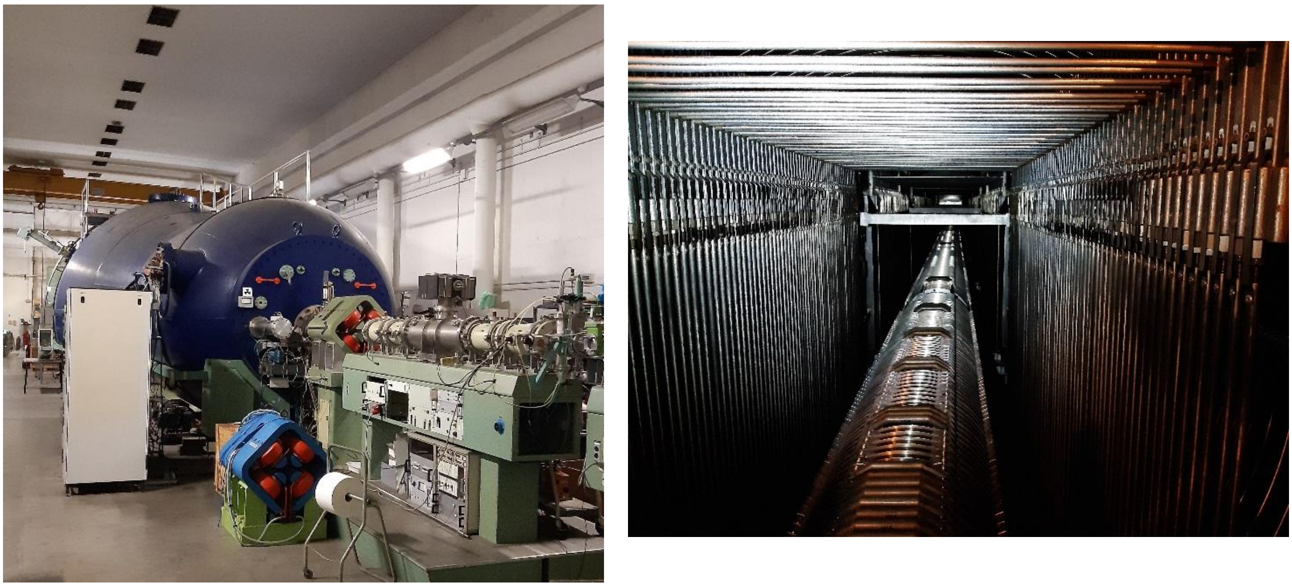

Figure 4.4 - On the left: Pictures of the Tandem. On the right: Detail from the inside of the acceleration column.

4.2.2. The fusion-evaporation reactions

For the choice of the fusion evaporation reaction to use, several possibilities were studied considering different parameters.

In order to have high fusion evaporation cross section and therefore a substantial gamma and neutron production, the beam must have an energy of at least 5-6 AMeV to assure an excitation energy of the compound nuclei in the range 50 -100 MeV. Moreover, to reduce the cross section of the fission reaction respect to the ones of the fusion-evaporation channel, beams of relatively light ions were preferred, combined with targets for which the total mass of the compound nuclei was ~ 100.

The gamma and neutron multiplicity must also be considered: for a typical NUMEN experiment the multiplicity is higher for gammas than for neutrons and their average value can slightly change with the type of reaction, the beam energy and/or the target backing. For these reasons, considering also the beam availability of the ALTO facility and the maximum current possible for each isotope, it was chosen a $^{16}O^{7+}$ beam to produce two reactions with different gamma/neutron multiplicity.

The parameters of the reactions are listed in Table 4.1.

	$\sigma_{F-E}[mb]$	E [MeV]	Target thick. [mg/cm^2]	Multiplicity		
				γ	n	γ/n
1) $^{16}O^{7+}$ + ^{107}Ag	1351	119	25	13	3	4.3
2) $^{16}O^{7+}$ + ^{58}Ni	1233	119	18	8	0.8	10

Table 4.1 - Parameter of the fusion evaporation reaction used in the HIT experiment.

The cross section for the fusion evaporation reactions were calculated with an algorithm based on the Bass model [41]. The angular distribution of the reaction products and the gamma and neutron multiplicity were calculated using the LILITA and Cascade evaporation codes.

For an intensity of the oxygen(7+) beam of ~350 enA and considering natural targets of Ag (^{107}Ag at 52%) and Ni (^{58}Ni at 62%), the calculated expected emission productions at 4π for the two reactions are listed in Table 4.2.

	$\boldsymbol{Rate\ \gamma}\ [\boldsymbol{MHz}]$	$\boldsymbol{Rate\ n}\ [\boldsymbol{MHz}]$
1) $^{16}O^{7+}$ + ^{107}Ag	400	90
2) $^{16}O^{7+}$ + ^{58}Ni	370	40

Table 4.2 – Total emission rate of gammas and neutrons calculated using the LILITA and Cascade codes.

While the gamma emission is isotropic, the neutrons distribution is angular dependent, therefore the position of the detector strongly affects the neutron detection rate. The expected detection rate for both gammas and neutrons is discussed in the next section.

4.2.3. Experimental setup

The $^{16}O^{7+}$ was transported to a "in-vacuum" scattering chamber where the targets were placed.

The detector under study and the triggering detector were outside the chamber, at a given angle θ with respect to the beam axis (Figure 4.5).

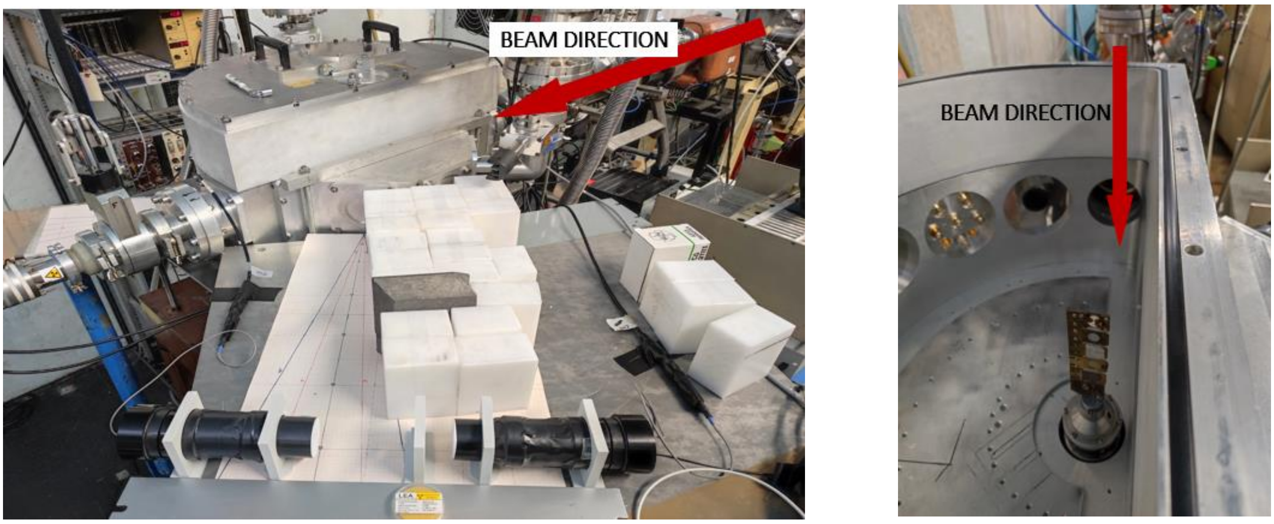

Figure 4.5 - Pictures of the experimental setup for the HIT experiment. On the left: the detectors are placed outside the reaction chamber, at 40 cm from the target. On the right: picture of the targets inside the scattering chamber.

The signal to be measured for the evaluation of the time resolution is produced by a ^{22}Na, emitting two annihilation gammas back-to-back at 511 keV. The source was placed between the detectors in a configuration similar to the one presented in chapter 3.

In order to reproduce a situation similar to NUMEN between the FPD and the G-NUMEN array, the detector under study (CH1) was exposed to the background produced by the fusion evaporation reaction, while the detector used as a trigger (CH0) was partially shielded (Figure 4.6).

In this configuration, by increasing the beam intensity it is possible to increase the detection rate mainly on CH1. This increase involves only the background while the production of the signal to be detected in coincidence come from the radioactive source and it is therefore independent.

The ^{22}Na must be shielded from the neutron background coming from the fusion-evaporation reaction to avoid reactions inside the source. This constraint influenced both the angular position and the distance from the target of the detectors and the source. On the one hand, the detector under study must be exposed to high fluxes of both gammas and neutrons to reach the desired detection rate, on the other hand the detector must be in the proximity of the ^{22}Na source to detect the coincidence signal and the neutron flux on the source must be minimized.

According to the calculation of the expected neutron and gamma energy and angular distributions and emission rate performed with the LILITA and Cascade evaporation algorithms, and considering the mechanical constraints of the experimental setup, the best configuration for the angular position of the source and the detector CH1 is respectively $\theta_S = 50°$ and $\theta_{CH1} = 40°$ (with respect to the beam axis).

A conservative evaluation of the neutron rate on source (diameter of 5 mm) at $\theta_S = 50°$ for a beam intensity of 500 nA is R_n(Ni) = 2 kHz in the case of the Ni target and R_n(Ag) = 1 kHz. The energy spectra of the neutrons for both reactions at $\theta_S = 50°$ is shown in black in figure 4.7.

A good shielding material for fast neutrons is the PTE whose neutron attenuation coefficients are well known in literature [42]. The neutron spectra after a 40 cm PTE shielding is shown in red in Figure 4.7, and it is negligible. The CPS of the neutron are < 1 Hz. Considering a total of 40 hours of beam time for both the reaction, the number of ^{22}Na nuclei (A(^{22}Na) = 210 kBq) and the absorption cross section σ ~ b [TENDL] (conservative assumptions), then it is possible to calculate the number of reactions in the source

$$\#_{reac} = \#_n \cdot \#(^{22}Na_{nuclei}) \cdot \sigma_{abs}$$

which is below negligible, therefore the 40 cm of PTE is correctly shielding the source. In addition to the PTE, a 5 cm lead shielding was used to reduce the gamma radiation on both the source and CH0.

The distance of CH1 from the target was x = 45 cm. Table 4.3 lists the maximum expected detection rates on CH1 for the two reactions considering a beam intensity of ~ 350 nA.

	$\boldsymbol{\gamma\ det.rate\ [kHz]}$	$\boldsymbol{n\ det.rate\ [kHz]}$	$\boldsymbol{TOT\ det.rate\ [kHz]}$
$\boldsymbol{^{16}O^{7+} + {}^{107}Ag}$	170	40	210
$\boldsymbol{^{16}O^{7+} + {}^{58}Ni}$	160	110	270

Table 4.3 – Calculated detection rate on CH1 from the reaction with the silver and nickel target considering an oxygen-16 beam intensity of 350 nA.

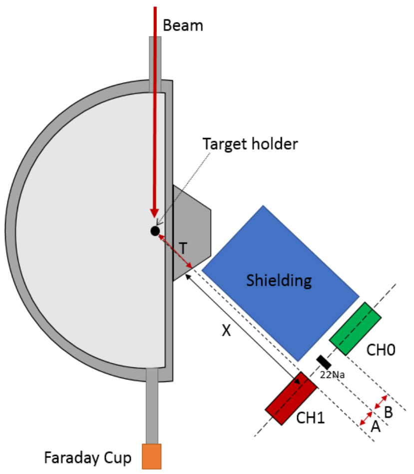

Figure 4.6 - Sketch of the experimental setup for the measurement of the coincidence signal from a ^{22}Na source over the background coming from the fusion evaporation reaction.

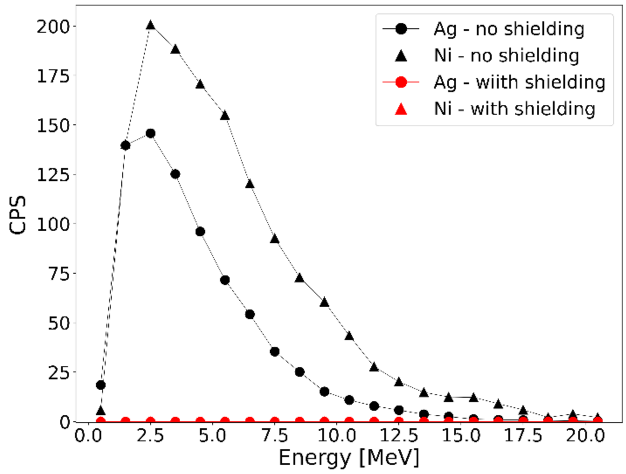

Figure 4.7 – Energy spectra of the neutrons produced in the fusion-evaporation reaction ^{16}O+^{107}Ag on the source position with (red) and without (black) a 40 cm PTE shielding. The energy spectra in black was obtained using the LILITA evaporation code.

4.3. Results

During the experiment all the events in each detector were acquired, without discrimination in energy and/or time. The maximum detection rate on the detector under study (CH1) was consistent with what expected (sec. 4.2) being 185 kHz for the reaction with Ag target and 310 kHz for the reaction with the Ni target.

In these cases, the ratio of the signal events (511 keV peak) with respect to the background was $\sim 10^{-2}$ for the reaction at 310 kHz with the Ni target and $\sim 2 \cdot 10^{-2}$ in the case of the reaction with the Ag target at 185 kHz.

The detection rate increased also on the triggering detector (CH0), reaching a maximum of 95 kHz and 90 kHz for the Ag and the Ni target respectively. An

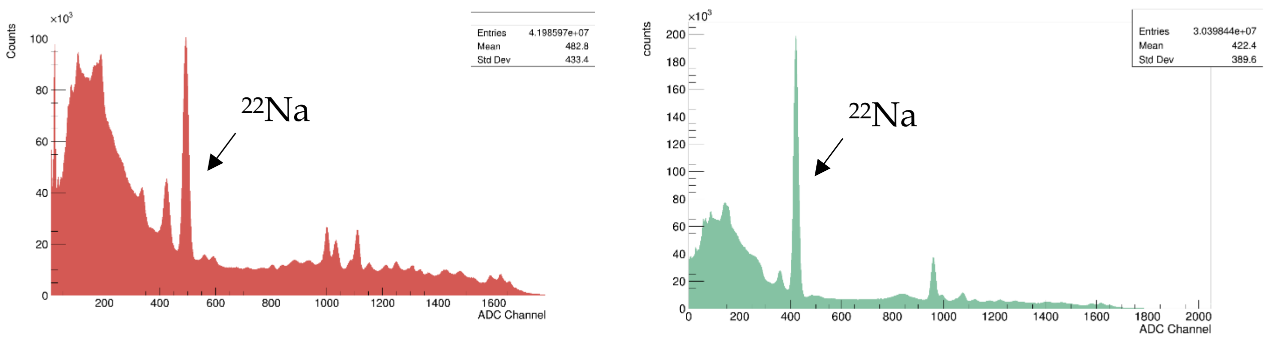

Figure 4.8 – Full energy spectra of detector under study CH1 (red) and triggering detector CH0 (green) for the reaction involving the silver target. The detection rate on CH1 is 45 kHz and on CH0 is 30 kHz. At this rate it is possible to distinguish the ^{22}Na peak in both spectra.

example of the energy spectra of CH0 and CH1 for the two reactions, detected together with the ^{22}Na source, are shown in Figure 4.8 and 4.9. It can be noticed that for both reactions there is a consistent contribution at low energies. Figure 4.8 shows the energy spectra of the detectors for the reaction involving the silver target. The total detection rate on CH1 was 45 kHz (30 kHz on CH0); at this rate it is possible to distinguish the ^{22}Na peak over the reaction background. The spectra of Figure 4.9 shows to the reaction with the Nickel target and with detection rate on CH1 of 230 kHz (65 kHz on CH0): at this rate the background overwhelms the ^{22}Na peak.

In the following sections it is shown the response of the detectors in terms of gain, energy resolution, coincidence efficiency (see chapter 3) and time resolution.

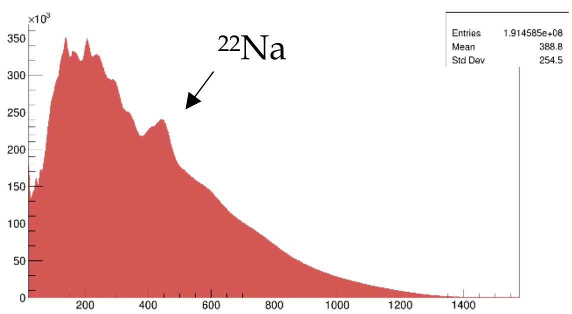

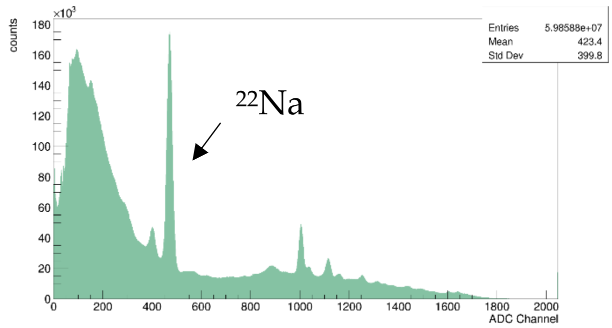

Figure 4.9 – Full energy spectra of detector under study CH1 (red) and triggering detector CH0 (green) for the reaction involving the nickel target. In the spectra shown in figure the detection rate on CH1 is 230 kHz and on CH0 is 65 kHz. At these rates, it is possible to distinguish the ^{22}Na peak only in the CH0 spectrum.

4.3.1. Gain and energy resolution

As shown in chapter 3, the gain of the detector is rate-dependent. Figure 4.10 shows the comparison of the CH1 spectra at 6 kHz (black) and at 80 kHz (red) in the case of the (^{16}O + ^{58}Ni) reaction. The shift of the 511 keV peak from the ^{22}Na source is clear. Both CH0 and CH1 show this effect and the gain variations are nearly independent from the type of background responsible for the detection rate, as shown in Figure 4.11. The gain variation of CH1 (red line) and CH0 (green line) at a given rate are essentially the same for both the reactions. These results are consistent with what was obtained at lower rates in the test with radioactive sources shown in Chapter 3.

The gain variations have a maximum at ~ 160 kHz; for rates above this value the energy resolution of the detector worsens reaching a value of 16% for 511 keV at 280 kHz, as it can be seen in Figure 4.12. As in the case of the gain variations, the results of the energy resolution are essentially independent from the origin of the background.

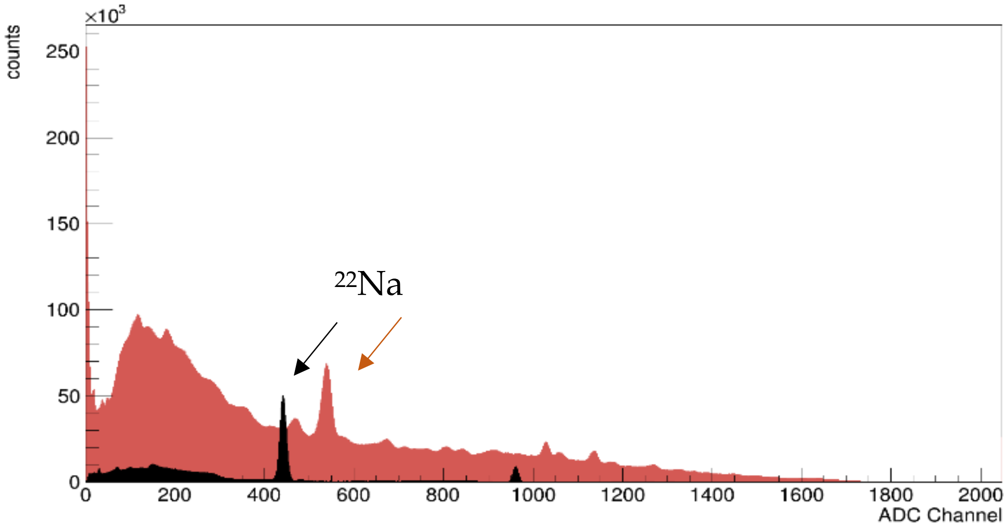

Figure 4.10 - CH1 full spectra for the reaction with the Ni target at 6 kHz (black) and 80 kHz (red).

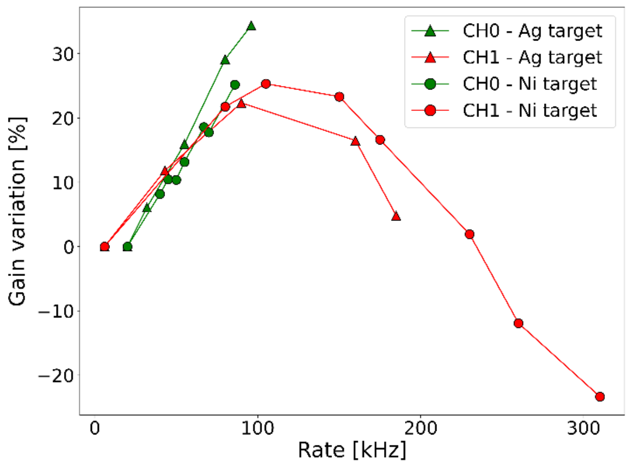

Figure 4.11 - Gain variation of the 511 keV peak at increasing detection rate, calculated for both reactions.

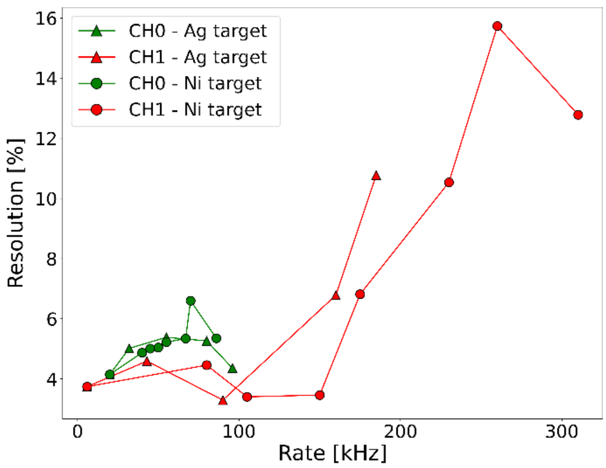

Figure 4.12 - Resolution of the two detectors at 511 keV as a function of the detection rate in both reactions. The resolution was calculated from the coincidence spectra.

4.3.2. Coincidence efficiency

The events from both detectors were analyzed with the same method showed in Chapter 3. A ROOT macro processes the events in coincidence in a time window

$\delta t_c = 30\ ns$. The coincidence spectra of CH0 vs CH1 are shown in Figure 4.13 and 4.14 for the Ag target and Ni target respectively.

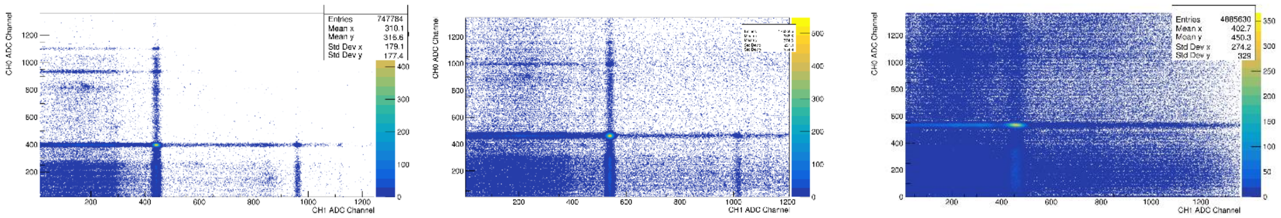

Figure 4.13 – From left to right: scatterplots of the coincidence spectra of CH0 and CH1 in the case of the Ag target for CH1 detection rates of 20, 90 and 190 kHz.

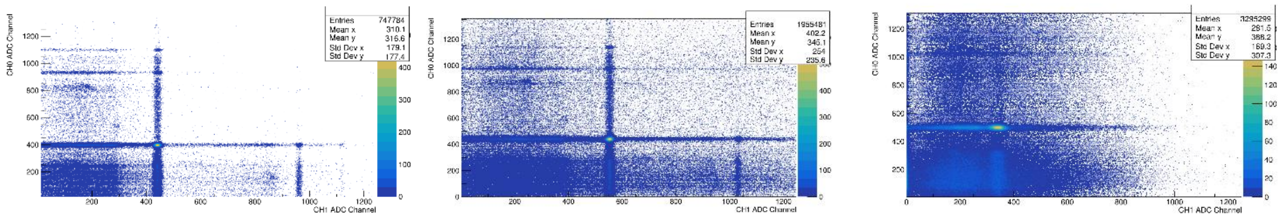

Figure 4.14 – From left to right: scatterplots of the coincidence spectra of CH0 and CH1 in the case of the Ni target for CH1 detection rates of 20, 105 and 310 kHz.

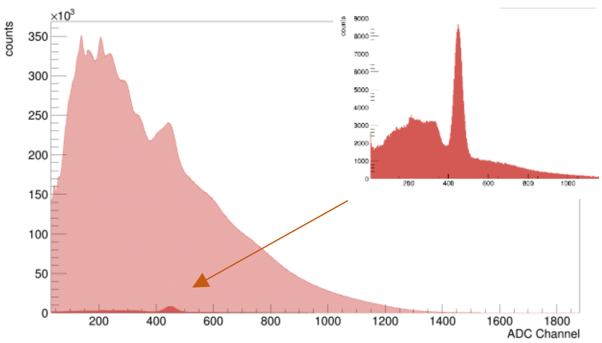

Figure 4.15 – CH1 coincidence spectra (red) and full spectra (shaded red) for the reaction with the Ni target at 230 kHz.

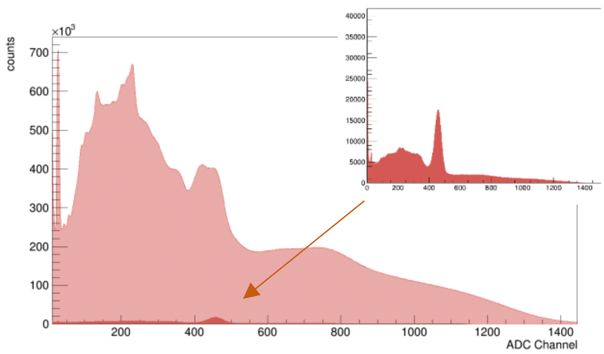

Figure 4.16 - CH1 coincidence spectra (red) and full spectra (shaded red) for the reaction with the Ag target at 190 kHz.

The coincidence spectra allow to distinguish the events of the 511 keV peak of CH1, even at high detection rate when the peak is not resolved. Figure 4.15 shows the full spectrum of CH1 in the case of the Ni target at 230 kHz (shaded red) and the CH1 coincidence spectrum (red). While the signal was not distinguishable in the full spectra, it is possible to identify it in the coincidence spectrum. Figure 4.15 shows a similar situation in the case of the reaction with the Ag target.

The coincidence events between the two 511 keV gamma are measured by performing a graphic cut around the 511-511 keV region in the scatterplot of Fig 4.13

and 4.14. The coincidence efficiency (eq 3.2) as a function of the rate for the two reactions is shown in Figure 4.17. The results are similar for both reactions but slightly lower in the case of the Ag target.

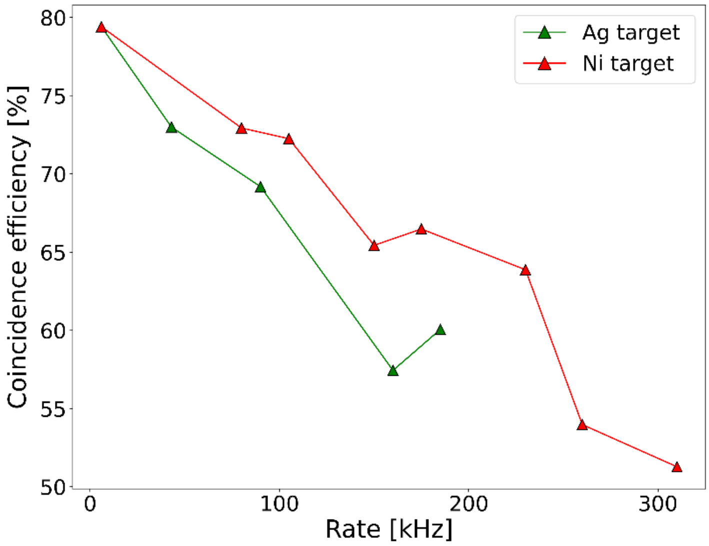

Figure 4.17 - Coincidence efficiency for the Ag target (green) and the Ni target (red).

4.3.3. Time resolution

The time spectra of the coincidence events were fitted with a Gaussian + (1st-order) polynomial function. An example of the time spectrum for the reaction with the Ni target at maximum CH1 detection rate is shown in Figure 4.18. The random coincidences are responsible for the constant background below the Gaussian peak and they increase with the detection rate. The P/B ratios at FWHM of the time spectra as a function of the rate for both reactions are shown in Figure 4.19. The sigma at the lowest detection rate is 1.3 ns; this value changes slightly with the rate under ~160 kHz but after this rate value, corresponding to the peak of the gain variation (meaning I_a~I_d – see sec. 3.5), the sigma increases rapidly, reaching 3.5 ns. Figure 4.20 shows the percentage variations of sigma as a function of the rate. The results are similar for both reactions.

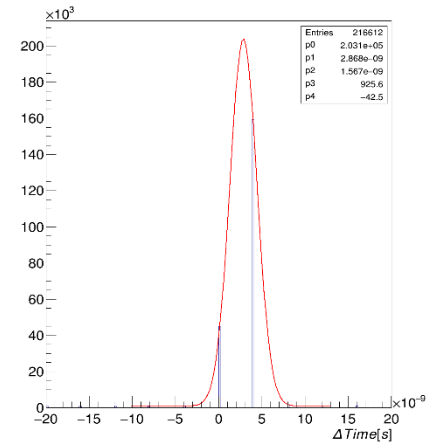

Figure 4.18 – Time spectra of the coincidence between the detectors in the case of the reaction with the Ni target at CH1 detection rates of 310 kHz.

The time resolution obtained in this experiment fits the requirements of NUMEN (below the rate threshold), however better time resolution can be obtained with the digitizer VX2745 foreseen for the experiment.

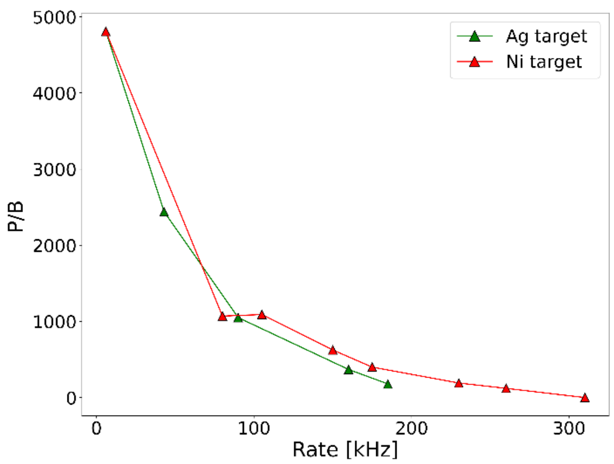

Figure 4.19 - P/B ratio at FWHM of the time coincidence spectra at increasing detection rate.

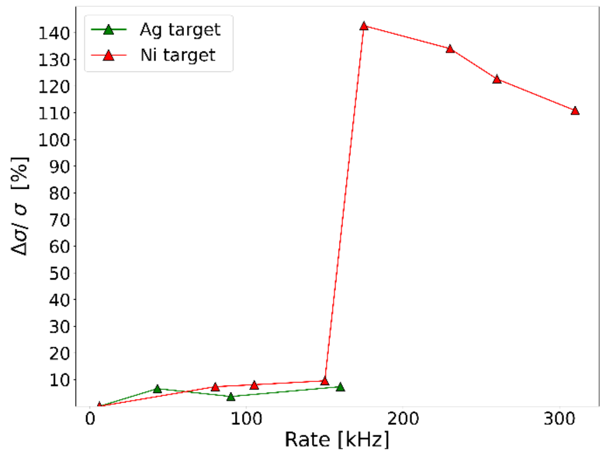

Figure 4.20 – Percentage variation of as a function of the rate for both reactions.

4.3.4. Preliminary test with VX2740

The experiment illustrated in this chapter was performed using the DT5720C digitizer, which is different from the one to be used for NUMEN (VX2745). As mentioned earlier, the reason for this choice is related to the fact that the model of the future NUMEN digitizers was not yet on the market and only few prototypes were available. In addition, at the time of this work, the prototypes were equipped only with the PHA firmware, while in NUMEN a PSD firmware will be used as it is more suitable for processing signals from scintillators such as $LaBr_3$:Ce.

Nevertheless, in order to test the performance of the detector with an acquisition system as similar as possible to the future ones, a preliminary test of the detector with a VX2740[1] digitizer was carried out during the experiment. For issues related to the acquisition software and the incompatibility with the VX2740 digitizer, it was possible to test the detector only at rates up to 140-150 kHz.

[1] The digitizer VX2740 is of the same family of VX2745 (the future NUMEN digitizer). The main difference is in the dynamic range which is limited to 2 Vpp for the VX2740 while it is 4 Vpp for the VX2740.

The discrimination capabilities of the detector were studied with the same procedure illustrated above, exploiting the reaction (^{16}O, ^{58}Ni). The acquired detection rates for CH1 were 15 kHz and 145 kHz, with both the DT5270C (+ PSD) digitizer and the VX2740 (+ PHA), with the detectors in the same experimental conditions. Figure 4.21 – left shows an example of the signal waveform acquired with the PHA firmware. The results for the coincidence efficiency are coherent between the two acquisition systems both at low and high detection rate. However, there is a discrepancy for both the energy and time resolution. At low detection rate, the configuration with the DT5720C shows better energy resolution (Res_{511keV} = 3.5 %) than the VX2740 (Res_{511keV} = 4.2%). At high detection rate the resolution increases in both configurations being still better for the DT5720C: 5.2% for the latter while 6.3% for the VX2740. This difference can be ascribed to the firmware used by the two digitizers: the signals of the LaBr3:Ce are too fast to be processes properly by the trapezoidal filter of the PHA firmware causing a worsening in the resolution. This confirms that the PSD firmware is the best choice for the acquisition system.

For what concerns the time resolution, at low detection rate the sigma of the Gaussian peak of the coincidence spectra is 1.3 ns for the configuration with the DT5720C and 450 ps with the VX2740 (Figure 4.21 – right). As expected, the time resolution is improved using the VX2740 digitizer, thanks to its timing performances. However, when increasing the rate up to 145 kHz, the time resolution increases by ~12% for the DT5720C and of ~55% for the VX2740. In both cases the time resolution is still

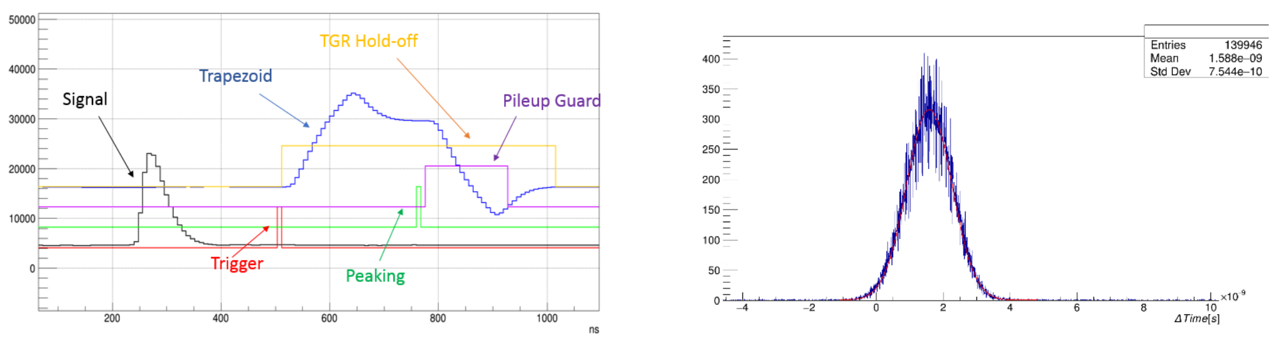

Figure 4.21 -On the left: Example of signal waveform acquired with the VX2740 digitizer and the PHA firmware. The trapezoidal filter is not processed properly due to the incompatibility with the signal fast rise time. On the right: Time spectrum of the coincidence events acquired with the VX2740 digitizer and the PHA firmware.

compatible with the NUMEN requirements. However, the change in resolution for the VX2740+PHA is very sharp and further studies are needed to investigate this effect.

4.4. Discussion of HIT results

In this chapter it is presented the study of the detector response under high intensity rates of both gamma and neutrons, in conditions of detection rates similar to the NUMEN experiment. This study shows that it is possible to distinguish a given event with a signal-to-noise ratio of $\sim 10^{-2}$ with good energy resolution.
It was demonstrated that the performances of the detector are strongly affected by the detection rate both in terms of energy and time response.

Energy response

The gain of the detector (evaluated at 511 keV) increases with the detection rate up to 20-30% of the initial value and it shows an abrupt change around 160 kHz, in agreement with what was shown in the characterization presented in chapter 3. The energy resolution is affected by the rate, as it worsens with increasing detection rate and it shows a sharp change also around 160 kHz. At detection rates below 160 kHz the resolution at 511 keV has a maximum of ~6%; after 160 kHz it reaches 15-16%. While 6% at 511 keV is a value still in the acceptance range for G-NUMEN, values of 15-16% are well above the range.
The above-mentioned effect mainly depends on the detector electronics (PMT+voltage divider). This means that in order to satisfy the requirements for G-NUMEN, an effort must be made in the search of the best electronic configuration (see sec. 4.5).

Regardless from the effects above 160 kHz, the dependence of the gain on the detection rate suggests that for the future experiments it will be necessary to perform accurate and recurring calibrations in the same conditions of the experiment in order to be able to properly distinguish the energy peak.

Time response

The time resolution is affected by the detection rate and it also shows an abrupt change around 160 kHz. At detection rates below this value, the resolution changes slightly and it remains below 1.5 ns. For higher detection rates the resolution increases up to 3 ns. While this value may still be acceptable for NUMEN requirements, it suggests that events are not being processed correctly causing an increase in random background compared to true coincidences. Preliminary tests with the VX2740 digitizer show better time resolution, but more studies are needed in this direction.

Based on the results shown in this work, further investigations aimed at finding the optimal electronics configuration for the optimization of both the temporal and energy resolution are needed.

4.5. Effects of the electronics on the detector response

In this work it is shown that the detector characteristics are affected by the detection rate and/or the amplitude of the signal (non-linearity with energy). The variations of the energy response of the detector with the increase in detection rate are mainly related to the type of power supply of the detector and in particular to the stability of the last inter-stage voltages.

In the next sections a comparative study of two LaBr3:Ce detector response at high detection rate (i.e. high anode current) is presented, respectively with a passive and an active voltage divider.

For a passive voltage divider, such as the one used for the detector prototype, the gain variations depend on the anode and divider currents as the follows:

$$\frac{\Delta G}{G} \approx \frac{\alpha N}{N+1}\frac{I_a}{I_d} \tag{4.2}$$

where α is related to the gain variation, N is the dynode number, I_a and I_d are the currents of the anode and the divider [35]. The currents ratio is usually $I_a/I_d < 100$ in order to avoid any gain change related to small variation of the anode current. However, the anode current can increase significantly due to high rate and/or high amplitude signals. This will induce an effect similar to the increase of the power supply, causing an increase of the detector gain as in the eq. 4.2. If the anode current reaches the critical value $I_a \sim I_d$, the voltage drops in the last stage can no longer be

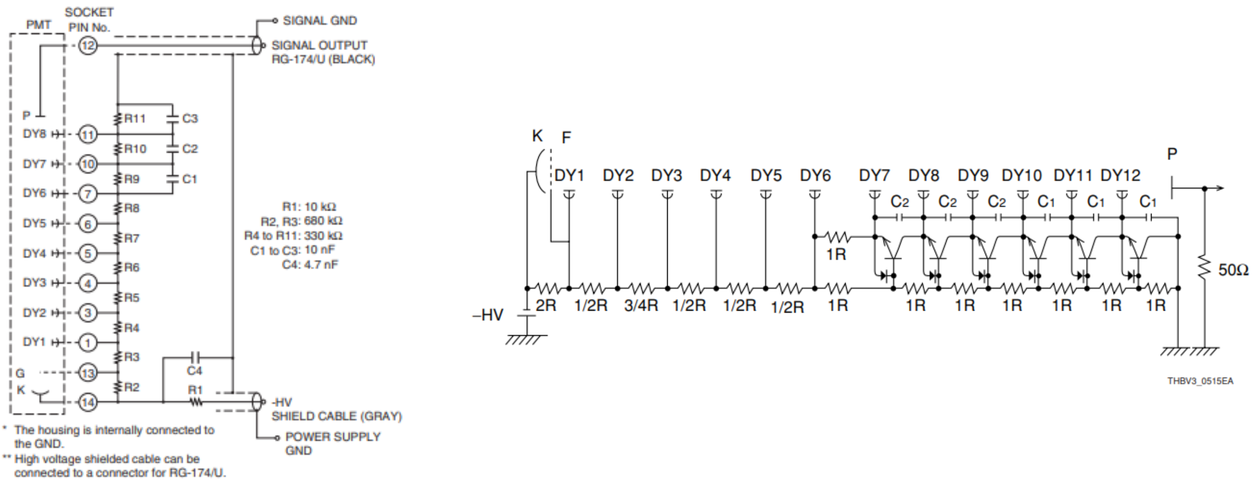

Figure 4.22 - Scheme of a passive (left) and active (right) voltage divider.

supported and, as a result, the gain suddenly drops. These effects can be mitigated using an active (transistorized) voltage divider which reduces the variation of the anode current by limiting it to half of the divider current and keeping the voltage drop on the last stages constant, even at high count rate. Figure 4.22 shows the design of a passive and an active voltage divider (base).

The passive detector used for this study is the prototype illustrated so far (PMT R6231 + E1198-26), while the active base one is a detector produced by EPIC which is made by the same crystal of the prototype, a PMT with the same characteristics of the R6231 and an active voltage divider. To simplify, in the next sections the passive-base detector will be referred to as the prototype and the second detector will be referred to as the active-base one. This study was carried out using the digitizer VX2745 with the PSD firmware.

4.5.1. Detection rate limits

The signal waveforms of the passive- and active- base detectors have the same characteristic time, and the active-base detector shows similar performances to the passive detector at low detection rate. The resolution at 662 keV is 2.8%, slightly better than the one for the passive detector (3.2%). The efficiency of the active base

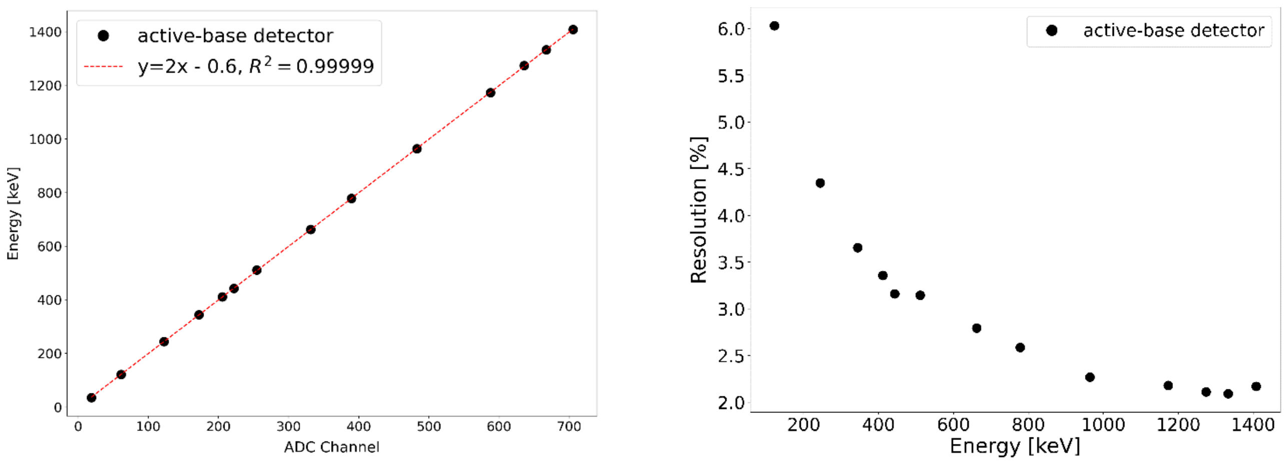

Figure 4.23 - Calibration (left) and energy resolution (right) for the active-base detector. The detection rate for the spectra of the calibration source is < 3 kHz.

detector at 662 keV is 26.5%, in good agreement with the value measured for the passive detector.

The response of the detectors at increasing detection rate was studied by varying the distance source-detector and/or by adding intense sources near the detectors.

Figure 4.24 – left shows the gain variation at 662 keV of the active detector as a function of the detection rate, where the latter was increased only by varying the relative position source-detector (see Fig. 4.24 - right).

The active-base detector shows an abrupt change in gain at detection rate ~ 130 kHz. As mentioned before, the effect of the detection rate on the detector is related to the anode current which causes the gain variations. Therefore, for a comparative study it is more accurate to evaluate the detector dependence on a parameter directly related to the current rather than on the detection rate. The product of the detection rate and the average energy of the gamma rays gives a parameter proportional to the anode current.

Figure 4.25 shows the comparison of the gain variation at 662 keV for both the active and the passive detector as a function of the current. It must be specified that the maximum detection rate for the two detectors is the same (~160 kHz), but since the gain of the passive detector is higher, the current relative to the same detection rate is also higher. As expected from literature, the gain shows an increase with the

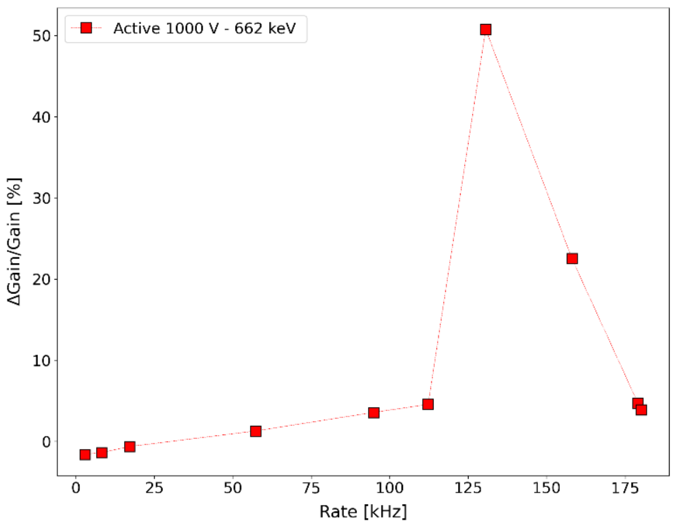

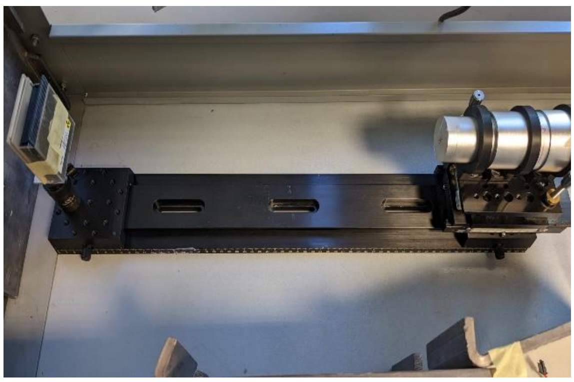

Figure 4.24- On the left: gain variation for the 662 keV peak of ^{137}Cs calibration source as a function of the detection rate. On the right: picture of the experimental setup.

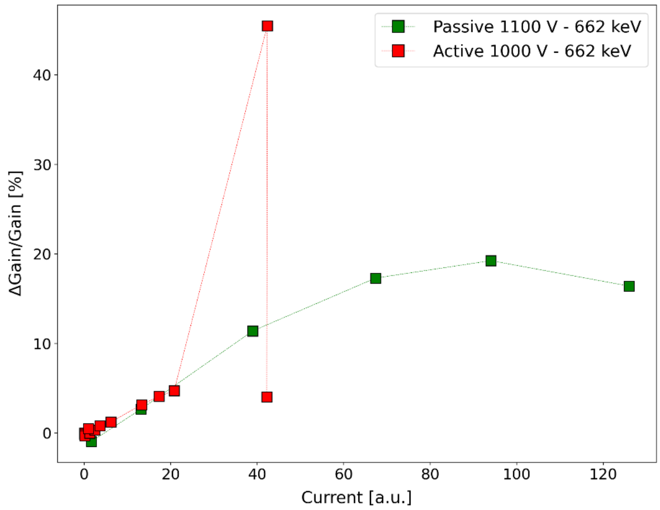

Figure 4.25 - Comparison of the current dependence for the active base detector (red) and the passive base one (green). The last point for both the active and the passive base detector corresponds to a rate of 160 kHz.

current and then a decrease when the anode current reaches the critical value. The passive base detector shows a smoother gain variation with respect to the active base detector. The latter shows a sharp peak at 40 current equivalent (corresponding to 160 kHz) and above this current value, the energy spectrum has a random distribution and the energy peak can no longer be identified. As for the passive base detector, the current peak is around 90 current equivalent, which corresponds to 120 kHz and above this peak the gain decreases but the structure of the energy spectrum is preserved and the data acquisition is still possible.

Figure 4.26 shows the current dependence of the gain variation for the detectors at different HV. For each data point set, the highest current equivalent corresponds to

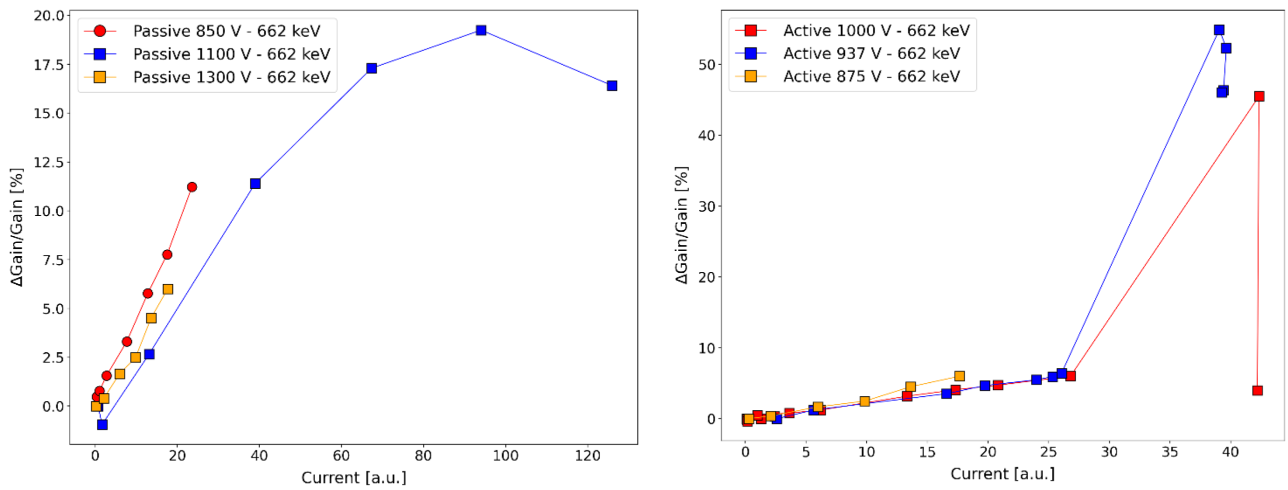

Figure 4.26 - Gain variation of passive base (left) and active base (right) at different power supply.

the same maximum detection rate of 160 kHz. Decreasing the power supply reduces the detector gain, and therefore increases the detection rate limit for the active base detector. At HV = 875 V it is possible to avoid the gain drop, reaching the same detection rate of higher power supply. Since the energy resolution of the detector does not change significantly for HV ≥ 800 V (Figure 4.27), decreasing the power supply voltage can represent a good choice to avoid 'breakdown' effect of the active base detector.

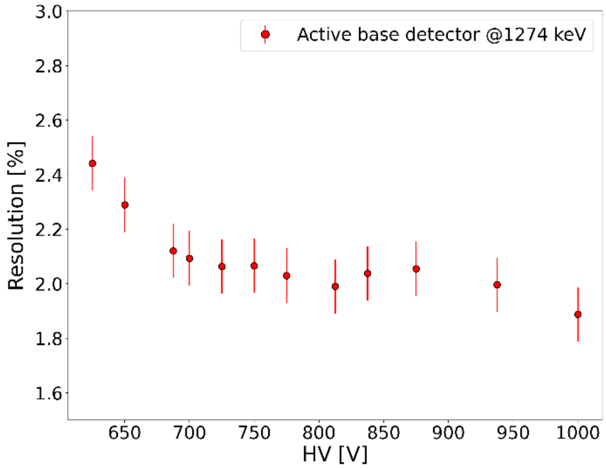

Figure 4.27 - Dependence of the resolution on the power supply for the active base detector for the energy of 1274 keV (22Na).

4.5.2. Linearity of the detector response

The response of the detectors at increasing anode current depends also on the energy in a non-linear way. Figure 4.28 shows the gain variation of the peaks at 662 keV and 1472 keV at increasing current equivalent, for both the passive and the active detector. For both detectors the gain variations are higher for higher energy peaks different but the difference in variation is smaller for the active base detector. This is due to the effects of the transistors (instead of the resistors for the passive base) which increases the linearity of the response. Figure 4.29 shows the comparison of the gain variation of the two detectors at lower power

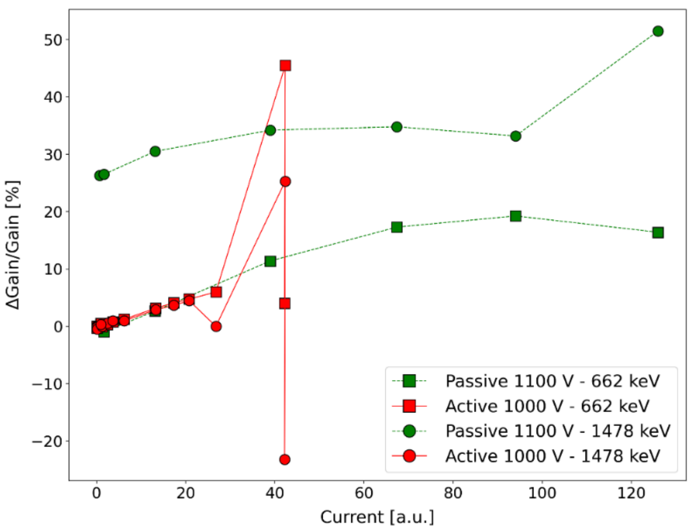

Figure 4.28 - Response of the detectors as a function of the current equivalent at different energies. The green dots represent the passive base detector, the active base detector is represented by the red dots.

supply voltage for the energy peak of 662 keV, 1478 keV and for the last energy peak of the alpha contamination at 2.6 MeV equivalent. There is a clear difference in the gain variation for the passive base detector between the first two energy peak and the one at 2.6 MeV, while the gain variations at different energies for the active base detector are similar to each others.

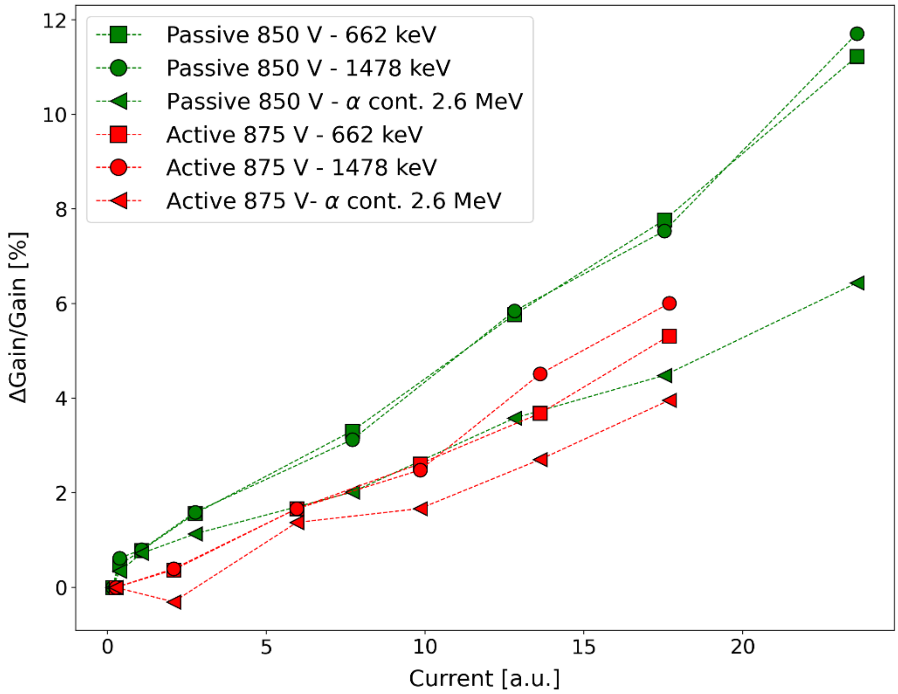

Figure 4.29 - Comparison of gain variation for the passive- and active- base detectors at different energies.

4.5.3. Discussion

The dependence on the detection rate (i.e. the anode current) of the passive- and active base detectors was studied up to a detection rate of ~160 kHz. The gain variations for both detectors are in agreement with the theoretical behavior.

When reaching a detection rate of ~160 kHz (40 current equivalent), the active base detector showed an abrupt change in gain variation: it was not possible to acquire consistent data at higher detection rate. This effect was limited by decreasing the power supply voltage, with a negligible decrease in energy resolution. The passive base detector showed a smoother change in gain variation at increasing detection rate, with a peak for ΔG/G at 120 kHz (for HV = -1110 V). After this value, it was still

possible to acquire data with no substantial energy distortion and/or loss up to the maximum rate tested (160 kHz). With the passive base detector it was possible to analyze consistent signal up to 160 kHz without having to reduce the power supply voltage and therefore worsen the energy resolution. However, the active base detector showed a more linear response with respect to the passive base detector. Further studies are needed to assess the best configuration for the final detector of the G-NUMEN array.
The active base detector appears to be the best choice for the linearity of its response when working at low voltages, but its gain variation with the detection rate must be tested at higher rates, more similar to the ones at the foreseen experimental conditions (~300 kHz), to exclude the possibility of 'breakdown' also at lower power supply voltage.

5. HIT: Radiation Damage Study

This chapter discusses the radiation damage study of the detector prototype of the gamma array for the NUMEN experiment. After an introduction on the motivations and on the state-of-the-art of the $LaBr_3$:Ce radiation damage studies (sec. 5.1), the experiment HIT will be introduced. This experiment was performed in 2022 at the ALTO facility (IJC Laboratory), with the purpose of studying the detector response to high fluence of fast neutrons (sec. 5.2). The section 5.3 presents the results of this study while the conclusions and future perspective will be discussed in section 5.4.

5.1. Motivations

The gamma array will play an important role for all the reactions in which an intense rate is expected (see Chapter 1). The target area around which the G-NUMEN array will be bombarded by an intense flux of both neutrons and gammas whose high rate can degrade the performances of the detectors: a radiation damage study is necessary to assess the response of the detectors to such harsh environments and evaluate their possible limits. Figure 5.1 shows the simulated spectra of both gammas and neutrons for selected angular slices of the array, for one of the reactions under study for the NUMEN experiment. In this situation, the maximum integrated flux in the detector

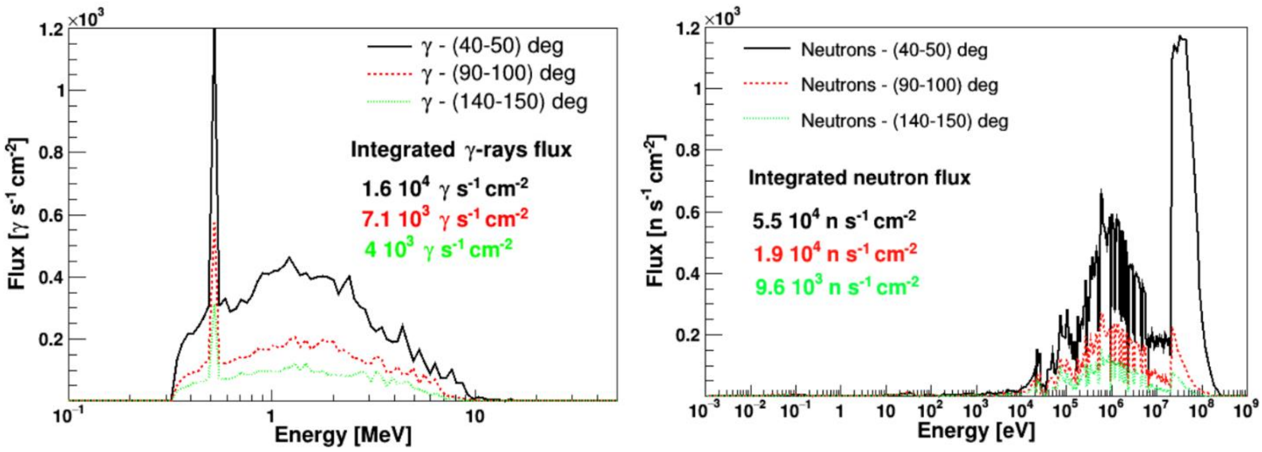

Figure 5.1 - FLUKA simulation of the gamma (left) and neutron (right) flux and energy in the array region for some angular slices of the array. The results refer to the reaction ^{18}O @ 60 AMeV on Sn 500 nm thick target with a beam flux of 10^{12} pps [O. Sgouros].

region is $\phi_{\gamma}^{max} = 1.6 \cdot 10^4\, \gamma/(s \cdot cm^2)$ for gammas and $\phi_{n}^{max} = 5.5 \cdot 10^4\, n/(s \cdot cm^2)$ for neutrons. The expected duration for a NUMEN experiment will be of around 30 days (corresponding to a 10% precision on the DCE cross section) [6], leading to a fluence $\Phi \sim 10^{11}\, evt/cm^2$ of both gamma and neutron for the above-mentioned reaction.

For other reactions under study for NUMEN, at different energies, the simulations show similar results for the integrated flux of neutrons while the gamma fluxes can be even higher. While the gammas are not expected to produce permanent damage in the detectors [43], [44] recent studies [45], [46], [47] have shown that the LaBr3:Ce performance can deteriorate after exposure to intense neutron fluxes. However, there are very few data in literature regarding the neutron damage of $LaBr_3$:Ce detectors. Moreover, the maximum neutron fluence investigated is 2-3 order of magnitude lower than that expected for the NUMEN experiment. In addition, there is no detailed study of the damage as a function of the neutron fluence and no quantitative information about the recovery time. Lu et al. [45] have shown that both the light output and the resolution at 661.6 keV of the $LaBr_3$ can worsen after neutron exposure. However, the dependence of the damage on the neutron fluence/flux and energy is not clear: higher neutron fluence can result in less damage than lower neutron fluence. In particular, fast neutrons from D-T reactions cause a resolution increase of 42% after $10^7\, n/cm^2$. Thermal neutrons produced in a reactor induce a resolution increase of 18% at higher neutron fluence ($10^8\, n/cm^2$) while neutrons from an Am-Be source (thermal + fast) cause no observable effect in the crystal resolution after a fluence of $10^8\, n/cm^2$ [45]. In general, the radiation damage of the $LaBr_3$:Ce crystal might have a dependence on the neutron energy, flux and fluence and these relations are not well understood.

For what concerns the NUMEN needs, the contribution for the neutron background is given mainly by fast neutrons (see Figure 5.1) with a the maximum expected fluence of $\Phi_{n}^{max} = 10^{11} - 10^{12}\, n/cm^2$, which is 3-4 order of magnitude higher than the maximum neutron fluence for which the damage has been investigated in literature.

The part of the HIT experiment presented in this chapter regards the study of the effect of the neutron damage on the $LaBr_3$:Ce detector, exposed to a fast neutron fluence of $\Phi_n \sim 10^{10}\ n/cm^2$. The post-irradiation annealing has also been evaluated. The following section presents the method used for the radiation damage study: section 5.2.1 presents the details of the neutron beam, the neutron monitoring is discussed in section 5.2.2 while the procedure for the neutron irradiation is illustrated in section 5.2.3. The results of this work and the discussion are presented in section 5.3 and 5.4.

5.2. The experiment

One of the aims of the HIT experiment was to evaluate the radiation damage induced by high fluence of fast neutrons on a $LaBr_3$:Ce detector. The experiment was performed with the Tandem accelerator of the ALTO facility (IJC Laboratory) using the LICORNE source which provides a fast neutron flux exploiting the reaction ^{7}Li (p,n)^{7}Be in inverse kinematics (see sec. 5.2.1).

The characteristics of a $LaBr_3$:Ce detector (38 mm diameter and 50 mm length) were studied before, during and after the exposure to a neutron fluence. In particular, the characteristics evaluated were: the intrinsic background, the time resolution, the gain and the energy resolution. The irradiation of the detector was divided in several steps. After each step the energy resolution and the gain at 661.6 keV were measured using a ^{137}Cs source. The intrinsic background and the time resolution were measured only before and after the irradiation. The recovery of the detector properties was also studied for a period of 41 days after the irradiation (see sec. 5.3.2)

The neutron fluence on the detector was monitored using two techniques: 1) the measurement of the ^{7}Be activity produced during the reaction and 2) the use of an activation foil of natural Indium. The ^{7}Li beam flux and thus the production of neutrons during the irradiation was also monitored by measuring the CPS of the ^{7}Li Coulomb excitation peak (see sec.5.2.2).

5.2.1 The LICORNE source

LICORNE is a neutron source installed at the ALTO facility which uses the reaction ^{7}Li (p,n)^{7}Be in inverse kinematics to produce naturally forward collimated neutron beam (max opening cone < 27°) with an energy ranging from 500 keV to 4 MeV [48], [49]. The unique characteristics of the LICORNE source such us the beam directionality, the possibility to produce quasi-mono-energetic neutron beam, the low fast and thermal scattered neutron background and the high neutron flux available (up to 10^{8} n/(s·sr)) allow this source to be used in several fields: from the study of the fission fragments to geochronology and medical physics applications [50], [51], [52], [53]. The hydrogen target is gaseous, and it is contained in an aluminum cell at the end of the setup, separated from the vacuum beam line by a Ta window (see Figure 5.2). The LICORNE properties such as the cell dimensions and the hydrogen pressure can be adjusted according to the experimental needs as their values affect the neutron energy distribution, as well as the maximum possible flux. Longer cells at high pressure result in a broader energy spectrum since the ^{7}Li can slow down up to the threshold energy (E_{th} = 13.098 MeV). The higher hydrogen

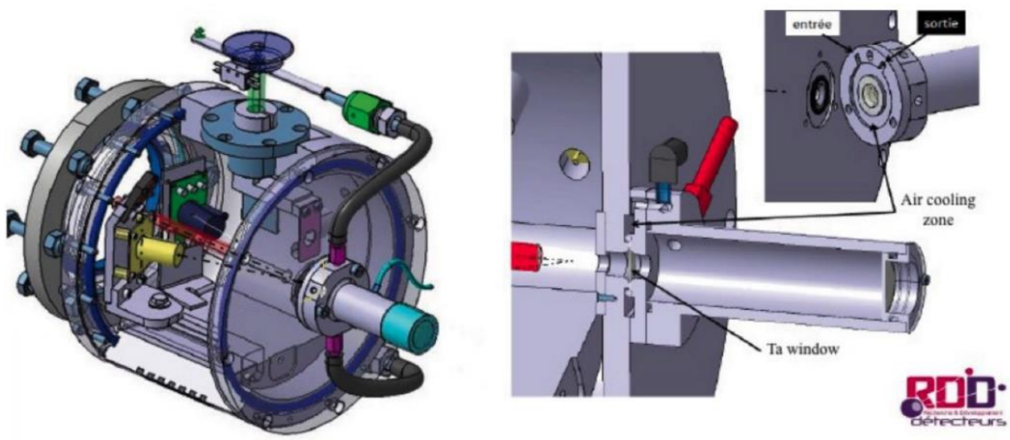

Figure 5.2 – Technical drawing of the LICORNE source. An aluminum cell contains a camera and an illuminating LED for beam tuning. The hydrogen cell is separated from the previous cell by a Ta window [48].

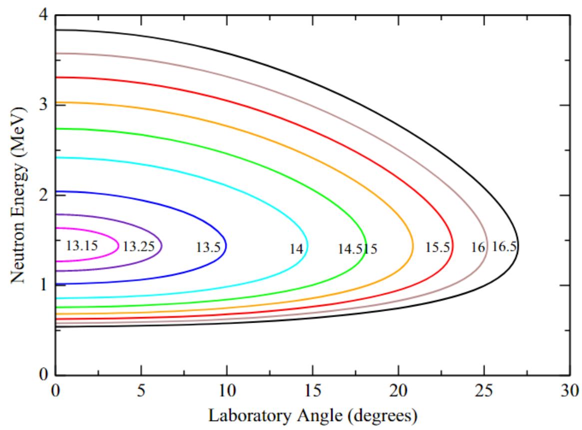

Figure 5.3 - Calculated kinematics curves for the neutron energy for different emission angles, depending on the ^{7}Li beam energy [48].

pressure, the higher the neutron flux. The ^{7}Li energy at the cell entrance affects the energy, the flux and the cone angle of the emitted neutrons. Figure 5.3 shows how the neutron energy varies

with the laboratory angle and the relation of these quantities with the beam energy. Neutrons with broad energy spectrum are emitted with higher cone angle, at higher ^{7}Li beam energies while, for energies just above the threshold, it is possible to obtain very well-defined energy spectra confined in a very narrow cone (< 3°). The LICORNE characteristics and the ^{7}Li beam properties used for the experiment presented in this chapter are listed in Table 5.1.

In these conditions, the simulated spatial distribution of the neutron cone at the exit of the hydrogen cell is shown in Figure 5.4 – left. The flux is more intense in the central region of the cone and it decreases at increasing angles. The maximum cone angle of the neutron beam is θ = 21.4° which corresponds to a cone section of diameter d = 3.1 cm at a distance z_0 = 0.5 cm from the hydrogen cell, corresponding to the position at which the detector under study was placed (see sec.5.2.3). The calculated total neutron flux at different cell pressures are shown in Figure 5.4 – right, assuming a beam intensity of 100 nA and a 100% transmission in the beam line. The expected total neutron flux in the cone is ~ 1.5 10^7 n/s at P = 1.1 bar and ~ 1.7 10^7 n/s at P = 1.3 bar.

^{7}Li beam	Incident energy	16.5 MeV
LICORNE	Ta window thickness	2 µm
	H_2 cell pressure	1.1 – 1.3 bar
	H_2 cell length	3.5 cm

Table 5.1 - Experimental parameters used for the radiation damage study presented in this chapter.

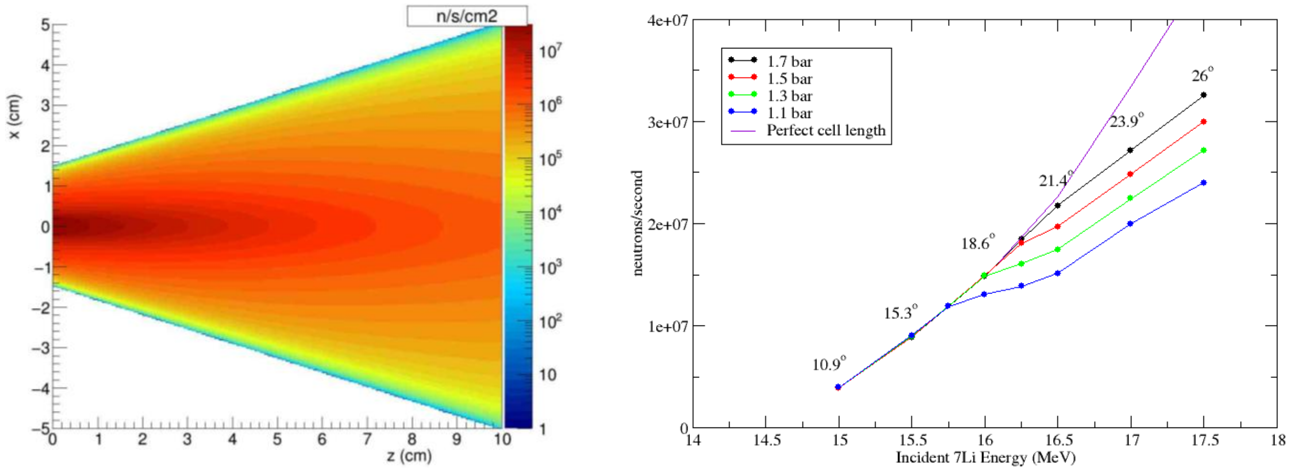

Figure 5.4 – On the left: simulated spatial distribution of the neutron beam cone for the experimental condition of this work (for I = 100 nA) . On the right: calculated neutron flux as a function of the incident ^{7}Li energy, at different hydrogen cell pressure, assuming 100% transmission in the beamline (I = 100 nA) [private communication from J.N. Wilson].

5.2.2 Neutron monitoring techniques

For a complete analysis of radiation damage results and their proper connection with the total neutron fluence, three independent methods for the monitoring of both the neutron fluence and the neutron flux variations were developed. The neutron fluence was evaluated by measuring the ^{7}Be nuclei produced in the ^{7}Li (p,n)^{7}Be, and by measuring the activity of a ^{nat}In activation foil. The neutron flux variations were monitored during the irradiation by measuring the coulomb excitation peak of ^{7}Li beam induced by the beam itself.

^{7}Be activity

In the reaction ^{7}Li (p,n)^{7}Be used in the LICORNE source, the number of neutrons produced is equal to the number of ^{7}Be nuclei; the latter are produced inside the hydrogen cell and all of them are implanted at the bottom of it[2]. The ^{7}Be decays leaving ^{7}Li in an excited state [54], by measuring the activity of the beryllium is possible to calculate the number of neutrons produced. Figure 5.5 shows the

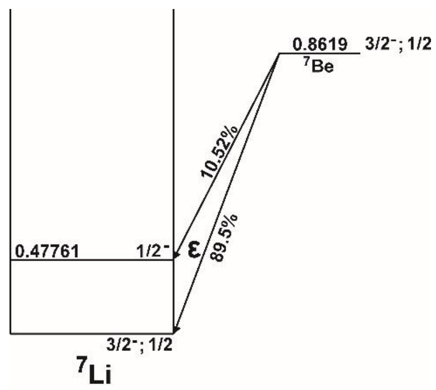

Figure 5.5 - Decay scheme of 7Be [TUNL – Nuclear Data] .

[2] The thickness of the end of the hydrogen cell (t = 5 mm) is greater than the range of the ^{7}Be nuclei produced in the reaction (range = 0.6 mm for the maximum ^{7}Be energy E_{7Be} ~ 15 MeV)

decay scheme of the ^{7}Be: the half-life of the nuclei is $t_{1/2} = 53.12\ d$ and it decays emitting a gamma $E_{^7Be} = 477.6\ keV$ with a branching ratio br = 10.52% [55].

$$\#n = \#\ ^7Be = \frac{A(t*)}{\lambda_{^7Be}} = \frac{\#counts(477.6\ keV)}{t_{meas} \cdot \varepsilon \cdot br \cdot \lambda_{^7Be}} \tag{5.1}$$

The equation (5.1) shows the relation between the number of neutrons produced and the activity of the 7Be nuclei where: A is the activity of the ^{7}Be nuclei implanted in the cell at the time t*, $\lambda_{^7Be}$ is the decay constant, ε is the geometric and energetic efficiency of the detector and $\#counts$ are the counts in the 477.6 keV peak measured in the time t_{meas}.

The activity of ^{7}Be nuclei was measured at the end of each irradiation steps when the beam was off. The detector used for the measurement was a $LaBr_3$:Ce (ϕ = 38 mm x 50 mm) coupled with a PMT R6231 and a E1198-26 voltage divider. It was placed at the exit of the hydrogen cell, in a central position with respect to the beam axis and at a distance $d = 5\ mm$. The signal was processed with a 671 amplifier and an Multi Channel Analyzer, and then acquired with the software Maestro from Ortec.

Activation foil

Natural Indium foils can be used as activation detectors for neutrons due to their high neutron capture cross section [56]. Natural indium is composed by 95.7% of ^{115}In and 4.3% of ^{113}In; for both isotopes, thermal and fast neutrons can activate different reaction channels but the ones of interest for the monitoring of fast neutrons produced with the LICORNE source are listed in Table 5.2. In fact, the energy range of the neutron produced with LICORNE is $\sim 500\ keV - 4\ MeV$ and the cross section of the reaction listed in Table 5.2 have a low energy threshold at $\sim 500\ keV$ (see

	Abd [%]	Half-life [h]	Energy [keV] (br)	xsec @ 1.5 MeV
^{115}In(n,n')^{115m}In	95.7	4.49	336 (0.458)	180 mb
^{113}In(n,n')^{113m}In	4.3	1.66	392 (0.654)	260 mb

Table 5.2 - Reaction of interest for fast neutron monitoring of LICORNE source using a ^{nat}In foil.

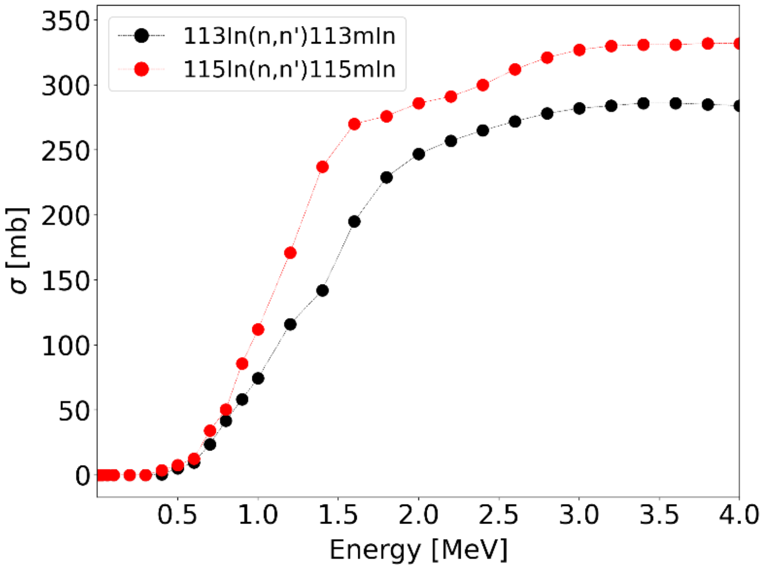

Figure 5.6 - Cross section of the ^{115}In(n,n') ^{115m}In reaction as a function of the incident neutron energy. The cross section is negligible for neutron energies below 500 keV [TENDL-2021].

Figure 5.6). This means that the low energy neutron background does not contribute to the activation of the channels listed in the table which is due only by the neutron produced by LICORNE. All the other possible reaction channels not listed in the table can be activated by both thermal and fast neutrons.

The cross sections of the reactions for $E_n = 1.5\ MeV$, corresponding to the energy peak of LICORNE (see sec.5.2.1), are listed in Table 5.2. The reaction involving ^{115}In has a lower cross section than that involving ^{113}In, however the latter isotope is less abundant. For this reason the reference reaction that chosen for the monitoring of the LICORNE neutron fluence was ^{115}In(n,n')^{115m}In which emits a gamma at $E_\gamma = 336\ keV$ with a half-life of $t_{1/2} = 4.49\ h$ and a branching ratio of br = 0.458.

This energy peak can be obtained also through photon activation by the competing reaction ^{115}In(γ,γ')^{115m}In. However, the cross section for photon activation is several order of magnitude lower than for neutron activation ($\sigma_{(\gamma,\gamma')}$ ~10^{-5} mb - 10^{-2} mb) [TENDL-2021] and also the simulated gamma flux in the position of the In foil is lower than the neutron flux. For these reasons, the contribution of photon activation to the energy peak $E_\gamma = 336\ keV$ can be neglected and it can be assumed that this peak is activated only by neutrons from LICORNE.

During the irradiation, a ^{nat}In foil was placed at the exit of the hydrogen cell with a cylindrical support which allowed the foil to be centered with respect to the beam axis and adherent to the beam exit. For each irradiation step monitored with this technique, different foils were used. The activity was measured with an N-type High Purity Germanium HPGe detector (Figure 5.7).

Figure 5.7 - HPGe detector used for the measurement of the activity of the Indium foil. The detector was shielded from the natural gamma background with lead layers.

The foils activities were measured at t^* from the irradiation at increasing time period from the end of the irradiation to reconstruct the decay curve and calculate the activity at the time t_0 corresponding to the irradiation stop (see sec. 5.3.1). The neutron fluence for one irradiation step can be calculated from the activity of the Indium foil at t_0, taking into account the dimensions of the foil (hence the number of ^{115}In nuclei), the cross section of the reaction of interest $\sigma_{(n,n')}$, the decay time $\tau = (t_{1/2}/ln2)$ and the duration of the irradiation:

$$\#n = \frac{A_0(t \quad = 0)}{\sigma_{(n,n')} \cdot \tau \cdot \#^{115}In} \tag{5.2}$$

where the cross section is evaluated at the energy corresponding to the peak of the energy distribution of the neutrons emitted by LICORNE: $\sigma(E_n = 1.5\ MeV) = 180$ mb. The activity $A_0(t \quad = 0)$ is extrapolated from the exponential fit of decay curve where the activities at time t* are calculated as:

$$A(t\,*) = \frac{\#counts}{t_{meas} \cdot \varepsilon \cdot abd \cdot br} \tag{5.3}$$

where ε is the efficiency of the HPGe detector $\varepsilon = \varepsilon(336\ keV) \cdot \varepsilon_{geom}$ and $\#counts$ are the events in the 336 keV peak measured in t_{meas}.

^{7}Li Coulomb excitation

The LICORNE source uses a ^{7}Li primary beam for the neutron production. As a consequence, it is possible to measure the Coulomb excitation of the first excited state of ^{7}Li at $E_{7Li} = 478\ keV$ whilst the beam is impinging on the hydrogen target and producing neutrons [57], [58]. The Coulomb excitation of the primary beam 7Li(p,p'γ) can be used to monitor the primary beam itself since the rate of events in the 478 keV peak is proportional to the intensity of the beam itself.

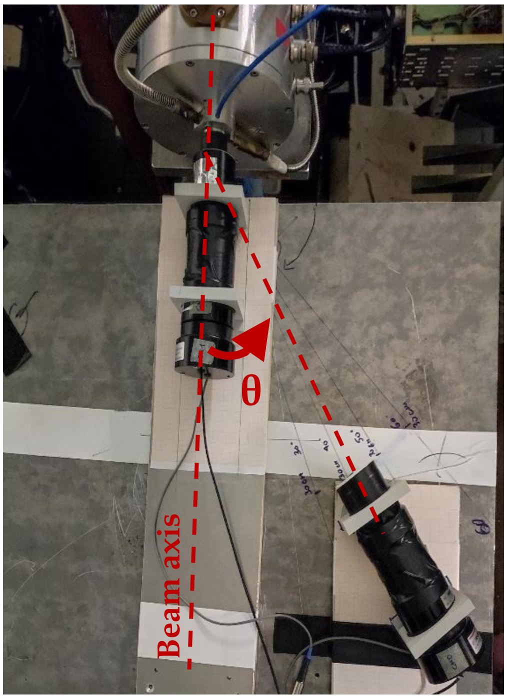

Figure 5.8 - Experimental set up for the monitoring of the ^{7}Li coulomb excitation peak . The monitoring detector is placed at θ = 40° respect to the beam axis while the detector under study is placed along the axis at the exit of LICORNE.

In fact, it is possible that during the irradiation the beam changes both in intensity and in position, causing a variation of the neutron flux produced. In both cases the Coulomb excitation of the primary beam changes due to the change in the interaction of the beam with the target. Monitoring the Coulomb excitation (CoulEx) peak allows to monitor the neutron production during the irradiation and to promptly adjust the beam parameter if any changes occur. Figure 5.8 shows the setup for the monitoring of the CoulEx peak during the irradiation. The detector under study for the neutron irradiation damage is placed along the beam axis while a second detector is placed at 40 degrees respect to the beam axis and it is used for the monitoring of the CoulEx peak. Since the neutrons from LICORNE are produced in a well-defined cone angle of 21.4° (see sec.5.2.1) the detector is not exposed to neutrons produced in the reaction. Due to the angular position, the energy of the CoulEx peak is Doppler shifted so the peak is measured at ~461 keV. During the irradiation the counts per second in the above-mentioned peak were monitored, in order to check for any unwanted variation of the beam intensity and hence of the neutron flux.

The monitoring detector is a $LaBr_3$:Ce (ϕ = 38 mm x 50 mm) coupled with a PMT R6231 and a E1198-26 voltage divider. The signal is amplified (671 Ortec) and read with a MCA connected to the Maestro software.

5.2.3 Neutron irradiation

The detector under study for the radiation damage induced by fast neutron was a $LaBr_3$:Ce detector, representing a prototype of the detector to be used for NUMEN (ϕ = 38 mm x 50 mm). The crystal is coupled with a R6231 PMT from Hamamatsu and a E1198-26 voltage divider and it was powered at HV = - 1080 V with a N147 Caen NIM module for the entire duration of the irradiation.

In order to maximize the neutron fluence in the detector, during the irradiation the latter was placed at 0°-degree respect to the beam axis at the minimum distance from the hydrogen cell exit corresponding to $d = 5\,mm$ (see Figure 5.9). In this configuration the entrance surface of the crystal fits perfectly the geometry of the neutron cone: the cone section at 5 mm is 31.4 mm while the crystal face is 38 mm therefore the entrance surface of the detector includes the totality of the neutron produced in the cone. A thin external annulus of the entrance surface of the detector is not covered by the neutron cone, however this area is negligible since it corresponds to the ~2.5% of the total surface area. A portion of the neutrons produced in the cone at $z > d$ is not covered by the detector due to its cylindrical geometry. The volume of the cone not covered by the detector corresponds to the 26% of the total volume of the cone in the detector position $0.5\,cm < z < 5.5\,cm$. However, this volume correspond to very low neutron fluxes of at least 2 order of magnitude lower than the neutron flux in the central region covered by the detector, therefore the volumetric neutron loss for $0.5\,cm < z < 5.5\,cm$ is less than 5%.

The irradiation of the detector was divided in 6 steps after which the neutron fluence was measured with the techniques showed in sec.5.2.2.

Before and after the irradiation the following were evaluated:

1. the intrinsic background;

2. the energy resolution and gain for a ^{137}Cs source (E=661.6 keV);
3. the time resolution, performing a coincidence with an auxiliary LaBr$_3$:Ce detector between the 511 keV annihilation gamma emitted by a ^{22}Na source.

The energy resolution and the gain were evaluated also at the end of each irradiation step at increasing neutron fluence. For the measurement of the characteristics at the point 2), the ^{137}Cs source was kept always at the same distance from the detector, centered respect to its axis, and the time duration of the data acquisition was the same. The recovery of the characteristics 2), for Δt after the irradiation up to 40 days, was evaluated. All the measurements were performed off-beam in a shielded environment inside the experimental hall, without turning off the detector.

For the data acquisition a Caen digitizer DT5720C was used, the signals were processed with a PSD firmware and acquired with the software Compass. The dynamic range of the digitizer DT5720C was 2 Vpp, which didn't cover the total dynamic range of the detector signals (up to 4 V). By changing the energy gain of the digitizer, it was possible to acquire the entire energy spectrum at the cost of linearity above E~900 keV, corresponding to the saturation of the dynamic range (ADC

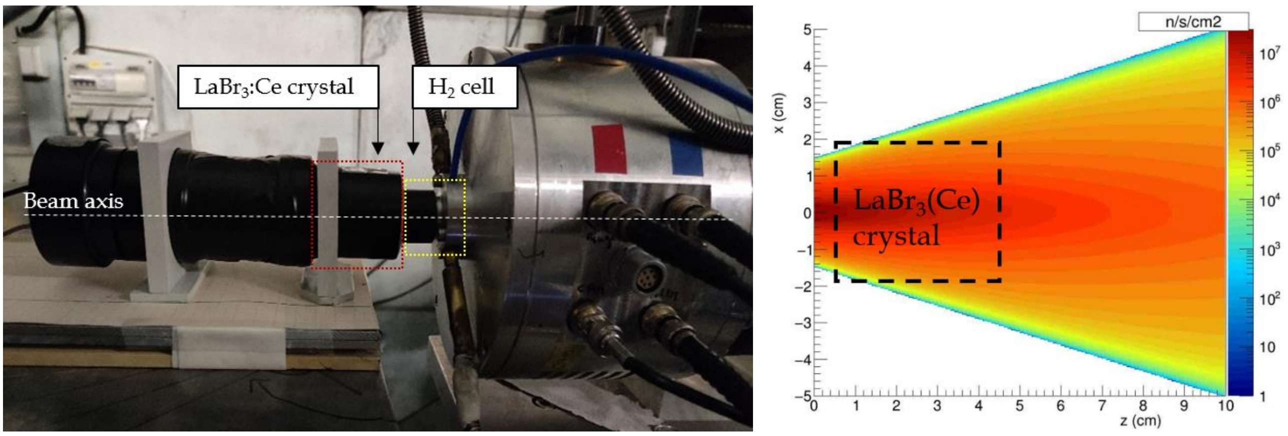

Figure 5.9 – On the left: experimental setup for the irradiation of the detector prototype with the LICORNE source. From right to left: the LICORNE source with the H$_2$ cell (yellow dotted square), the detector under study placed in front of the H$_2$ cell (red dotted square). The grey supports hold the detector, so it is aligned with the beam axis (white dotted line). In the picture it is also possible to notice the black cylindrical support placed around the hydrogen cell to hold the Indium foil used for the neutron fluence monitoring. On the right: superimposition of the actual dimensions and position of the LaBr3:Ce crystal under study with the simulation of the neutron cone geometry in the experimental condition of the work presented in this chapter.

Channel ~ 800). However, the effects of the neutron damage were evaluated at the energy of E = 661.6 keV, inside the linearity region of the acquisition system.

5.3. Results

5.3.1 Neutron fluence measurement

The neutron fluence was measured using the techniques illustrated in the section 5.2.2:

1. The evaluation of the number of ^7Be nuclei, which is equal to the number of neutrons produced in the reaction ^7Li (p,n)^7Be (see equation (5.1))
2. The evaluation of the activity of a ^{nat}In activation detector, which can be related to the total number of neutrons through the equation (5.2).

The method 1) was used at the end of each 6 irradiation steps while the method 2) was used only for the steps #3, #4,#5.

^{7}Be activity

From the activity of ^7Be is possible to extract the number of ^7Be nuclei hence the neutron fluence. The beryllium nuclei half-life is 53.12 days, much longer than the total irradiation time (3 days), therefore the nuclei number increases with the irradiation time. At the end of each irradiation step a $LaBr_3$:Ce detector (different from the one irradiated) was placed in front of the hydrogen cell, in the same position of the irradiated detector[3],

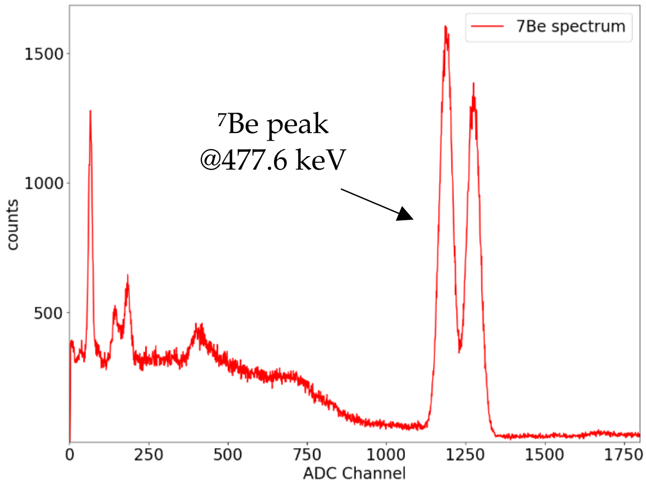

Figure 5.10 - Spectrum of the ^7Be acquired after the irradiation step#3.

[3] At the end of each irradiation step the detector under irradiation was moved from its position for the measurement of the detector characteristics. Therefore, between consequent steps it was possible to place a secondary detector at the exit of the hydrogen cell.

and the ^{7}Be counts were measured to extract the activity (eq. 5.1). In this configuration, the spectra were acquired for a fixed time $t_{meas} = 10\,min$ and the counts per second (CPS) in the energy peak corresponding to the ^{7}Be decay were evaluated. Figure 5.10 shows the spectrum acquired at the end of one irradiation step#3. The CPS in the peak have been calculated as the area of the fitted gaussian peak at 477.6 keV, subtracted by the linear background and divided by t_{meas}. Since the measurement is cumulative, the CPS relative to the nuclei implanted during a certain irradiation step correspond to the total measured CPS subtracted by the CPS measured at the end of the previous irradiation step. Figure 5.11 shows the total CPS measured at the end of each irradiation step. From the CPS relative to a certain irradiation step, it is possible to calculate the number of neutrons produced during the irradiation step using the equation 5.1. The efficiency in the above-mentioned equation includes both the geometric and the energetic contribution $\varepsilon = \varepsilon_{geom} \cdot \varepsilon_{en}$ .The geometric efficiency $\varepsilon_{geom} = 37 \pm 7\,\%$ and it is calculated as $\varepsilon_{geom} = 2\pi r(r-d)/(4\pi r^2)$ where r is the ray of the spherical surface subtended by the detector and d = *0.5 mm* is the distance source-detector. The energetic efficiency is known from literature: ε_{en} = 38% [33]. The overall efficiency is therefore calculated assuming that the ^{7}Be nuclei can be approximated as a point-like source emitting a gamma at E = 477.6 keV (the neutron beam has a narrow intense peak of ~ 8 mm – sec. 5.2.1). This approximation results in an overestimation of the actual efficiency hence an underestimation of the neutron number. Figure 5.12 shows the number of neutrons calculated for each irradiation step using equation (5.1) while Table 5.3 shows the comparison between the neutron flux measured with the ^{7}Be technique $\Phi^{exp}_{(7Be)}$ and the neutron flux expected Φ^{th} based on the beam and target

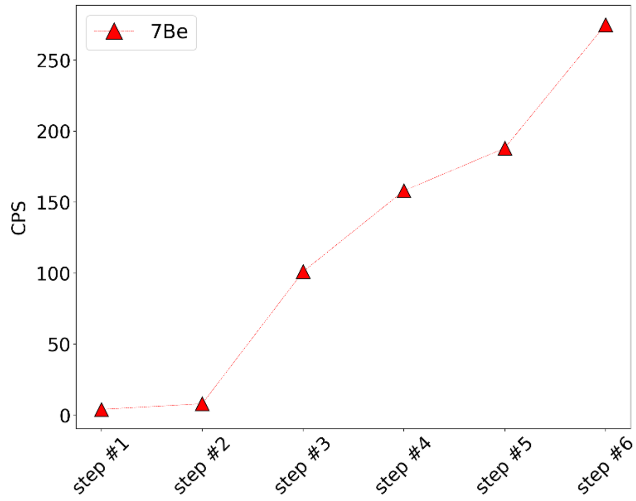

Figure 5.11 – Total CPS of the ^{7}Be nuclei at the end of each irradiation step. The errors are negligible.

parameters (sec.5.2.1). The reason of the discrepancy between the measured and theoretical values can be ascribed to a non-optimal transmission in the beam line and/or the instability of the beam focusing. The total number of neutrons for all the irradiation step, measured with the ^{7}Be techniques is $\#n_{7Be}^{TOT} = (1.23 \pm 0.3) \cdot 10^{11}\ n$ corresponding to a neutron fluence of $(1.1 \pm 0.2) \cdot 10^{10}\ n/cm^2$ in the detector.

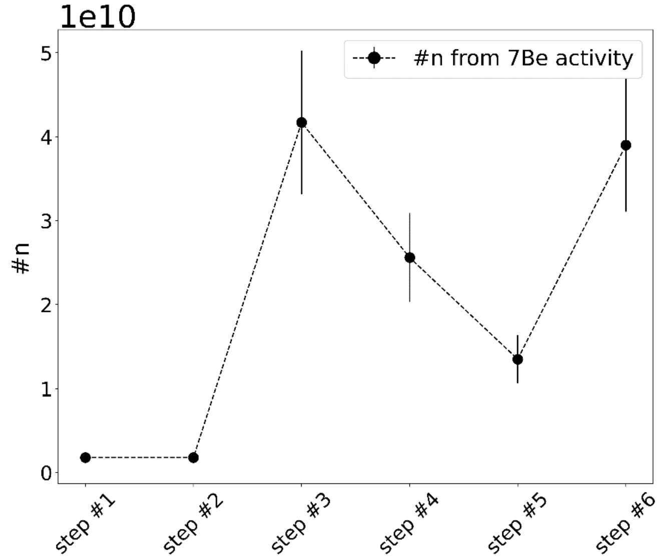

Figure 5.12 - The number of neutrons for each irradiation step, calculated with the 7Be activity monitoring technique.

#step	#neutrons	$\Phi_{(7Be)}^{exp}[n/s]$	$\Phi^{th}\ [n/s]$
1	$(1.8 \pm 0.4) \cdot 10^{9}$	$6 \cdot 10^{6}$	$1 \cdot 10^{7}$
2	$(1.8 \pm 0.4) \cdot 10^{9}$	$1 \cdot 10^{6}$	$1 \cdot 10^{7}$
3	$(4.2 \pm 0.8) \cdot 10^{10}$	$1.4 \cdot 10^{6}$	$9.9 \cdot 10^{6}$
4	$(2.6 \pm 0.5) \cdot 10^{10}$	$3.55 \cdot 10^{6}$	$1.6 \cdot 10^{7}$
5	$(1.3 \pm 0.3) \cdot 10^{10}$	$4.1 \cdot 10^{6}$	$1.4 \cdot 10^{7}$
6	$(3.9 \pm 0.8) \cdot 10^{10}$	$1.1 \cdot 10^{7}$	$1.4 \cdot 10^{7}$

Table 5.3 – Comparison between measured and theoretical neutron flux for each irradiation step.

^{nat}In activation foil

The Indium foils were used to measure the neutron fluence during the irradiation steps #3,#4,#5. The foils were replaced at the end of each irradiation step. For each foil the activity of the peak at E = 336 keV was calculated using the equation (5.3) where the geometric efficiency was given by simulations performed by the radioprotection department of the IJC Laboratory, taking into account the dimensions of the In samples. Figure 5.13 shows one of the In foils spectra acquired with the HPGe detector. The red line marks the peak at 336 keV, representative of the reaction under study for the evaluation of the neutron fluence (see sec.5.2.2). The counts in the peak were evaluated as the area of the 336 keV peak subtracted by the background (linear).

The spectra of the In foils were acquired after a time t* from the stop of the irradiation, and then at increasing Δt from the irradiation to reconstruct the decay curve of the 336 keV peak. Figure 5.14 represent the activity of the Indium foil used for the irradiation step #3 at increasing time from the irradiation stop. The red dotted line is the exponential fit from which A_0 and τ where evaluated :

$$A(t) = A_0(t \quad = 0)e^{-t/\tau} \tag{5.4}$$

where τ corresponds to the decay time of the ^{115m}In isotope, and A_0 corresponds to the activity of the foil at the irradiation stop. The calculated decay time τ^{exp}= 6.45 h differs from the theoretical $\tau^{theo} = 6.48\,h$ from less than 0.5%. The number of neutrons produced during the irradiation step was calculated through the equation

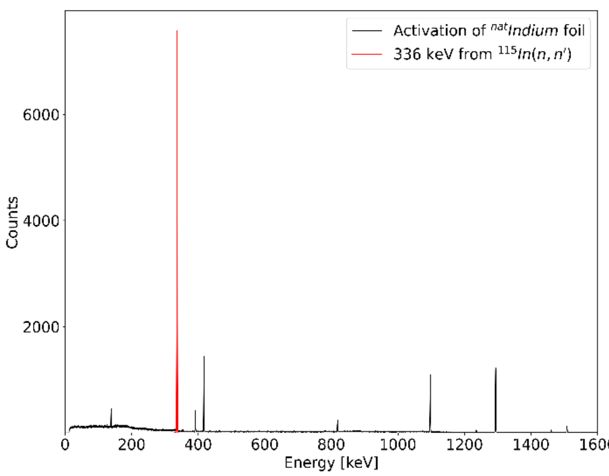

Figure 5.13 - HPGe detector spectrum of one Indium foil used for the monitoring of the neutron fluence in the step#3. The red line corresponds to the 336 keV peak of interest for the neutron monitoring. The spectrum shown in figure has been acquired after 10 minutes from the irradiation.

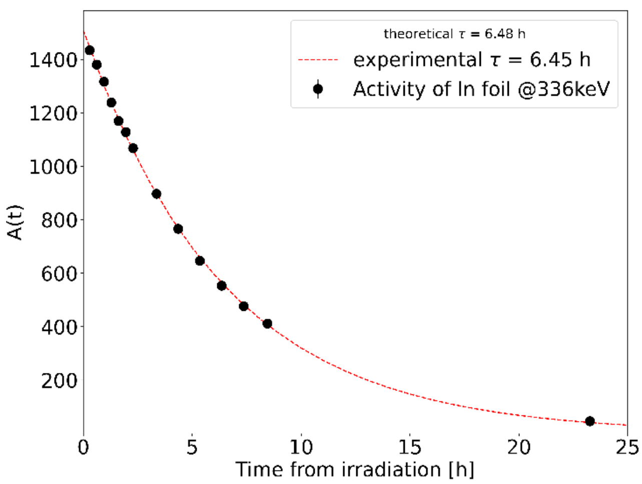

Figure 5.14 - Decay curve of the 336 keV peak of the Indium foil. The exponential fit is represented by the red dotted line. The data refers to the Indium foil used for the step#3.

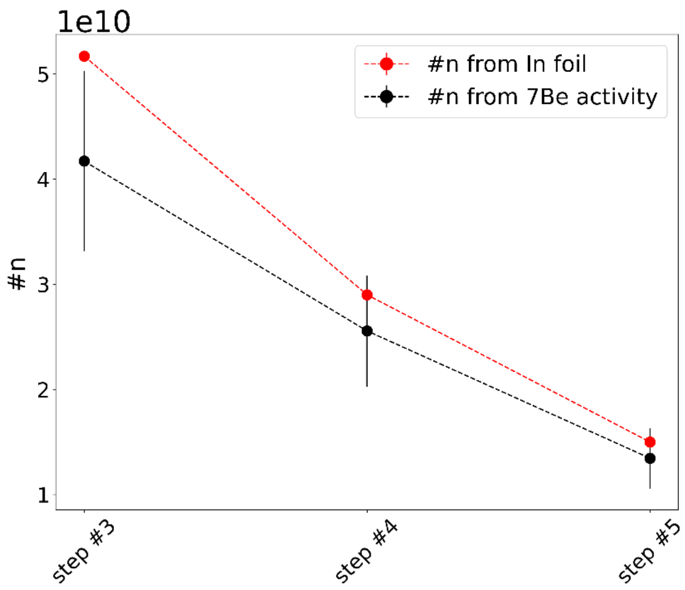

Figure 5.15 – Comparison of #n calculated with the two monitoring techniques used in this work.

(5.1). Table 5.4 lists the activity of the three foils, the results for the respective number of neutrons and the comparison with the results of the ^{7}Be technique as well as the expected neutron production. It can be noticed that the results of the two monitoring techniques are consistent within the error bars (expect step#3). The neutron production calculated through the ^{7}Be technique is always lower than the value obtained with the activation foil technique: as stated before, this difference is due to the use of the point-like source approximation for the evaluation of the efficiency in eq. (5.1) for the calculation of #n(^{7}Be), which leads to an overestimation of ε, i.e. an underestimation of the neutron production. Figure 5.15 shows the comparison of the neutron number calculated using the two techniques. The neutron production results from both techniques is lower than the one expected from the LICORNE theoretical calculation, confirming the assumption made in the previous section on the non-optimal beam transmission and/or the instability of the beam focusing.

For a conservative estimation of the radiation damage on the detector, #n(^{7}Be) was considered as reference value for the calculated neutron production during the irradiation. Therefore, the characterization of the neutron damage effects on the detector (section 5.3.2) refers to the #n listed in Table 5.4, the total number of neutron in the detector is $(1.23 \pm 0.3) \cdot 10^{11}$ and the neutron fluence is $(1.1 \pm 0.2) \cdot 10^{10}$ n/cm^{2}.

step	A [Bq]	#n(In)	#n(^7Be)	$\Phi^{exp}_{foil}[n/s]$	$\Phi^{exp}_{7Be}[n/s]$	Φ^{th} $[n/s]$
3	2127.7 ± 10	$5.2 \cdot 10^{10}$	$(4.2 \pm 0.8) \cdot 10^{10}$	$1.7 \cdot 10^6$	$(1.4 \pm 0.2) \cdot 10^6$	$9.9 \cdot 10^6$
4	1023.1 ± 5	$2.9 \cdot 10^{10}$	$(2.6 \pm 0.5) \cdot 10^{10}$	$4 \cdot 10^6$	$(3.5 \pm 0.7) \cdot 10^6$	$1.6 \cdot 10^7$
5	548.3 ± 3	$1.5 \cdot 10^{10}$	$(1.3 \pm 0.3) \cdot 10^{10}$	$4.6 \cdot 10^6$	$(4.1 \pm 0.8) \cdot 10^6$	$1.4 \cdot 10^7$

Table 5.4 – Results of the activation foil monitoring technique and comparison with the results of the ^{7}Be technique illustrated in the previous section and the theoretical values. The error for the #n(In) are negligible.

^{7}Li CoulEx

The measurement of the ^{7}Li Coulomb excitation peak allowed to monitor the variations of the Li-beam during the irradiation of the detector, hence the higher the neutron flux, the higher the CPS in the detector. Figure 5.16 shows a typical spectrum acquired with the monitoring detector. During the irradiation the CPS in the CoulEx peak were monitored in order to adjust the beam parameters and/or the irradiation time accordingly and to obtain the maximum neutron fluence possible in the detector.

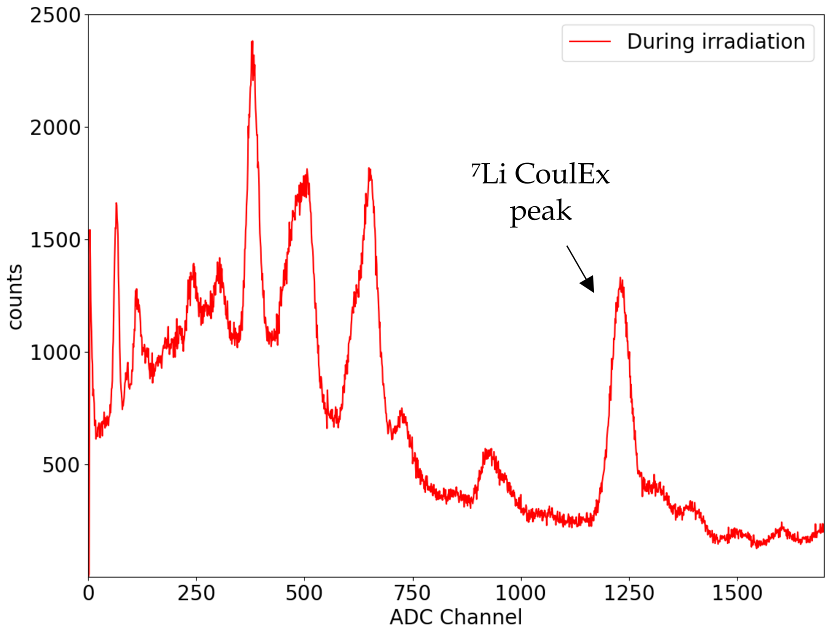

Figure 5.16 - Spectrum of the ^{7}Li CoulEx peak acquired with a detector placed at 40° degrees respect to the beam axis, during the irradiation of the detector under study.

5.3.2 Evaluation of the radiation damage and its recovery

The detector was irradiated with a maximum neutron fluence of $(1.1 \pm 0.2) \cdot 10^{10}\ n/cm^2$.The damage of the detector was quantified in terms of changes in the intrinsic background, variations in the gain and energy resolution at 661.6 keV and variation in time resolution.

Intrinsic background

The intrinsic background of the detector was measured before the neutron irradiation and after 24 hours from the irradiation stop. The background was acquired inside the experimental hall, while the detector was shielded with Pb layer. The duration of the data acquisition was the same for both measurements in order to obtain the same statistics ($t_{meas} = 20\ min$). Figure 5.17 shows the intrinsic background before and after 24 h from the irradiation. It can be noticed that the shape of the energy spectrum is the same, however the detection rate increased uniformly of 112%, from 250 kHz to 530 kHz. As a result, the spectrum after the irradiation (red line) is shifted up respect to the spectrum before the irradiation (black line). The increase of the intrinsic background rate has been observed in literature: Lu et al.

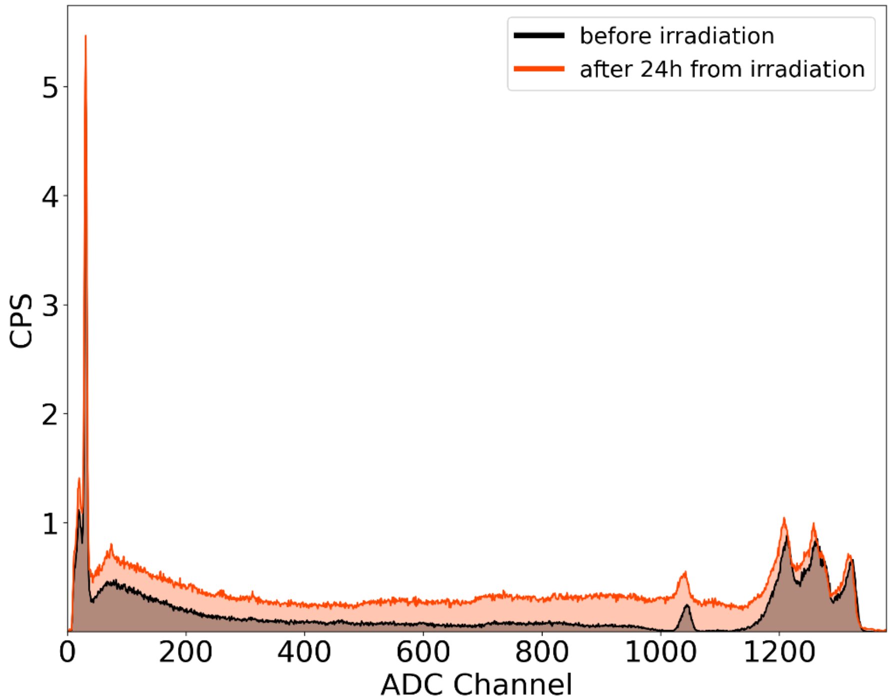

Figure 5.17 - Intrinsic background of the detector before and after 24 hours form the neutron irradiation.

have reported a rate increase of ~120% after exposing the detector to $2 \cdot 10^8 \ n/cm^2$, two orders of magnitude lower than the experiment presented in this work. However the background increase reported in Ref. [45] was consistent especially in the low energy region, while in the work presented in this chapter the increase is uniform. This difference can be ascribed to the different neutron energies used for the irradiation (thermal neutron energies from a reactor for Lu et al. and fast neutrons in this work). The reasons for this effect are not clear, and they can be related, for example, to a non-optimal shielding of the detector during the background acquisition or to an increased electronical noise in the experimental hall. More studies are needed in order to be able to disentangle the effect on the detector from the eventual environmental noise. The detection rate of the intrinsic background was found to be restored after 1 week from the end of the irradiation (measured in another laboratory).

From Figure 5.17 it is possible to notice a shift in the ADC channel which is not linear with the energy. The evaluation of this effect can be done using the characteristic intrinsic peaks at E = 35.5 keV and E = 1472 keV (see Chapter 3) .

Table 5.5 shows the comparison of the gain and the resolution for the above-mentioned background peak before and after the neutron irradiation. While there is no substantial variation of the characteristics at E = 35.5 keV, the position of the peak at 1427 keV shows a slight change. However, the position of the latter intrinsic peak is above the linearity region (see sec.5.2.3) therefore its behaviors is not well representative of the detector damage since it can be affected by the digitizer's non-complete charge collection of the detector signal.

	35.5 keV		**1472 keV**	
	x	**Resolution [%]**	**x**	**Resolution [%]**
before	31.6 ± 1.8	14	1044 ± 7	1.65
after (24h)	31.3 ± 1.8	14	1038 ± 7	1.74

Table 5.5 – Comparison of gain and resolution for the intrinsic background peak before and after the neutron irradiation.

Gain and energy resolution

The energy resolution and the gain have been evaluated at the energy corresponding to the ^{137}Cs peak of E = 661.6 keV at increasing neutron fluence. All the spectra of the above-mentioned source have been acquired keeping fixed the distance source-detector ($d = 5\ cm$) as well as the acquisition time ($t_{meas} = 10\ min$). For each spectrum it was evaluated: the variation of the position of the 661.6 keV peak (% gain variation) with respect to the spectrum acquired before the neutron irradiation; the resolution at the same energy. It was evaluated also the recovery of these characteristics after different time periods from the irradiation stop, up to 40 days. Figure 5.18 shows the ^{137}Cs spectra before the irradiation, after 24 hours and after 40

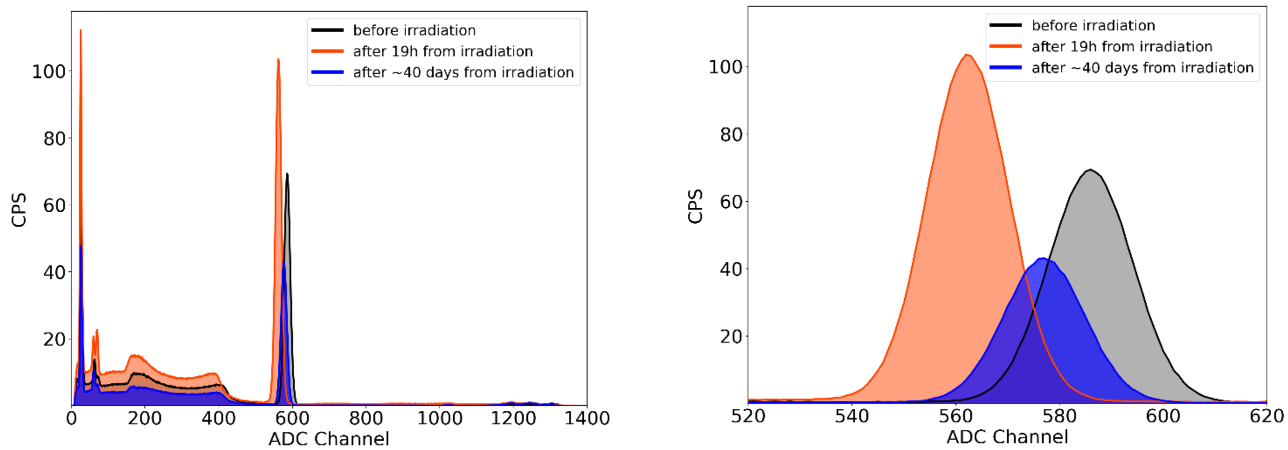

Figure 5.18 – Left: ^{137}Cs spectra of the detector under study before the neutron irradiation (black), after 24 hours from the irradiation stop (red) and after 1 month (blue). Right: zoom of the spectra around the region of the ^{137}Cs peak.

days from the irradiation. It can be noticed that the gain at 661.6 keV decreased after the irradiation (red line) with respect to the position before the irradiation (black line). However, after a 40 days-period, the gain recovers (blue line). Figure 5.19 – left shows the variation of the gain with respect to the position of the ^{137}Cs peak before the irradiation, after increasing neutron fluence. The black dotted lines represent the maximum and minimum value of the initial gain (considering the errors) and the grey area represents its total interval. After the total neutron fluence of $(1.1 \pm 0.2) \cdot 10^{10}\ n/cm^2$, the gain at 661.6 keV decreases of 4.0 ± 1.4 % with respect to the initial gain (before the irradiation). This gain decrease is expected from the literature at

661.6 keV after $\sim 10^8 n/cm^2$ is 4 – 8 %. However, the ^{137}Cs spectrum acquired for the evaluation of the damage after the irradiation with total neutron fluence was taken after 24 hours from the end of the irradiation for technical reasons, therefore it could be possible that the measured gain variation can include a partial recover of the detector and that the effective damage after $(1.1 \pm 0.2) \cdot 10^{10}\ n/cm^2$ could be higher than 4.0 ± 1.4 %.

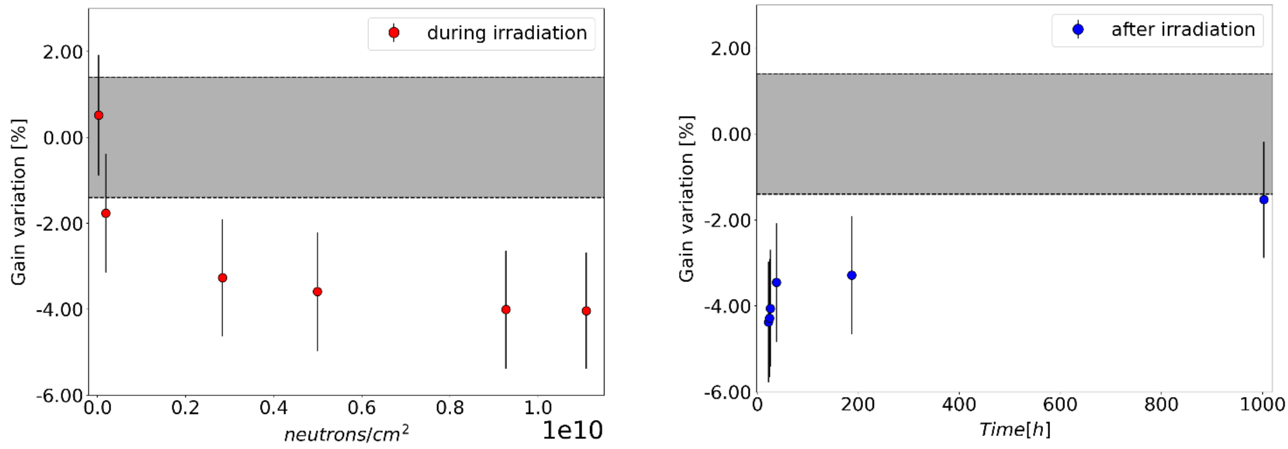

Figure 5.19 – Variation of the gain of the 661.6 keV peak with respect to the spectrum before the neutron irradiation at increasing neutron fluence (left) and at increasing time after irradiation (right). The grey band corresponds to the interval value of the initial point (considering the errors).

Figure 5.19 – right shows the recovery of the gain variation after increasing time periods from the irradiation stop. After 1003 hours (~40 days) from the irradiation, a total recovery of the gain was observed. The data point at t = 200 h and t = 1003 h were acquired in a different laboratory with respect to the other data points, with a different power supply module (same HV) but with the same acquisition system (digitizer + firmware + software).

The resolution of the ^{137}Cs peak as a function of the neutron fluence is shown in Figure 5.20 – left. The neutron fluence causes a decline in the energy resolution which goes from 3.26% to 3.34% after $\sim 5 \cdot 10^9\ n/cm^2$. This decline is lower than expected from literature for lower fluences of both thermal and fast neutrons [47].

However, from Figure 5.20 it can be noticed that the damage at the total neutron fluence is lower than the damage at lower fluence. This is due to the fact that the damage for the point at the total neutron fluence has already partially recovered thanks to the annealing effect, since the spectrum related to this data point was acquired after 24 hours from the irradiation stop. In fact, it is expected a total recovery of the resolution at a certain time after the irradiation. According to these results, the recovery time for the resolution after a neutron damage induced by fast neutrons with a fluence of $(1.1 \pm 0.2) \cdot 10^{10}\ n/cm^2$ is $t_{recovery} \leq$ 24 hours.

Figure – right shows the resolution after different time period from the irradiation stop. The resolution values after the irradiation are all consistent with resolution value before the neutron irradiation. As discussed above, the two data points relative to t = 200 h and t = 1003 h have been acquired in a different laboratory and have, therefore, greater error bars with respect to the other data points.

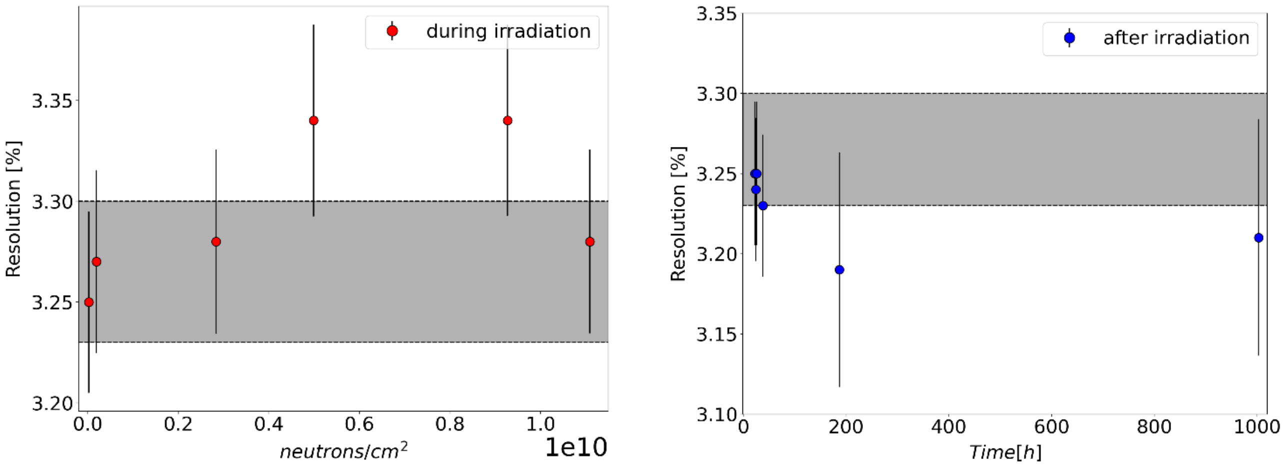

Figure 5.20 - Energy resolution of 661.6 keV peak at increasing neutron fluence (left) and its recovery at increasing time period from the irradiation stop (right). The black dotted line and the grey area represent the interval of the resolution value before the irradiation.

Time resolution

The time resolution of the detector was evaluated before and after the neutron irradiation. The two 511 keV annihilation gamma emitted in coincidence by a ^{22}Na source were measured using an auxiliary $LaBr_3:Ce$ detector (not irradiated). The acquisition system for both detectors is the one previously. The detectors were aligned and placed at 180° respect to each other at a distance of 20 cm, and the ^{22}Na source was positioned at the center. The coincidence was processed offline considering a time window of 40 ns (the data were analyzed with a ROOT macro). After applying an energy selection of the events in the 511 keV peak for both detectors the time spectrum was analyzed, and the sigma σ of the gaussian fit was evaluated. Figure 5.21 shows the time spectra before (left) and after (right) the neutron irradiation. The sigma of the gaussian peak before and after are respectively $\sigma_{before} = 3.3\, ns$ and $\sigma_{after} = 2.9\, ns$. There is no substantial change in the time resolution after the exposure of the detector to $(1.1 \pm 0.2) \cdot 10^{10}\, n/cm^2$.

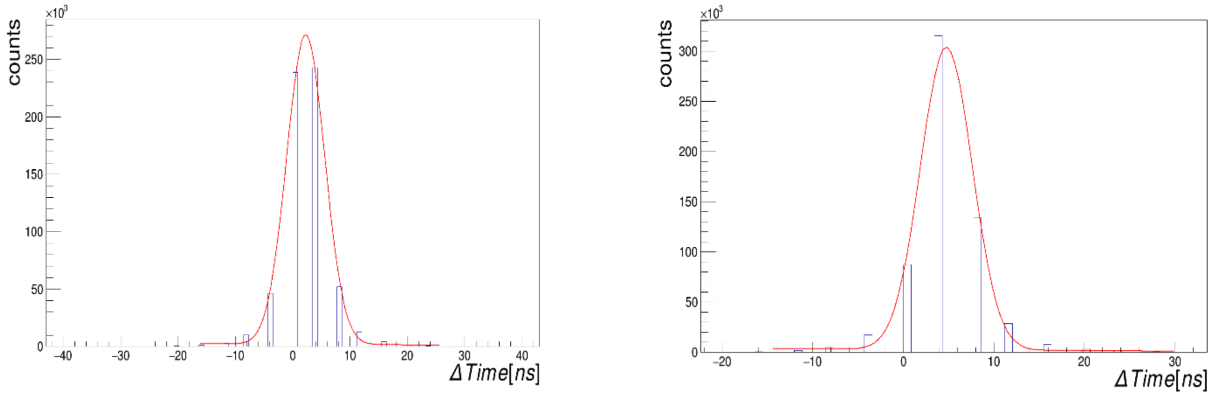

Figure 5.21 - Time spectra of the coincidence between the two detectors in the 511 keV region before (left) and after (right) the irradiation.

5.4. Discussion

In this work it has been studied the neutron damage induced in a $LaBr_3$:Ce (ϕ = 38 mm x 50 mm) after the exposure to a fast neutron fluence of $(1.1 \pm 0.2) \cdot 10^{10}\, n/cm^2$. The neutron fluence was measured with two different techniques, obtaining consistent results. The damage of the detector was evaluated in terms of the intrinsic background detection rate, energy resolution, gain and time resolution. The energy resolution and the gain were evaluated also at intermediate neutron fluences.

The detector showed an increase of the intrinsic detection rate of 112% after the neutron irradiation, but after 1 week from the irradiation stop the detection rate was restored. The gain at 662 keV suffers from a decline of 4 ± 1.4 % after the irradiation but it shows an increasing recovery over time. The period after which there is a total recovery is ~ 41 days. For what concerns NUMEN, the decrease in gain is not crucial for the experiment outcome but it suggests that it might be necessary to periodically calibrate the detectors during the data acquisition.

The resolution damage caused by the neutron fluence is the most important result to evaluate for the NUMEN experiment, since the decline in resolution could prevent it from distinguishing the first excited state transition of the DCE reaction from the background. This work shows that the resolution damage is negligible and that there is a total recovery of the performance already after 24 hours from the irradiation stop. It must be noticed that the effect of the neutron damage after the total neutron fluence could be underestimated because they have been evaluated after 24 hours from the irradiation stop, therefore they include the annealing effect of the crystal.
The work presented in this chapter explores for the first time the effect of the fast neutron damage on the $LaBr_3$:Ce at fluences of the order of magnitude of $10^{10}\ n/cm^2$. The results showed in this work are promising as they suggest that the detector performances are not permanently damaged after the neutron irradiation. The detector characteristics after the neutron exposure of $10^{10}\ n/cm^2$ still satisfy the NUMEN needs mainly in terms of energy resolution.
The total neutron fluences investigated are lower than those expected for the NUMEN experiment ($\Phi_n^{max} = 10^{11} - 10^{12}\ n/cm^2$) and they correspond to a data acquisition period of about 2 days with the respect to the foreseen 30 days. For this reason, further studies are needed at higher neutron fluence to evaluate and prevent a possible permanent damage of the detectors. It is crucial to evaluate the recovery time of the detector because if the damage after a given neutron fluence will be too high, it could be possible to consider to split the data acquisition in subsequent steps to allow the detectors to fully recover their performance.
In order to investigate the detector damage at higher neutron fluences, a new experiment to be performed at the ALTO facility (IJC Laboratory) is already planned. The experiment will consist in the same type of measurements illustrated in this chapter, but the foreseen total neutron fluence will be higher, in order to match the NUMEN needs. Some improvements are planned based on the results of this work.
For the monitoring of the <u>neutron fluences</u>:

- The accuracy of the ^{7}Be monitoring technique will be improved. The activity of the ^{7}Be nuclei in the hydrogen cell will be measured during the irradiation with the same method illustrated in this chapter but, in addition, it will be measured also at the end of the irradiation both with the methods already used and with a HPGe detector. The measurement with the HPGe detector will provide a more accurate estimation of the total neutron fluence and it will be used as reference for the other measurements at intermediate neutron fluence;
- If possible, an Indium foil will be used during each irradiation step;
- The results from the monitoring techniques illustrated in this work will be compared with the intensity of the beam measured with a Faraday Cup (FC) along the beam line. The FC will be placed just before the LICORNE source in order to guarantee optimally check the focusing the beam. This improvement will provide a calibration of the beam intensity in neutron flux.

For the monitoring of radiation damage:

- For the acquisition system it is planned to use a VX2745 Caen digitizer with a dynamic range of 4 Vpp. This will allow to avoid any non-linearity effects related to a partial charge collection;
- The intrinsic background of the detector will be acquired before and after the irradiation (as in this work) but also at increasing neutron fluence. Moreover, the same measurements (at the same time) will be acquired also with a reference detector not irradiated, in the same experimental condition. In this way it would be possible to distinguish between the effects of the neutron damage and the environmental noise;
- The results suggest that the effect of the neutron damage on the gain and on the resolution could be different at different energies. For this reason, it is foreseen to investigate the energy resolution and gain at other energies, in

addition to the 662 keV peak of the ^{137}Cs, by using for example ^{152}Eu, ^{207}Bi and/or ^{60}Co sources.

Conclusions

The development of the detection apparatus of the NUMEN project presents numerous challenges related to the detection of DCE events with low cross section. The entire detection apparatus, as well as the LNS facility, is currently under a significant upgrade essential in order to match the requirements needed by the NUMEN project. In addition to the upgrade of the existing facility, it is foreseen the development of a new gamma array, G-NUMEN, for the identification of the DCE events in all the reactions involving extreme experimental conditions (high energy beams and deformed nuclei).

This thesis work focused on the study and characterization of the future G-NUMEN array and it presents the first experimental results of a prototype of the detector's array. The full characterization of the detector presented in Chapter 3 showed promising results for the fulfillment of the NUMEN requirements.

For a complete study of the detector performances an in-beam experiment (HIT) was designed and performed at the ALTO facility for the investigation of the main issues related to the gamma array: the response of the detector to extreme detection rates and its radiation hardness for intense fast neutron fluences.

In Chapter 3 and 4 it was shown that the response of the detector is strictly dependent on the detection rate, both in terms of energy and time resolutions whose values can significantly worsen when reaching the rates expected in NUMEN. This work shows that, in order to overcome the problems appearing in these extreme conditions, it would be possible to enhance the detector performances by improving its electronic in order to satisfy the NUMEN needs.

Another important aspect of the gamma array regards the intense neutron fluences it will be exposed to and the consequent detector damage about which there are no data in literature. Chapter 5 presented the study of the detector radiation damage and its recovery time after the exposure to fast neutrons at fluences never

investigated before. The performance of the detector decreases in terms of energy resolution and gain, but a complete recovery is possible for both characteristics after waiting a proper amount of time. These results are encouraging for the NUMEN experiment, as they suggest that even if it would be necessary to set a limit for the data acquisition periods, it could be possible to preserve the G-NUMEN performance simply by waiting a short amount of time needed for the detector recovery.
In conclusion, the results of this work set the stage for the future developments of the G-NUMEN array which will involve: the test of new electronic for the detectors and the study of the discrimination capabilities of a scaled array of the detector; the study of the radiation damage at higher neutron fluences. For this purpose, a new experiment to be performed at the ALTO facility is foreseen.

References

[1] NUMEN project, «INFN,» [Online]. Available:

https://web.infn.it/NUMEN/index.php/it/.

[2] Agodi et al., «NUMEN Project @ LNS : Heavy ions double charge exchange reactions towards the 0vββ nuclear matrix element determination,» *AIP Conference Proceedings,* vol. 1686, 2015.

[3] Cappuzzello et al., «The NUMEN Project: An Update of the Facility Toward the Future Experimental Campaigns,» *Frontiers in Astronomy and Space Sciences,* vol. 8, 2021.

[4] Engel et al., «Status and future of nuclear matrix elements for neutrinoless double-beta decay: a review,» *Reports on Progress in Physics,* vol. 80, 2017.

[5] Wang et al., «Comparison between variational Monte Carlo and shell model calculations of,» *Physics Letter B,* vol. 798, 2019.

[6] Cappuzzello et al., «The NUMEN technical design report,» *International Journal of Modern Physics,* vol. 36, 2021.

[7] Cappuzzello et al., «The role of nuclear reactions in the problem of 0vββ decay and the NUMEN project at INFN-LNS,» *Journal of PHysics Conference Series,* vol. 630, 2015.

[8] Cappuzzello et al., «Shedding light on nuclear aspects of neutrinoless double beta decay by heavy-ion double charge exchange reactions,» *Progress in Particle and Nuclear Physics,* vol. 128, 2023.

[9] Bellone et al., «Probing beta decay matrix elements through heavy ion charge exchange reactions,» *Journal of Physics Conference Series,* vol. 1056, 2018.

[10] Lenske, «Probing Double Beta-Decay by Heavy Ion Charge Exchange Reactions,» *Journal of Physics: Conference series,* vol. 1056, 2018.

[11] Lenske, «Theory of Heavy Ion Single and Double Charge Exchange Reactions,» *Theory of Heavy Ion Single and Double Charge Exchange Reactions,* vol. 1, 2019.

[12] Carbone et al., «The nuclear matrix elements of 0νββ decay and the NUMEN project at INFN-LNS,» *EPJ Web Conf.,* vol. 194, 2018.

[13] Cappuzzello et al., «Heavy-ion double charge exchange reactions: a tool towards 0νββ nuclear matrix,» *European Physical Journal A,* vol. 51, 2015.

[14] Cappuzzello et al., «The MAGNEX spectrometer: Results and perspectives,» *The European Physical Journal A,* vol. 52, 2016.

[15] Calabretta et al., «UPGRADE OF THE LNS SUPERCONDUCTING CYCLOTRON FOR BEAM POWER HIGHER THAN 2-5 kW,» *Proceedings of Cyclotrons,* 2016.

[16] Calanna et al., «UPGRADE OF THE LNS SUPERCONDUCTING CYCLOTRON,» *Proceedings of IPAC2015,* 2015.

[17] Santoncito et al., «Upgrade of the experimental Facilities at LNS,» *IL NUOVO CIMENTO,* vol. 41, 2018.

[18] Finocchiaro et al., «The NUMEN Heavy Ion Multidetector for a Complementary Approach to the Neutrinoless Double Beta Decay,» *universe,* vol. 6, 2020.

[19] Oliveira et al., «New spectrometer projects for challenging particle-gamma measurements of nuclear reactions,» *Journal of Physics: Conference Series,* vol. 1056, 2018.

[20] Oliveira et al., «First comparison of GEANT4 hadrontherapy physics model with experimental data for a NUMEN project reaction case,» *Eur. Phys.J.A.,* vol. 56, 2020.

[21] M. Rudigier et al., «FATIMA — FAst TIMing Array for DESPEC at FAIR,» *NIM-A,* vol. 969, 2020.

[22] M. Rudigier et al., «Isomer spectroscopy and sub-nanosecond half-live determination in 178w using the NuBall array,» *Acta Physica Polonica B,* vol. 50, 2019.

[23] K. Shah et al., «LaBr 3:Ce scintillators for gamma ray spectroscopy,» *2002 IEEE Nuclear Science Symposium Conference Record,* 2002.

[24] E. Loef et al., «Scintillation properties of LaBr3:Ce3+ crystals: fast, efficient and high-energy-resolution scintillators,» *NIM-A,* vol. 486, 2002.

[25] G. Gosta et al., «Response function and linearity for high energy g-rays in large volume LaBr:Ce detectors,» *NIM-A,* vol. 879, 2018.

[26] R. Nicolini et al., «Investigation of the properties of a 100 100 LaBr3:Ce scintillator,» *NIM-A,* vol. 582, 2007.

[27] A. Lavagno et al., «Study of linearity and internal background for LaBr3(Ce) gamma-ray scintillation detector,» *NIM-A,* vol. 718, 2013.

[28] F. Quarati et al., «Study of 138La radioactive decays using LaBr3 scintillators,» *NIM-A,* vol. 683, 2012.

[29] L. Swiderski et al., «Scintillators for high temperature plasma diagnostics,» *Proceedings of Science ECPD,* 2015.

[30] P. Sibczynski et al., «Characterization of some modern scintillators recommended for use on large fusion facilities in gamma-ray spectroscopy and tomographic measurements of X-emission,» *NUKLEONIKA,* vol. 3, 2017.

[31] Dorenbos et al., «"Nonproportional response of LaBr3:Ce and LaCl3:Ce scintillators to synchrotron x-rayy irradiation,» *JOURNAL OF PHYSICS: CONDENSED MATTER,* vol. 22, 2010.

[32] R. Casanovas et al., «Energy and resolution calibration of NaI(Tl) and LaBr3(Ce) scintillators and validation of an EGS5 Monte Carlo user code for efficiency calculations,» *NIM-A,* vol. 675, 2012.

[33] Aldawood et al., «Comparative Characterization Study of a LaBr3Ce Scintillation Crystal in Two Surface Wrapping Scenarios: Absorptive and Reflective,» *Front. Oncol.,* vol. 5, 2015.

[34] A. Caricato et al., «Thermal neutron conversion by high purity 10B-enriched layers: PLD-growth, thickness-dependence and neutron-detection performances,» *The European Physical Journal Plus,* vol. 137, 2022.

[35] Photonis, «Photomultiplier tube basics».

[36] Yu et al., «Study of the performance of photomultiplier tubes at high variable counting rates,» *NIM-A,* vol. 1008, 2021.

[37] P. Dorenbos et al., «Gamma Ray Spectroscopy With a 19 19 mm3 LaBr3 : 0:5% Ce3+ Scintillator,» *IEEE Tran. on Nucl. Sc.,* vol. 51, 2004.

[38] R. Pani et al., «Pulse height non-linearity in LaBr3:Ce crystal for gamma ray spectrometry and imaging,» *Nuclear Physics B - Proceedings Supplements,* vol. 215, 2011.

[39] S. Franchoo et al., «The ALTO project at IPN-Orsay,» *Hyperfine Interact,* vol. 171, 2006.

[40] S. Franchoo et al., «The Alto Tandem and Isol Facility at IPN Orsay,» *JPS Conf. Proc.,* 2015.

[41] R. Bass, «Nucleus-Nucleus Potential Deduced from Experimental Fusion Cross Sections,» *Phys.Rev. Lett.,* vol. 39, 1977.

[42] M. Fragopoulou et al., «Shielding around spallation neutron sources,» *Journal of Physics: Conference Series,* vol. 41, 2006.

[43] Normand et al., «Resistance to g irradiation of LaBr3:Ce and LaCl3:Ce single crystals,» *NIM-A,* vol. 572, 2007.

[44] F. Quarati et al., «X-ray and gamma-ray response of a 2"x2" LaBr3:Ce scintillation detector,» *NIM-A,* vol. 574, 2007.

[45] Yu et al., «Study of neutron radiation effect in LaBr3 scintillator,» *Chinese Physics C,* vol. 39, 2015.

[46] C. Cazzaniga et al., «Response of LaBr3(Ce) scintillators to 14 MeV fusion neutrons,» *NIM-A,* vol. 778, 2015.

[47] C. Cazzaniga et al., «Response of LaBr3(Ce) scintillators to 2.5 MeV fusion neutrons,» *Review of Scientific Instruments,* vol. 84, 2013.

[48] M. Lebois et al., «Development of a kinematically focused neutron source with the p(7Li,n)7Be inverse reaction,» *NIM-A,* vol. 735, 2014.

[49] J. Wilson et al., «LICORNE: A new and unique facility for producing intense, kinematically focused neutron beams at the IPN Orsay,» *EPJ Web of Conferences,* vol. 62, 2013.

[50] L. Qi et al., «Prompt fission gamma-ray emission spectral data for 239Pu(n,f) using fast directional neutrons from the LICORNE neutron source,» *EPJ Web of Conferences,* vol. 169, 2018.

[51] P. Agnes et al., «Measurement of the liquid argon energy response to nuclear and electronic recoils,» *PHYSICAL REVIEW-D,* vol. 97, 2018.

[52] M. Lebois et al., «Studies for X-ray emission in the fission process with LICORNE,» *EPJ Web of Conferences,* vol. 122, 2016.

[53] D. Rutte et al., «Boutique neutrons advance 40Ar/39Ar geochronology,» *Science Advances,* vol. 5, 2019.

[54] G. Martin-Hernandez et al., «Excitation function shape and neutron spectrum of the 7Li(p,n)7Be reaction near threshold,» *PHYSICAL REVIEW C,* vol. 96, 2016.

[55] «The Lund/LBNL Nuclear Data Search,» [Online]. Available: http://nucleardata.nuclear.lu.se/toi/nuclide.asp?iZA=40007.

[56] J. Chao et al., «Activation detection using indium foils for simultaneous monitoring neutron and photon intensities in a reactor core,» *Radiation Measurements,* vol. 45, 2010.

[57] Vermeer et al., «Coulomb excitation of 7Li,» *Australian Journal of Physics,* vol. 37, 1984.

[58] M. Fatemian et al., «Coulomb excitation of 7Li in the cluster model,» *Journal of Physics G: Nuclear Physics,* vol. 12, n. 11, 1986.

[59] CAEN, «User Manual UM5960 - Multiparametric DAP Software for PHysics,» 2022.

[60] Saint-Gobain, «Scintillation products - Technical Note: Lanthanum Bromide Scintillators,» 2019.

[61] EPIC. [Online]. Available: https://www.epic-crystal.com/halide-scintillators/labr3-ce-scintillator.html.